Titre: Title:	Retroreflector and Multibeam Antenna for a Millimeter Wave Collision Avoidance System
Auteur: Author:	Ahmed Bilal Numan
Date:	2018
Type:	Mémoire ou thèse / Dissertation or Thesis
Référence: Citation:	Numan, A. B. (2018). Retroreflector and Multibeam Antenna for a Millimeter Wave Collision Avoidance System [Thèse de doctorat, École Polytechnique de Montréal]. PolyPublie. https://publications.polymtl.ca/3035/

URL de PolyPublie: PolyPublie URL:	https://publications.polymtl.ca/3035/
Directeurs de recherche: Advisors:	Jean-Jacques Laurin, & Jean-François Frigon
Programme: Program:	génie électrique

UNIVERSITÉ DE MONTRÉAL

RETROREFLECTOR AND MULTIBEAM ANTENNA FOR A MILLIMETER WAVE COLLISION AVOIDANCE SYSTEM

AHMED BILAL NUMAN
DÉPARTEMENT DE GÉNIE ÉLECTRIQUE
ÉCOLE POLYTECHNIQUE DE MONTRÉAL

THÈSE PRÉSENTÉE EN VUE DE L'OBTENTION
DU DIPLÔME DE PHILOSOPHIÆ DOCTOR
(GÉNIE ÉLECTRIQUE)
AVRIL 2018

UNIVERSITÉ DE MONTRÉAL

ÉCOLE POLYTECHNIQUE DE MONTRÉAL

Cette thèse intitulée :

RETROREFLECTOR AND MULTIBEAM ANTENNA FOR A MILLIMETER WAVE COLLISION AVOIDANCE SYSTEM

présentée par : NUMAN Ahmed Bilal
en vue de l'obtention du diplôme de : Philosophiæ Doctor
a été dûment acceptée par le jury d'examen constitué de :

M. NERGUIZIAN Chahé, Ph. D., président
M. LAURIN Jean-Jacques, Ph. D., membre et directeur de recherche
M. FRIGON Jean-François, Ph. D., membre et codirecteur de recherche
M. WU Ke, Ph. D., membre
M. KISHK Ahmed A., Ph. D., membre externe

RÉSUMÉ

La section efficace du radar (SER) pour des cibles automobiles a une réponse angulaire étroite. Une variation de plusieurs décibels par mètre carré (dBsm) peut également être observée avec un léger changement de l'orientation de la cible. La localisation de telles cibles est difficile pour un radar automobile. En outre, un matériel complexe est généralement nécessaire pour mettre en œuvre un radar efficace, ce qui se traduit par des systèmes coûteux qui ne sont abordables que dans les véhicules haut de gamme. Cela défie l'objet d'un système de sécurité pour éviter les accidents de la route à grande échelle. Cette thèse présente une nouvelle balise d'amélioration de SER et une antenne multifaisceaux pour des applications de radar automobile. Ces composants peuvent éventuellement améliorer les performances d'un algorithme de super-résolution, et permettre le développement d'un radar d'évitement de collision automobile simple et peu coûteux. Une architecture de système simple et rentable est particulièrement importante dans la gamme de fréquences d'ondes millimétriques, allouée pour cette application, où les atténuations du signal et les coûts de dispositif sont significativement élevés. Les structures proposées dans cette thèse peuvent également trouver des applications dans d'autres applications en ondes millimétriques.

Un système radar est analysé en étudiant les propriétés de l'algorithme de super-résolution bien connu ESPRIT. Sur la base d'une simulation numérique MATLAB de cet algorithme, il est établi qu'une SER stable est importante pour l'utilisation de cet algorithme dans des applications automobiles. Ceci peut être réalisé en équipant la cible d'un marqueur d'amélioration de la SER. Deuxièmement, dans cet algorithme, la taille du réseau de récepteurs détermine le nombre de cibles détectables. En sectorisant le CdV du radar en utilisant une antenne multifaisceaux, l'erreur de localisation angulaire peut être réduite pour un plus grand nombre de cibles.

La balise proposée est conçue à 77 GHz, fonctionnant dans la bande attribuée au radar automobile (76 GHz à 81 GHz). Les caractéristiques des radars automobiles dans la littérature suggèrent un CdV en forme de faisceau en éventail pour la balise avec un CdV plus large dans le plan azimutal. De CdV de 120^o et 9^o dans les plans d'azimut et d'élévation sont respectivement choisis comme critères de conception pour la balise proposée. La propriété de rétroréflexion dans le plan d'azimut aide à améliorer la SER de la balise. La balise proposée reflète le signal incident avec une rotation de polarisation linéaire de 90^o. Cette modulation de polarisation permet d'améliorer la visibilité de la cible par rapport au bruit de fond. De plus, une modulation d'amplitude est également implémentée dans la balise. Cette modulation

peut aider à communiquer des informations supplémentaires ainsi que faciliter la détection de la cible en améliorant le rapport signal sur bruit du signal reçu traité.

Un nouvel élément rayonnant est proposé pour obtenir une balise avec le CdV désiré. Cet élément rayonnant est constitué d'une cavité rectangulaire fonctionnant dans son mode fondamental pour réaliser une structure compacte. La cavité est couplée à un guide d'onde intégré au substrat (SIW) en utilisant une fente de couplage. Une fente de résonance est placée sur le dessus de cette cavité pour un rayonnement de polarisation linéaire. L'état de polarisation peut être modifié en changeant l'orientation de la fente rayonnante sur la cavité. Des réseaux unidimensionnels compacts avec une largeur de faisceau demi-puissance d'environ 9^o dans le plan de réseau sont conçus et fabriqués pour couvrir le CdV dans le plan d'élévation de la balise. Ces réseaux sont conçus pour avoir une petite largeur de $0,47\lambda$ à 77 GHz. Cette largeur permet d'obtenir une petite distance entre les éléments dans le plan azimutal pour obtenir un CdV azimutal de 120^o avec une propriété de rétroréflexion, sans élever les lobes secondaires. Des réseaux unidimensionnels et bidimensionnels ont été prototypés pour deux états de polarisation orthogonale afin de valider les caractéristiques de formation de faisceau et de bande passante.

La balise est réalisée en agençant des réseaux unidimensionnels avec deux polarisations orthogonales dans une configuration de réseau Van-Atta le long du plan d'azimut. Une configuration de mesure a été établie pour évaluer la SER monostatique et bistatique de la balise fabriquée. Une comparaison de la SER de la balise avec les réflexions d'une plaque d'aluminium plate montre une amélioration de 15-20 dBsm. Un large CdV rétro-réfléchissant en azimut et un étroit élévation sont également validés pour le prototype fabriqué. Les résultats de simulation et de mesure sont comparés pour évaluer les tolérances de fabrication.

Comme moyen de moduler le signal réfléchi par la balise, une nouvelle topologie de commutateur dans la technologie guide intégré dans le substrat (SIW: Substrate Integrated Waveguide) est proposée. Le commutateur est réalisé en implémentant une charge commutable sur un SIW. À cet effet, une fente résonante en série sur un SIW est utilisée. L'impédance de la fente est commutée en couplant la fente avec une diode PIN en son milieu. La polarisation directe de la diode PIN fait basculer la fente résonante dans un état non résonant, éliminant ainsi l'impédance de résonance élevée de la ligne de transmission. Un commutateur entièrement fonctionnel est implémenté dans la bande K. Un commutateur câblé en bande W est utilisé pour démontrer la modulation d'amplitude dans de balises proposée. Une variation d'amplitude de 15 dB a été observée pour les prototypes de balises avec un commutateur à l'état passant ou bloqué.

Enfin, une nouvelle antenne multifaisceaux est proposée pour sectoriser le CdV du radar.

Cette antenne imprimée à faible coût comporte une seule couche de substrat implémentant une lentille de Luneburg, qui est utilisée dans le réseau de formation de faisceaux réalisant l'antenne multifaisceaux proposée. La lentille génère un faisceau focalisé avec un plan équiphase qui peut être incliné en faisant pivoter l'excitation le long de la circonférence de la lentille. Cette inclinaison du plan équiphase est utilisée pour exciter un réseau en phase avec une phase progressive qui dirige le faisceau rayonné. Une antenne à sept faisceaux est conçue à 77 Ghz pour atteindre une plage de direction de faisceau de $\pm 41^o$ et est fabriquée pour valider la lentille de Luneburg proposée et le réseau de formation de faisceau.

La balise proposée et l'antenne multifaisceaux forment essentiellement le sous-système rayonnant d'un système d'évitement de collision par ondes millimétriques utilisant un algorithme de super-résolution. La tag améliore la SER de la cible, ce qui améliore le rapport signal sur bruit du signal réfléchi, nécessaire pour améliorer la performance de l'algorithme de super-résolution pour cette application. L'antenne multifaisceaux permet d'augmenter le nombre de cibles détectables en utilisant une super-résolution dans le CdV du système avec un nombre limité d'éléments rayonnants dans le réseau de récepteurs. L'architecture du système est proposée dans cette thèse. Les caractéristiques mesurées des composants conçus peuvent être utilisées pour évaluer les performances du système proposé.

ABSTRACT

Rear radar cross section (RCS) of automotive targets has a narrow angular response. A variation of several decibel per square meter (dBsm) can also be observed with slight change in the target orientation. Localization of such targets is challenging for an automotive radar. Furthermore, complex hardware is typically required to implement an effective radar resulting in high-cost systems that are affordable only in high-end vehicles. This defies the object of a safety system to avoid roadside accidents at large scale. This dissertation presents novel RCS enhancing tag and multibeam antenna for automotive radar applications. These components can possibly improve the performance of a super-resolution algorithm, and enable the development of a simple, low-cost automotive collision avoidance radar. Simple and cost-effective system architecture is particularly important in millimeter wave frequency range, allocated for this application, where the material losses and device costs are significantly high. The proposed structures in this thesis can also find applications in other millimeter wave applications.

A radar system is analyzed by studying the properties of Estimation of Signal Parameters via Rotational Invariance Technique (ESPRIT), a well know super-resolution algorithm. Based on a MATLAB numerical simulation of this algorithm, it is established that a stable target RCS is important for employing this algorithm in automotive applications. This can be achieved by equipping the target with a RCS enhancing tag. Secondly, in this algorithm, the size of the receiver array determines the number of detectable targets. By sectoring the radar field of view (FoV) using a multibeam antenna, the localization error can be reduced for higher number of targets.

The proposed tag is designed at 77 GHz, operating in the band allocated for automotive radar (76 GHz to 81 GHz). Automotive radar characteristics in the literature suggest a fan-beam shaped FoV for the tag with wider FoV in azimuth plane. Azimuth and elevation plane FoV of 120^{o} and 9^{o} are selected as design criteria for the proposed tag. Retroreflection property in the azimuth plane helps to improve the tag RCS. The proposed tag reflects the incident signal with 90^{o} linear polarization rotation. This polarization modulation can enhance the target visibility against the background clutter. Additionally, an amplitude modulation is also implemented in the tag. This modulation can help to communicate additional information. It can also facilitate the target detection by improving the signal to noise ratio of the processed received signal.

A novel radiating element is proposed to achieve the desired tag FoV. This radiating element

consists of a rectangular cavity operating in its fundamental mode to achieve a compact structure. The cavity is coupled with a substrate integrated waveguide (SIW) using a coupling slot. A resonant slot is placed on the top of this cavity for linear polarization radiation. The polarization state can be changed by changing the radiating slot orientation on the cavity. Compact one-dimensional arrays with approximately 9° half-power beamwidth in the array plane are designed and fabricated to cover the elevation plane FoV of the proposed tag. These arrays are designed to have a small width of 0.47λ at 77 GHz. This width allows to achieve small interelement distance in azimuth plane to cover 120° azimuth FoV with retroreflection property, without raising grating lobes for small arrays. One- and two-dimensional arrays were prototyped for two orthogonal polarization states to validate the beamforming and bandwidth characteristics.

The tag is realized by arranging one-dimensional arrays with two orthogonal polarizations in a Van-Atta array configuration along the azimuth plane. A measurement setup was established to assess monostatic and bistatic RCS of the fabricated tag. A comparison of the tag RCS with reflections from a flat aluminium plate shows 15-20 dBsm of RCS enhancement. Wide retroreflective azimuth FoV and narrow elevation FoV are also validated for the fabricated prototype. Simulation and measurement results are compared to evaluate the fabrication tolerances.

As a mean to modulate the tag reflected signal, a novel switch topology in SIW technology is proposed. The switch is realized by implementing a switchable load on an SIW. A series resonant slot on an SIW is used for this purpose. The slot impedance is switched by coupling the slot with a PIN diode at its middle. Forward DC-biasing of the PIN diode switches the resonant slot in non-resonant state, eliminating the high resonance impedance from the transmission line. A fully functional switch is implemented in K-band. A hardwired switch in W-band is used to demonstrate amplitude modulation in the proposed tag. Amplitude variation of 15 dB was observed for tag prototypes with on- and off-state switch.

Finally, a novel multibeam antenna is proposed to sector the radar FoV. This printed, low-cost antenna features a single substrate layer implementation of Luneburg lens which is used in a beamforming network that realizes the proposed multibeam antenna. The lens generates a focused beam with an equiphase plane which can be inclined by rotating the excitation along the circumference of the lens. This equiphase plane inclination is used to excite a phased array with a progressive phase which steers the radiated beam. A seven-beam antenna is designed at 77 GHz to achieve $\pm 41°$ beam steering and fabricated to validate the proposed Luneburg lens and beamforming network.

The proposed tag and multibeam antenna essentially form the radiating subsystem of a mil-

limeter wave collision avoidance system using super-resolution algorithm. The tag enhances the target RCS that improves the signal to noise ratio of the reflected signal, necessary to improve the super-resolution algorithm performance for this application. Multibeam antenna helps to increase the number of detectable targets using super-resolution within the system FoV with limited number of radiating elements in the receiver array. The system architecture is proposed in this dissertation. The measured characteristics of the designed components can be used to evaluate the proposed system performance in the future.

TABLE OF CONTENTS

LIST OF TABLES

LIST OF FIGURES

LIST OF ACRONYMS AND ABBRIVIATIONS

AF	Array Factor
AICC	Automatic Intelligent Cruise Control
BFN	Beam Forming Network
CW	Continuous Wave
DF	Direction Finding
DoA	Direction of Arrival
ESPRIT	Estimation of Signal Parameters via Rotational Invariance Techniques
FMCW	Frequency Modulated Continuous Wave
FoV	Field of View
HPBW	Half-Power Beam Width
LNA	Low Noise Amplifier
LRR	Long Range Radar
MMIC	Monolithic Microwave Integrated Circuit
MUSIC	MUltiple SIgnal Classifier
PCB	Printed Circuit Board
RCS	Radar Cross Section
RF	Radio Frequency
SIW	Substrate Integrated Waveguide
SLL	Side Lobe Level
SNR	Signal to Noise Ratio
SPST	Single Pole Single Throw
SRR	Short Range Radar
TE	Transverse Electric
TEM	Transverse ElectroMagnetic
TM	Transverse Magnetic
VCO	Voltage Controlled Oscillator
VNA	Vector Network Analyzer

LIST OF APPENDICES

CHAPTER 1 INTRODUCTION

1.1 Problem description

With the increase in vehicle density on roads, the necessity of driver assistance systems is becoming more eminent and crucial to avoid fatal accidents. Studies have shown that 90% of fatal accidents involve human error or negligence and these accidents are avoidable if drivers take certain measures before the accidents. It is observed that the collision probability is reduced to less than 5% for certain type of accidents (head-on, rear and intersection collisions) if the drivers' response time can be decreased by only two seconds [1].

Automotive industry and governments are trying to reduce fatal accidents that claim approximately 1.2 million lives per year all over the world. It is not only a human atrocity but also an enormous economic loss to the affected entities. For these reasons, automobile manufacturers are putting great efforts to develop reliable safety systems which can be produced at mass level.

Safety systems can be categorized in two major classes, namely active and passive systems. Active systems help to avoid accidents whereas passive systems are designed to reduce injuries after accidents. Passive systems involve seat belts, air bags, safe materials and vehicle designed to minimize injuries after accidents. Previously, automobile manufacturers mostly concentrated their efforts to improve passive safety systems. However, this trend is rapidly shifting towards active safety systems.

Active safety systems consist of sensors providing surrounding awareness. There are many ways to sense the environment. Laser sensors transmit and receive light pulses to see a target. However, in rainy and dusty conditions, the laser system performance deteriorates due to light scattering and absorption. Ultrasound sensors use sound waves in higher inaudible frequency ranges, but these systems are not efficient for wide field of view (FoV), for measuring the velocity of the target and in rainy conditions. Video cameras provide low-cost and flexible solutions to sense the environment. In spite of good target identification properties due to advances in computer vision, visual sensors cannot work in bad weather and light conditions. Infrared sensors use a frequency band between microwaves and visible range. Though they provide good resolution and night vision, they can operate efficiently only for short ranges. Radar sensors, on the other hand, use microwaves in gigahertz frequency range. Although it is difficult to identify a target, radar sensors provide direct speed and target range estimations in practical road conditions and operate efficiently in almost all weather conditions.

An efficient safety system integrates many sensors along with road and traffic information. However the capability of radar systems to operate in all weather conditions and directly provide the range information make them an essential component of automotive safety systems, and an active research topic in this field.

1.2 Brief history

Radar systems for automotive applications are under development since the early seventies. High radar operating frequency is desirable as it results in compact sized systems that can be mounted on small vehicles. Technical difficulties associated with early experiments slowed down the development process. An initial test setup operated at 10 GHz [2]. Due to its large size, it was mounted on the top of a sedan vehicle. It was followed by a 16 GHz setup that was installed on the front bumper of a sedan in the middle seventies [2]. Recent developments in electronics and fabrication technologies have accelerated the automotive safety system development due to fabrication feasibility of high frequency components.

In addition to 10 GHz and 16 GHz, different radar systems operating in 24 GHz, 35 GHz, 47 GHz, 60 GHz and 94 GHz were also tested [2]. In 2001, a 5 GHz band centered at 24 GHz was temporarily allocated for short range automotive radar in the European Union and United States due to the availability of components at that frequency. Japan selected the 60 GHz band due to possible integration of safety systems with inter-automobile communication that takes place in this frequency band. However, as 24 GHz and 60 GHz bands are used by other applications, it was proposed by the European Union to replace it by 76 GHz to 81 GHz frequency band in 2013. Due to delays in development of safety systems in the 77 GHz band, utilization of the 24 GHz band has been extended by European Commission. However, future development of the automotive radars is forced in the 76-81 GHz frequency band. It will allow different regions and companies to develop components that are compatible with each other.

The first commercially deployed radar safety system was the front looking Eaton-Vorad anti-collision system. It was installed on Greyhound busses and trucks in 1992 [2]. It consisted of a narrow beam antenna with 5^o half power beamwidth (HPBW) that was mechanically steerable to $\pm 20^o$ and operating at 24.15 GHz frequency [3]. It was designed to warn the driver for possible collision. This installation reduced the accidents per kilometer travelled by more than 50%.

The timeline for the development of the millimeter wave systems from 1992 to 1997 is described in [4]. Development of millimeter wave systems for automatic intelligent cruise control

(AICC), forward looking radar, automatic soft braking and lane changing aid are discussed in [5]. The first commercially available safety system (DISTRONIC) for sedan was introduced in Mercedes-Benz S-class vehicles in 1998. It was operating at 77 GHz and was replaced by the improved DISTRONIC PLUS eight years later. This new system consisted of a 77 GHz long range radar (LRR) for AICC and 24 GHz short range radar (SRR) for collision avoidance [2].

Early active systems were designed to assist the driver. They were used for applications like AICC, parking aid, lane change assist and blind spot monitoring. Currently developed safety systems, such as Tesla Autopilot, process data from multiple sensors such as camera arrays, ultrasonic sensors and radar system using complex algorithms to form a reliable safety system.

1.3 Objectives and Contributions

1.3.1 Objectives

The purpose of this work is to explore solutions that can lead to the development of a possible low-cost and effective collision avoidance system which can be produced on a large scale. Developing an automotive radar system is a challenging task. In addition to strict performance constraints, size, cost and working environment constraints multiply the design intricacy and challenges.

The radar cross section (RCS) of different cars is quite complex and vary based on manufacturer and model of the car. This RCS also varies significantly (in range of 10 dBsm) with slight variation of the target orientation with respect to the radar. Furthermore, multiple targets (cars, motorcycle, road signs, pedestrians, etc.) can be present in the radar field of view (FoV). Complex hardware and software techniques are required to reliably observe and identify these types of targets.

A first specific objective of this work is to propose a possible system with reduced hardware complexity, using super-resolution algorithms in an automotive radar for target positioning. Estimation of Signal Parameters via Rotational Invariance Techniques (ESPRIT) is simulated in MATLAB on the signal reflected by automotive targets to characterize the super-resolution algorithm for this application and propose an automotive radar system.

Secondly, it is proposed to improve automotive target detection by the radar by designing a tag which decreases the RCS sensitivity to the target orientation and improves the visibility of the target. This tag can also be installed on any desired object, like signs along the road, to generate radar beacons to communicate additional information. Additionally, the

signal reflected by the tag can also be modulated with a code for unique identification of the target and also to improve the reflected signal for target detection and signal processing. Tag modulation mechanism is therefore also explored in this work.

According to the ESPRIT algorithm, if a particular region is illuminated by a transmitter then the number of observable targets is limited by the number of antenna elements in the receiver array. As this number is limited, a third specific objective is to develop an antenna system to divide the whole FoV into smaller sectors where each sector is further illuminated by a signal which is orthogonal with respect to the other sectors. This sectoring along with tagging the target and use of the ESPRIT algorithm can result in a simpler system that can reliably detect the target position.

1.3.2 Original Contributions

Below are the major original contributions of this dissertation.

- **Developing a retroreflector tag for an automotive target to reduce its RCS complexity:**
  A tag at 77 GHz with polarization and amplitude modulation to increase the visibility of an automotive target to the radar was developed. The tag consists of compact sized radiating elements that can be arrayed together to achieve 120^o field of view (FoV) with retroreflection in azimuth plane and 9^o FoV in elevation plane. These radiating elements can also be designed for an arbitrary linear polarization. One- and two-dimensional arrays of these elements were designed and tested to validate the design criteria of these elements. One-dimensional arrays were also configured as Van-Atta array to develop a retroreflector to minimize the automotive target RCS variations for wide FoV and target orientation.

- **Novel amplitude modulation technique for the retroreflector:**
  A novel amplitude modulation technique is proposed for the designed retroreflector. This technique is based on loading a substrate integrated waveguide (SIW) with a variable load. The load is a series slot on an SIW, coupled with a PIN diode. This simple technique can be used to effectively modulate the signal reflected from the retroreflector.

- **Multibeam transmit antenna for sectoring the radar FoV to enhance the super-resolution algorithm performance:**
  A novel Luneburg lens-based printed multibeam antenna in W-band is proposed to sector the whole FoV of an automotive radar. The proposed antenna can provide

flexible solution in this regard. The number of sectors can be easily changed by varying the lens diameter used in the proposed antenna structure. Printed circuit board (PCB) process is used to fabricate the proposed structure and provide flexible yet comparable performance in comparison with the available multibeam antenna structures.

1.4 Dissertation Outline

This dissertation reviews the available technique and methods used in automotive radar and aims to propose a simple structure for this purpose. Components of the radiation subsystem of the proposed system are designed, analyzed and fabricated. The proposed system front end implementation, baseband modulation signals, link budget analysis and system performance characterization are proposed as future work. The different chapters of this dissertation are briefly described below.

Chapter 2 reviews the state-of-the-art systems and techniques that are available in the literature, covering different aspects of automotive radar. Based on this knowledge and the simulations of ESPRIT algorithm, a system is proposed in Chapter 3. The radiating elements of the proposed retroreflective tag are designed and prototyped in Chapter 4. An SIW switch is presented in Chapter 5 to introduce amplitude modulation of the signal reflected by the tag. The retroreflector structure is developed in Chapter 6. A multibeam antenna structure is proposed in Chapter 7 for the transmitter of the proposed system. Chapter 8 concludes this dissertation and recommends possible future work.

CHAPTER 2 LITERATURE REVIEW

Published work related to automotive collision avoidance systems can be subdivided into several sections such as automotive radar requirements, modes of operation, super-resolution algorithm, beamforming and automotive target characterization. The literature related to those topics is discussed in this chapter.

2.1 System Requirement

The first step to develop a system is to understand its requirements. The system requirements for an automotive radar vary from manufacturer to manufacturer. In [6] and [7], requirements for an automotive radar are described by researchers associated with General Motors. In general, forward looking automotive radar can be divided into two major parts. One is AICC and the other part is anti-collision system. AICC should have a range of 200 m with 18^o azimuth FoV. The angular resolution within this FoV should be 2^o. Similarly, the range and azimuth FoV for anti-collision system should be 60 m and 120^o, respectively, with azimuth angle resolution of 5^o. The overall size of the system should be $90 \times 70 \times 25$ mm^3 ($W \times H \times D$). The total power consumption should be in the range of 10-20 mW. Furthermore, the collision avoidance system should be able to detect 20 different targets and its response time should be less than 50 milliseconds.

The importance of the elevation direction of arrival (DoA) sensing is described in [8]. It is possible that on-road or overhead installations appear as desired targets to the radar sensor if there is no information about the elevation DoA. It is proposed to use monopulse in the elevation plane to solve this problem. Using monopulse, it is possible to detect that the reflection is coming from either ground or overhead installations [6].

2.2 Mode of Operation

In general, the automotive radar system implementation can be divided into two major categories, namely, continuous wave and pulse-based radar systems. In [9], a pulse-based automotive radar operating at 24 GHz is proposed. A network of four sensors, transmitting narrow pulses of width 1 ns, precisely detect multiple target positions within an error margin of 3 cm. Delayed pulses received by each sensor provide a locus of the possible target position. By combining these possible target positions estimated by the individual sensors, precise target location can be estimated. An automotive radar system based on similar

principles is also presented in [10] and [11]. Range resolution improvement of a pulse-based radar is proposed in [12]. However the detectable range of the target is very low due to pulsed nature of the system that cannot transmit high average power with the available hardware technology. Moreover, use of multiple sensors and synchronization requirements between these sensors make this system complex and expensive.

Continuous wave radar systems are more popular due to the higher average transmitted energy. In [13], a frequency modulated continuous wave (FMCW) based AICC radar is simulated using advanced design system (ADS) and MATLAB. A double triangle FMCW waveform is used for this purpose. The front end monolithic microwave integrated circuit (MMIC) components such as the voltage controlled oscillator (VCO), amplifiers, low noise amplifier (LNA), frequency multiplier and mixers are modeled by the data provided by the vendors. Other system components like couplers and transitions are modeled by their S parameters obtained from full-wave simulators. In this reference, small targets like pedestrians and motorcycles are modeled by constant RCS with respect to range and angle of arrival whereas large targets like trucks and cars RCS are a function of the distance from the radar. The received signal is processed in ADS and signal processing improvements are implemented in MATLAB. Continuous wave radar transceiver for automotive applications are also reported in [14] and [15].

In [16], the effect of antenna beamwidth is studied using a co-simulation model in which the RF front-end simulation is carried out in ADS and the antenna, channel and targets are incorporated in a 3D ray tracing environment where different traffic scenarios can be simulated. Signal received at the receiving point can be weighted and summed to get a desired radiation pattern of the receiving antenna array. Antenna pattern with 3 dB beamwidth of 20^o, 10^o and 5^o are studied. Additionally, the effects of the sidelobe levels (SLL) are also studied in this work. It is shown that a wider beamwidth illuminates unwanted targets like roadside installations that appear as targets in the beat frequency spectrum. Similarly, the side lobes can illuminate the targets that are not in the desired directions and cause ambiguities. Channel modeling using ray tracing is also used in several other articles like [17], [18] and [19]. A review of different continuous wave systems is presented in [20].

In [21], different FMCW waveforms are discussed. It is stated that a single triangle FMCW cannot detect multiple targets. So a dual FMCW waveform is proposed to get the beat frequencies associated with different targets. Dual FMCW waveform has two triangles with different slopes. Each slope will give a different beat frequency for each target and using these frequencies, we can estimate the distance and speed of the target. Additionally, a three segment FMCW waveform is also proposed where one segment has zero slope allowing

the continuous wave signal to detect the doppler frequency of all the targets and using single triangle FMCW to get the distance of multiple targets. Performance analysis of these techniques is also presented in this reference.

2.3 Target Localization Techniques

In order to locate a target, it is required to estimate its DoA. A pulse-based radar uses multiple sensors to estimate DoA whereas in continuous wave radar, DoA can be estimated by either using high gain antennas where DoA resolution is determined by the antenna beamwidth or it can be estimated using statistical analysis of the signal received by an antenna array. Though narrow beamwidth antenna system provides simple and robust method to detect the DoA, it remains difficult to develop an efficient system that cover a wide FoV of 120^o.

2.3.1 Beamforming Techniques

In [22], a beamforming antenna system is introduced using a dielectric lens. The dielectric lens is fed by patch antennas placed along a line that passes through the focal point of the lens. Exciting a patch placed at the focal point generates a beam with 28 dB directivity in Ka band. By exciting adjacent radiating elements with proper phase and amplitude, a wider beam can be achieved. Similarly by exciting off-centered feeding elements, the main beam can be scanned. A beamforming network that excites the patches with specific phase and amplitude is required to get the desired beam. However this technique produces deteriorated beam patterns when using longer feed arrays.

In [23], the implementation of Luneburg lens is presented. The lens is formed by shaping a dielectric slab inserted in a parallel plate waveguide in order to produce an effective index of reflection profile that obeys Luneburg's law. The lens is fed by linearly tapered slot antenna properly positioned within the waveguide to avoid unnecessary modes. Effect of positioning the phase center of the feed antenna on the focal point position is analyzed experimentally. A fan beam was generated using this lens with the lens focusing along one principle axis and wider beam at the other axis.

In [24], a neural network based DoA estimation technique is proposed. Firstly, a Nolen Matrix based beamforming network is developed to estimate 2D DoA from a 90^o cone in front of the transmitting antennas. In each dimension, two transmitting antennas generate three different signals that are fed to a neural network program to estimate the DoA. It is reported that the DoA error reduces with increase in signal to noise ratio (SNR) and this error is lower for smaller angles due to higher density of training samples for those angles in

comparison to the higher angle values.

In [25], digital beamforming is introduced to achieve high resolution beam scanning. In traditional systems, physical phase shifters are used to control the phase added to each antenna in an array to direct the beam in the desired direction. In case of the switched phased-array-antenna system, each antenna is switched, and the received signal is downconverted, sampled and stored in the signal processing unit. These samples can be multiplied with phase and added together in a signal processing unit to form a beam. Hence we can digitally form a beam without analog radio-frequency phase shifters. This type of beamforming requires very fast switching but it can achieve higher angular resolution. An FMCW based switched phased-array-antenna system was implemented and tested in this reference.

In [26], different antenna topologies used in automotive radar systems are reviewed. These antenna beamforming can be divided into three major categories. The first one is reflector and lens antenna in which the feeding element illuminates a polarization grid that reflects the signal to a polarizer as shown in Figure 2.1. The polarizer rotates the signal polarization such that this signal can pass the polarization grid. Periodic structures on the polarizer control the phase and hence focus of the transmitting signal. The second category covers planar antennas that consist of printed structures, slots and periodic perturbations in waveguide.

In [27], design and beamforming for different planar structures is discussed with reported examples in the literature. Beamforming using dielectric lens, Rotman lens, series, corporate and hybrid arrays are reported for mm-wave range. Especially, the design of series feed patch antenna array is discussed in detail. Additionally, monopole and dipole antennas are also reported in this reference.

2.3.2 Super-Resolution Techniques

When DoA is estimated using statistical analysis of the signal received by an antenna array, the antenna beamwidth can be much wider in comparison to the angular resolution provided by the analysis. This is why these methods are called super-resolution methods as target's angular position can be resolved within the antenna beamwidth. This is an attractive alternative to cover a wide FoV with high resolution as in the case of automotive radar. However these techniques are sensitive to the strength of the signal returned from the target.

A review of direction finding (DF) techniques is given in [28]. These techniques are divided into two different categories, namely conventional DF and high resolution DF. Conventional DF includes spinning, multilobe and digital beamforming. In case of spinning DF, the receiver is rotated with a specific speed which depends on the target range. A narrow beamwidth

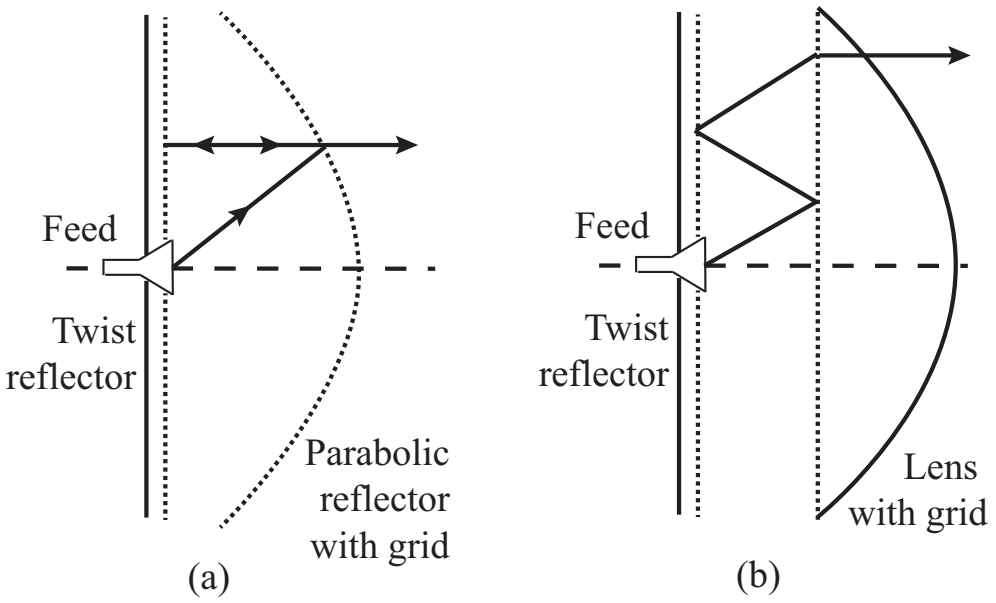

Figure 2.1 Reflector and lens antenna topology (a) Folded reflector and (b) Lens antennas [26].

antenna provides accurate target position however it can miss the target if the rotating speed is very high for a long range target for a radar using spinning DF technique. In this case, the reflected signal may arrive at the antenna after the main beam is rotated away from the desired direction. There is a compromise between the target miss rate and target position. Additionally, mechanical constraints associated with this type of DF also affect the system performance.

Multilobe DF systems consist of fixed antennas pointing multiple beams in different directions. Comparison of amplitude, phase or both amplitude and phase of the signal received by the these antennas gives the information about the location of the target. Though this method has no moving parts, it suffers in multi-path and multi-target environments. Digital beamforming also falls in the conventional DF category.

Probably the first high-resolution DF method was Capon's method that forms a null to one target and tries to find another maxima (target) in the rest of FoV. However placing nulls at a certain location reduces the available antenna elements to form directional beam in other directions hence the resolution is reduced.

All the above methods do not distinguish between the desired (signal reflected by target) and undesired signals (signal reflected by background). However, if by some means we can distinguish between desired and undesired signals received by the antenna array (that is usually done by defining a signal energy threshold), we can form a beam towards only desired

signals with high resolution. MUltiple SIgnal Classification (MUSIC) and Estimation of Signal Parameters through Rotational Invariance Techniques (ESPRIT) are based on this technique. Using eigenvalue decomposition method, the desired signals are separated from the undesired signals. MUSIC algorithm estimates the weights of the array elements that provide maxima or null in the direction of desired signals, whereas ESPRIT algorithm uses spatial displacement to estimate the direction of arrival of the signal.

In [29], the basics of DF algorithms are described in detail. It is stated that in general, high-resolution DF algorithm are sensitive to the SNR of the signal coming from the target. If two targets are half antenna beamwidth apart, then in order to detect these targets, the SNR should be four times greater than when the targets are a full beamwidth apart of the same antenna. This high SNR requirements limits the application of high-resolution algorithms in automotive radar application.

In [30], an improved version of [25] is presented. If transmitting antenna array elements are also switched in addition to the receiving antenna elements, we can reduce the number of receiving antenna elements. By adding certain phase in each transmitting antenna element relative to the first transmitting antenna, we can also practically multiply the physical array size by the number of the switched transmitting antennas hence reducing the number of receiving channels and the system complexity. A system is developed in this reference to demonstrate this concept. In order to resolve the angular resolution, the authors used high resolution algorithm (ESPRIT algorithm) instead of digital beamforming as digital beamforming provides less angular resolution in comparison with the ESPRIT algorithm.

In [31], DoA estimation technique for two targets using three receiving antennas is proposed. Just like Capon's method, the proposed system places the nulls at the location of the target using digital beamforming. Once minimum signal level is achieved, the target position can be determined by finding the location of the nulls in the array factor. This technique has low computational load in comparison with the high resolution algorithm however we need to calibrate the system before applying this algorithm as practical errors in the array factor will cause estimation errors. The calibration is done by measuring the array factor for a single target placed at different locations. The system performance can also be improved by having multiple snapshots.

In [32], sixteen receivers and one transmitter are used to apply MUSIC algorithm to get high azimuth resolution in an automotive radar. The estimator performance decreases with an increase in coupling between the antennas (increases signal correlation), phase mismatch (errors in estimated array factor) and fluctuation in SNR of different targets. The performance of the MUSIC algorithm can be improved by pre-processing the signal before applying the

algorithm that reduces the signal correlation.

2.4 Target Radar Cross-Section characterization

As mentioned earlier, the super resolution algorithms are very sensitive to the SNR of the signal reflected by the target. The SNR of the reflected signal depends on the RCS of the target. The RCS of an automotive target is complex due to the short target range from the radar transceiver. Instead of a single point target (for which super-resolution algorithms are formulated) the automotive target appears as an extended target that has many reflection points on a single target. This is equivalent to say that the radar antenna is not in the far-field distance from the target, although the target may be in the far-field of the antenna. So understanding the RCS of automotive targets is important in order to apply super resolution algorithms.

In [33], the RCS for different automotive targets are measured experimentally. A signal from port 1 of a vector network analyzer (VNA) is transmitted using a horn antenna connected to this port. The reflected signal from the target is received by another horn antenna connected to the port 2 of this VNA. Fourier transform of this signal gives the distance information as time is related with distance as a function of speed of light. The target is placed at a distance of 17 m on a 360^o turn table. Horizontal and vertical polarizations are used to get the RCS. It is reported that the horizontal polarization is more robust to the ground reflection clutter such as road surface whereas the target features are independent of the polarization. Cadillac STS sedan, Avalanche pickup truck, Express van, bicycle, motorcycle and adult pedestrian RCS are observed with horizontal polarization. RCS variation of 30 dB is observed in azimuth FoV for large targets like trucks.

In [34], statistical models of RCS for twenty five different personal vehicles are presented. The target vehicle is placed at 40 m and it is illuminated with a wideband signal covering 91-97 GHz frequency range by a conical beam of 1.5^o. The measurement was made for thirty different aspect angles at the rear of the target. The received data best fit with a Weibull distribution random variable[1] with shape (k) and scale (λ) parameters in comparison with log-normal and gamma distributions. Based on this, a dummy target is formed to act as a surrogate test target for testing the millimeter wave safety systems without harming the test driver and car.

[1]
$$f(x;\lambda,k) = \begin{cases} \frac{k}{\lambda}\left(\frac{x}{\lambda}\right)^{k-1} e^{-(x/\lambda)^k} & \text{if } x \geq 0 \\ 0 & \text{otherwise.} \end{cases}$$

In [35], pedestrian RCS is measured using CW system at 76 GHz. The target is placed in an anechoic chamber on a turn table at 5 m distance. The average measured RCS is -8 dBsm with variance of 20 dB. RCS variance with different clothes is about 12 dB. Similarly, RCS of a bicycle is characterized in [36].

2.5 Conclusion

Based on this literature review it can be concluded that the available collision avoidance system consists of a long range, narrow FoV continuous-wave system and a short-range, wide FoV pulse-based system. Targets are localized by using pulses travel time and beamforming. Target localization using super-resolution algorithms is also presented in this literature review. It is perceived that employing super-resolution algorithms for automotive collision avoidance system can simplify the resulting hardware by combining the continuous-wave and pulse-based systems. Hence, a single system can replace multiple sensors currently used for collision detection and avoidance. Based on MATLAB simulations, a radar system is proposed and partially developed in the following chapter in order to utilize super-resolution algorithm for collision avoidance applications.

CHAPTER 3 PROPOSED SUPER-RESOLUTION BASED COLLISION AVOIDANCE SYSTEM

In order to simplify the system architecture, super-resolution based target localization is proposed for collision avoidance applications. This system is developed in this chapter. Firstly, target localization technique is selected. Characteristics of classical super-resolution algorithms are studied to select an algorithm for the architecture development. Finally, a system is proposed by analyzing the performance of the selected super-resolution algorithm by using a MATLAB simulation.

3.1 System mode and DoA technique selection

As mentioned in the literature review, CW systems have an advantage over pulse-based systems with respect to radar range. Similarly, in order to cover a 120^o FoV, wide beamwidth antenna with a super-resolution algorithm can result in a simple system design in comparison with narrow beamwidth antenna systems that either require beam switching or mechanical scan. In the following sections, we therefore analyze a CW radar system using a super-resolution algorithm.

3.2 DoA algorithm selection

After selecting the mode of operation (CW system) and DoA finding technique, the next step is to select a DoA algorithm appropriate for the given application. Azimuth angle of arrival for a signal received by an antenna array whose beamwidth is wider than the required angle resolution is generally estimated using high-resolution algorithms. MUSIC and ESPRIT algorithms are classical examples of such algorithms. MUSIC algorithm is used in [32], [37], [38] and [39] to detect the DoA for radar applications. Similarly [30] and [40] are two examples of the application of the ESPRIT algorithm in radar systems.

In order to select a super-resolution algorithm for our system, it is important to understand the basics of these algorithms. As mentioned in the literature review, both algorithms separate the desired signals from the undesired ones using eigenvalue decomposition. It is done by developing a dataspace using vector matrix formed by taking a time sample (snapshot) from each element in the antenna array. A matrix is then formed where each row represents one snapshot of data from the antenna array elements at a given time. This matrix is multiplied by its transpose matrix to form a correlation matrix. Once the correlation matrix is

formed, its eigenvalue decomposition provides eigenvalues of the independent signals in the dataspace. Eigenvalues above a certain threshold are considered as desired signals and form a signal subspace. It is important to note that the signal reflected by different targets should be independent and narrow-band. However in case of automotive radar, the statistical nature of automotive targets' RCS and FMCW modulation with appropriate bandwidth addresses these issues.

Once the signal subspace is separated, the MUSIC estimates the weights of the array elements to form a beam that has maximas or nulls (depending on the implementation of the algorithm) in the desired directions. These weights are used to develop an array factor which is known as the MUSIC spectrum. This spectrum is then parsed to get the desired angles by searching maximas or nulls in the spectrum. Below are a few important aspects of the MUSIC algorithm [29].

1. MUSIC algorithm requires large number of data snapshots to generate correlation matrix. The number of snapshots depends on the angular resolution of the targets and their SNR. Snapshots in range of tens of thousands might be required to get a desired accuracy. This is a very challenging requirement for a real-time system like automotive radar.

2. In general, super-resolution algorithms require high computational resources. In case of the MUSIC algorithm, the computation is involved in eigenvalue decomposition and searching the MUSIC spectrum for maximas or nulls.

3. In order to form a MUSIC spectrum, it is required to have accurate calibration of the antenna system. In practice, all array elements or the spacing between them might not be identical. These factors should be known accurately before forming MUSIC spectrum. Errors in calibration result in inaccurate DoA estimation. This factor can be more prominent in W-band with small signal wavelengths.

4. In general, SNR of the signal reflected by the target has an important impact on target detection and angular resolution of the super-resolution algorithm. A weak reflector in proximity of a strong reflector can be masked by the strong one.

5. Number of detectable target DoAs is one less than the total number of array elements (N-1).

On the other hand, the ESPRIT algorithm utilizes the displacement of two identical arrays to estimate the DoA in the signal subspace. This algorithm works with signals received by two

identical arrays that are displaced by some known distance in the desired DoA estimation plane. Consider two elements placed at known distance receiving a narrowband signal coming from a point source. Signals received by both elements will differ by a factor of $e^{j\beta l \sin\theta}$ where β is propagation constant , l is known distance and θ is the angle in the required DoA plane, between the normal to the array axis and the point target. Knowing this factor along with element spacing and propagation constant, we can find θ. However, in case of noise corrupted signals, estimation techniques are required to get the required DoA. Hence, if we have signals received by two identical arrays, displaced by a known distance, DoA can be estimated using statistical techniques. Below are a few important aspects of the ESPRIT algorithm [41].

1. ESPRIT algorithm is known as search-free algorithm which means that it does not require large number of snapshots to estimate DoA. Theoretically only one snapshot can estimate the DoA. However in practice averaging a few snapshots improve the DoA estimation performance.

2. ESPRIT is computational expensive just like MUSIC. However ESPRIT directly provides the desired angles i.e. parsing the array factor is not required in this case.

3. ESPRIT does not require calibration as it utilizes two identical arrays and the only difference between the signals received by the two arrays is the delay due to the displacement.

4. ESPRIT is also sensitive to the reflected signal SNR.

5. Number of detectable target DoAs depends on the length of the individual arrays.

By analyzing key points associated with the two algorithms, it can be observed that ESPRIT has advantage of being search-free and calibration independent algorithm. Though for the given number of target DoAs, the MUSIC algorithm needs half number of antenna elements in the array in comparison with ESPRIT algorithm yet ESPRIT algorithm can use overlapping arrays that greatly mitigates this disadvantage. Additionally, small footprint of the antenna elements in millimeter wave range allows to have many antenna elements in the receiver array. For these reasons, the ESPRIT algorithm is selected for this project.

Only two super-resolution algorithms are discussed in this sections. Additional techniques such as Pencil Matrix, Maximum Likelihood, weighted subspace fitting, improved versions of MUSIC and ESPRIT can also be analyzed. However, as most of the super-resolution algorithms share the same key features, the proposed system architecture is expected to be similar for the other algorithms.

3.3 Simulations with ESPRIT Algorithm

In order to propose a system, different aspects of the ESPRIT algorithm are analyzed by setting up a MATLAB simulation. This simulation assumes a continuous wave signal reflected from targets. The targets' RCSs are defined by a Weibull distribution, as predicted by automotive RCS modelling presented in the literature review. The signal received by the N element array (X_r), shown in Fiugre 3.1, can be mathematically represented by using a uniform linear array factor (AF) as described below.

$$AF = \left[1, e^{-j\omega\frac{dsin\theta}{c}}, e^{-j\omega\frac{2dsin\theta}{c}}, ... \ e^{-j\omega\frac{(N-1)dsin\theta}{c}}\right] \tag{3.1}$$

$$X_r = AF(\theta)s(t) + n \tag{3.2}$$

where $s(t)$ is the signal reflected by the targets, satisfying Weibull distribution and n is gaussian noise. The correlation matrix R and the signal received by the two arrays (shown in Figure 3.1) are given by following equations:

$$R = X_r(X_r)^t \tag{3.3}$$

$$R_{Array1} = \zeta R_{Array2} \tag{3.4}$$

where $(X_r)^t$ is transpose of X_r and ζ is related to the DoA information by the following expression.

$$\zeta = exp\left(j2\pi\frac{f}{c}dsin\theta\right) \tag{3.5}$$

The MATLAB implementation of the ESPRIT algorithm, presented in the appendix, uses eigenmode decomposition of noise corrupted correlation matrix to estimate the signal subspace from the noise subspace and solves linear system of Equation 3.4 to estimate target DoAs (ζ).

This simulation perceives the algorithm behavior with change in reflected signal SNR, number of targets and receiver antenna array size to propose a system utilizing ESPRIT algorithm for automotive radar applications. The simulation is run by one thousand times and the deviation of the estimated DoA from the actual ones is recorded for each iteration. The

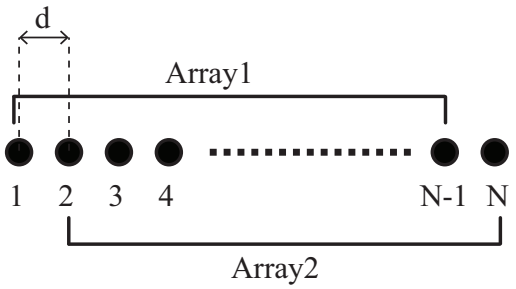

Figure 3.1 Uniform linear array configuration for ESPRIT algorithm.

number of iterations with error of a certain degree is denoted as the error count for that angle. The DoA error distribution (the error count vs degrees) are reported in the following graphs. Error distributions with concentration closer to zero degree are desirable. Five snapshots of the received data are used in this simulation to generate a correlation matrix. The target in these simulations is mid-sized vehicle modeled by Weibull distribution with shape and scale factors of 0.8 and 20, respectively. Uniform linear array with inter-element spacing of half-wavelength is considered at the receiver.

Firstly, the effect of SNR is observed by changing the SNR of the reflected signal. Two targets are placed at an angular displacement of 10^{o}. The receiver array has 20 elements in this simulation. The simulation results in Figure 3.2 show that with decrease in the SNR, the DoA error distribution spreads out. Thus, high SNR of the signal reflected from the targets is desirable.

Similarly, as shown in Figure 3.3, the DoA error distribution spreads with increase in number of targets, placed at 5^{o} angular displacements and average SNR for the reflected signal of approximately 10 dB. The receive array has 20 elements for this simulations. Finally, the error increases with decrease in the number of the receiver antenna elements as shown in Figure 3.4 for three similar targets placed with 5^{o} angular displacements with average SNR of approximately 10 dB.

Generally, super-resolution algorithms are sensitive to SNR and they are formulated for point targets. These factors pose serious challenges in utilizing these algorithms in automotive radar applications because the automotive targets are very complex in nature. Due to short distance, automotive targets act as extended targets [42]. An extended target has multiple scatterer on its surface. Hence one target reflects multiple signals depending on its structure. The strength of the reflected signal depends on the orientation of the target. Due to limited number of antenna elements in an array, it is possible that one target reflects multiple strong

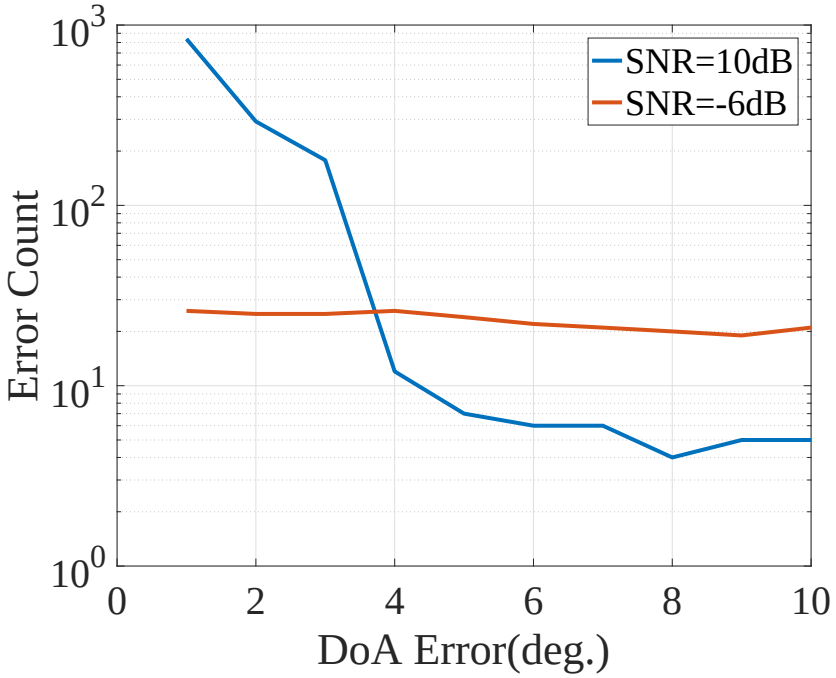

Figure 3.2 ESPRIT algorithm error distribution with respect to SNR.

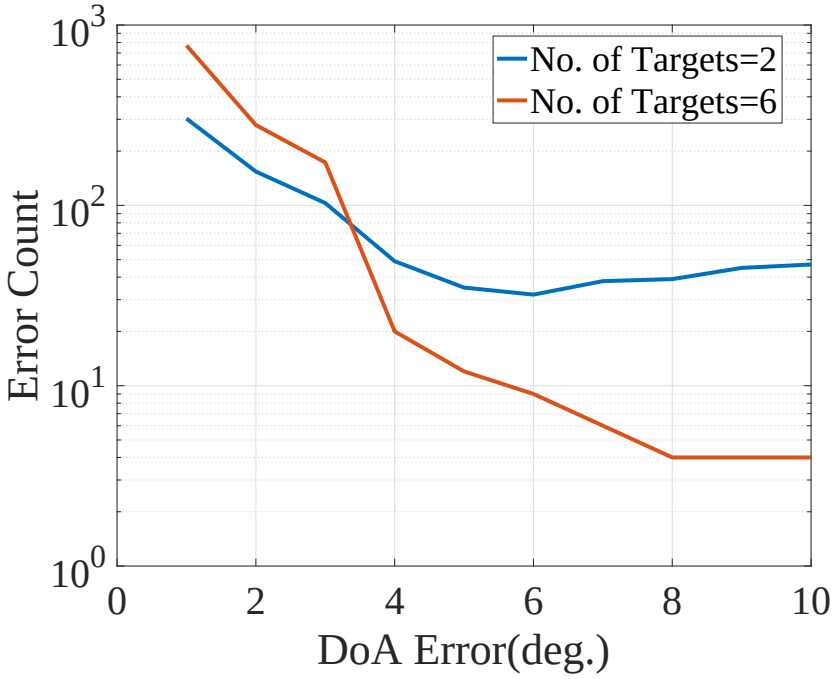

Figure 3.3 ESPRIT algorithm error distribution with respect to number of targets.

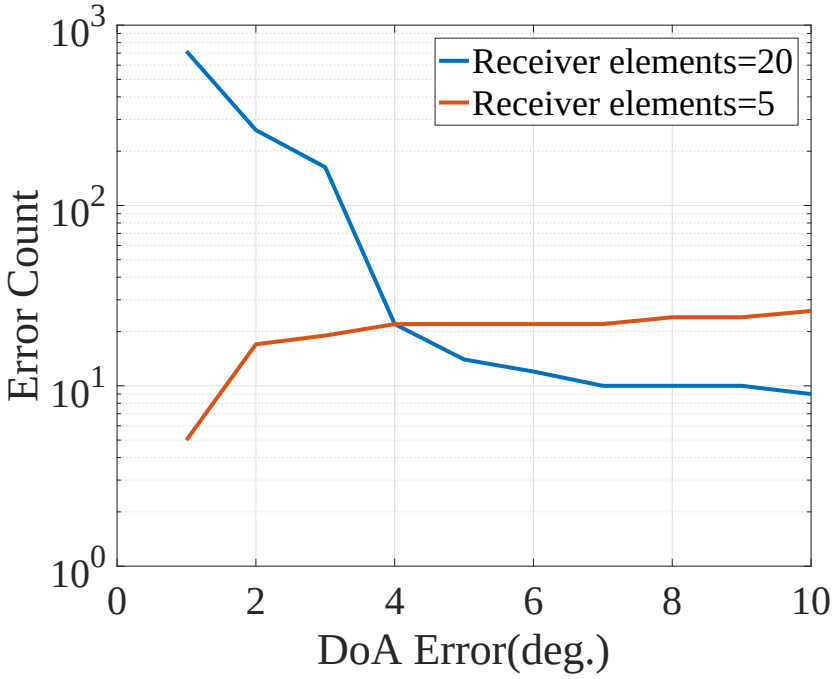

Figure 3.4 ESPRIT algorithm error distribution with respect to number of receiver antenna elements.

signals in comparison to the other targets of interest. In this case only strong signals will be detected by the algorithm. Hence other targets of interest can be masked by multiple reflection from one target.

Moreover, as mentioned in the literature review, the RCS of automotive targets is a strong function of aspect angle. This means that with a few degree of azimuth variation, RCS can vary by several dBsm. Additionally, visible FoV of automotive target is approximately 50° when it is illuminated from the rear side of the vehicle [42], [43]. This is why, using super-resolution algorithms, it is very challenging to position a target in 120° azimuth FoV required for the automotive radar (as mentioned in the literature review).

All these problems can be solved if we can make the automotive target radar friendly. In other words, if we can add a simple and low cost circuit (passive or semi-active) to the automotive target such that the target appears as a single reflector to the radar and is visible for whole 120° azimuth FoV, the problems associated with using super-resolution algorithms for automotive radar systems can be solved. This circuit or tag can introduce some simple modulations to separate desired targets from the background clutter and identify the targets. Reflection of the incident signal in the direction of incidence (retroreflection) is also proposed

for this tag to improve the tag RCS. In this work, polarization (90^o polarization rotation of the reflected signal with respect to the incident polarization) and amplitude modulations are proposed for this tag. In addition to the azimuth FoV, the tag should also provide 9^o elevation plane FoV to incorporate uneven terrain.

Finally, if we illuminate the whole 120^o FoV with one transmit antenna, then by using fully overlapping ESPRIT algorithm, we need N+2 receiver antennas, where N is the maximum number of detectable targets in the whole FoV. Moreover, from Figure 3.4, it is observed that longer receiving arrays reduce the error in DoA estimation. Combining these two factors, it is proposed to divide the whole 120^o FoV in smaller sections and illuminate each section with a signal that is modulated with a waveform that is orthogonal with respect to the waveforms of other sectors. Using this technique, we can detect a number of targets equal to the number of sectors times $N_r - 2$ for fully overlapping ESPRIT algorithm implementation where N_r is the number of antenna elements in the receiving array.

Based on this discussion, the proposed automotive radar system is shown in Figure 3.7. The transmitter subsystem divides the whole FoV into five sectors where each sector is illuminated by a signal that is modulated with a waveform orthogonal with respect to that of the other sectors. Though five sectors are suggested for the proposed system, system performance evaluation will determine the exact number of the sectors in the whole FoV. On the receiver side, each receiver antenna has a whole 120^o FoV. Though the receiver antennas share the whole FoV, orthogonal modulation of different sections allows us to distinguish the signals reflected from different sectors within the signal received by a single shared receiver. Hence the number of detectable targets can be increased by adding more sectors without changing the size of the receiver array.

The overall system is shown in Figures 3.5 and 3.6. The target is equipped with the proposed tag which is rotating the reflected signal polarization by 90^o with respect to the incident linear polarization. On the transceiver side, the transmitter sectors the whole FoV where each sector is illuminated by the modulation signal orthogonal to the other sectors. The elements in the receiver antenna array has FoV covering all the sectors. Statistical analysis of the signal received by the receiver antenna array reveals the DoA information of the targets in the radar FoV.

The development of the proposed radar system components can be divided into the following steps

1. Tag design
2. Design of the proposed transmitter antenna

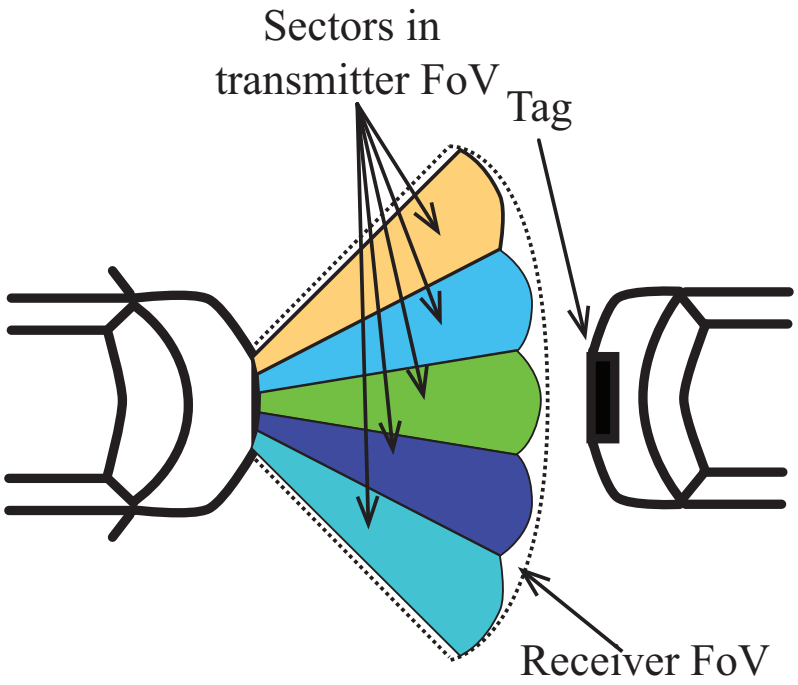

Figure 3.5 Automotive radar system description.

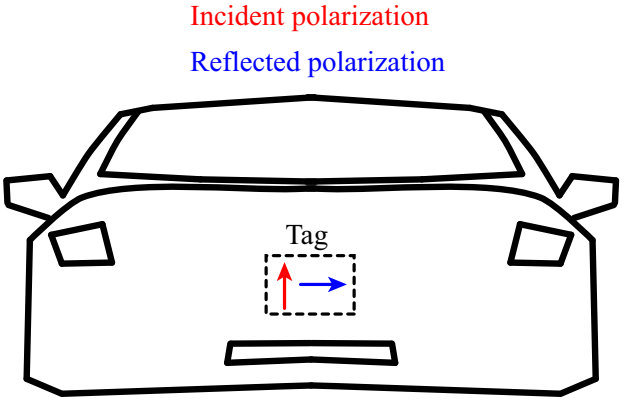

Figure 3.6 Tag on target vehicle

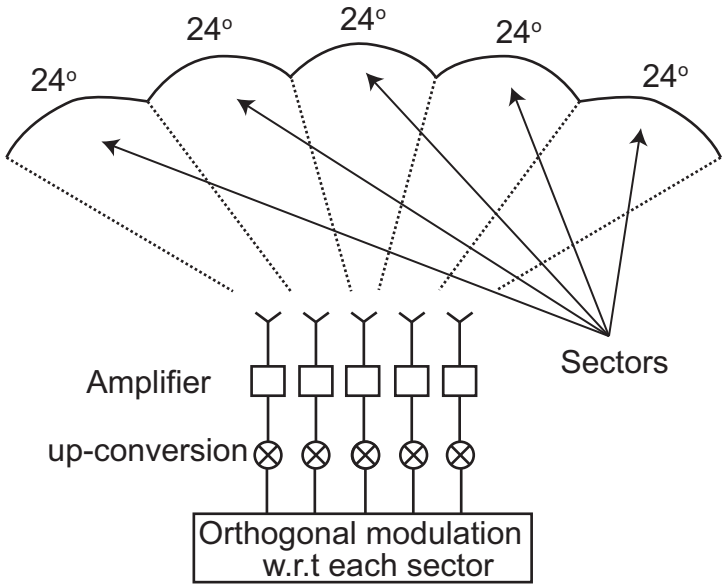

(a)

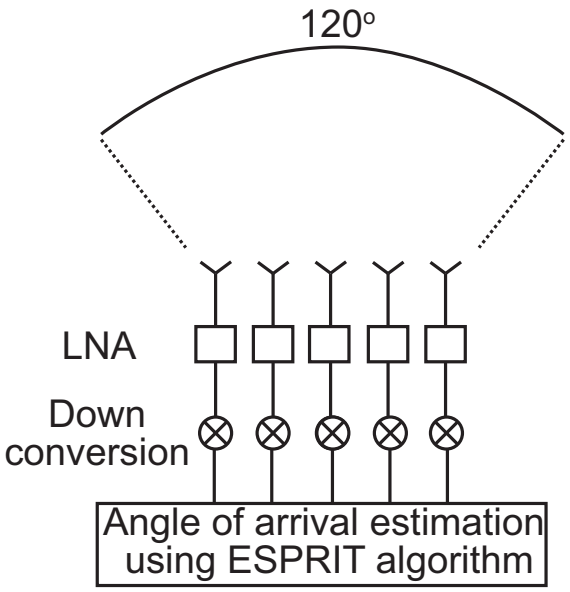

(b)

Figure 3.7 Proposed automotive radar System, (a) Transmitter (b) Receiver.

3. Design of receiver antenna system
4. Design of orthogonal waveforms for transmitter
5. Link budget analysis
6. Validation of the proposed system

This dissertation covers the challenging radiation sections of the proposed system which covers the tag and transmit antenna design.

3.4 Conclusion

A simple and possibly efficient system is proposed in this chapter. Based on the literature review in the last chapter, continuous-wave system mode and a DoA technique are selected. The ESPRIT algorithm is selected for the proposed application by considering the important features of well known super-resolution algorithms. A MATLAB simulation is used to analyze the performance of the ESPRIT algorithm for this particular application. Based on this analysis, a system is proposed for localization of automotive targets. The mm-wave components of this system will be proposed and presented in details in the following chapters of this dissertation.

CHAPTER 4 COMPACT W-BAND ANTENNA ARRAYS WITH POLARIZATION DESIGN FLEXIBILITY

As discussed in the previous chapter, a tag in W-band is proposed to improve the detection of targets in automotive radar applications. The tag is required to have 120^o and 9^o FoVs in azimuth and elevation planes, respectively. Moreover, radiating elements with orthogonal polarization are also required to implement polarization modulation in the tag to improve the target detection in the presence of the background clutter. A radiating structure is introduced in this chapter to implement such tag. This building block of the proposed tag should be able to provide two dimensional beamforming with compact azimuth size while providing polarization diversity. The compact azimuth size is required to ensure wide angle beam scanning without raising the grating lobes. One-dimensional arrays consisting of nine radiating elements (1×9) for two orthogonal polarization states are designed and prototyped in this chapter to cover the elevation FoV. These arrays are designed to have 0.47λ width in azimuth plane at 77 GHz. Two-dimensional arrays (6×9) for two orthogonal polarizations are then designed using these one-dimensional arrays with beamforming capacity in a 120^o range in the azimuth plane.

The radiating element structure and characteristics are briefly introduced in Section 4.1 along with a comparison of the proposed structure with other designs presented in the literature. Detailed discussions and design procedure of the proposed structures are presented in Section 4.2. The simulation and measurement results are reported in Section 4.3 and final remarks are made in Section 4.4.

4.1 Introduction

Designing a compact sized radiating element with polarization flexibility is challenging as both properties impose conflicting requirements. An efficient radiating element is usually about half-wavelength long. Though the polarization state can be varied by changing the orientation of a radiating elements, tightly packing the array for an arbitrary polarization is quite challenging.

As the tag is intended to operate in millimeter wave range, slots are selected as the radiating elements. In this frequency range, slots have several advantages. In addition to ease in fabrication, they can provide a compact footprint by capacitive loading at the ends as discussed in the following sections. They also provide high cross-polarization isolation [44]. Slotted

rectangular waveguides are known since long [45], [46]. The slot orientation on a waveguide determines the input impedance of the array. For the special case when a slot on the waveguide broad wall is placed parallel to the waveguide axis, the input impedance depends only on the displacement of the slot with respect to the waveguide axis [47]. The independence of the input impedance from the slot orientation for slot placed parallel to the waveguide axis allows us to match the array impedance with the transmission line characteristic impedance without changing the polarization state of the slot. However, for other polarization states, achieved by changing the slot orientation, the input impedance is a strong function of the slot orientation [48], making the impedance matching a challenging task for an arbitrary polarization array.

The proposed solution achieves the compact size with polarization diversity by introducing cavities between the feeding waveguide and radiating slots. With this configuration, the line loading is made independent of the orientation of the radiating slot, solving the problem of the input impedance dependence on the slot orientation for the classical slot array structure.

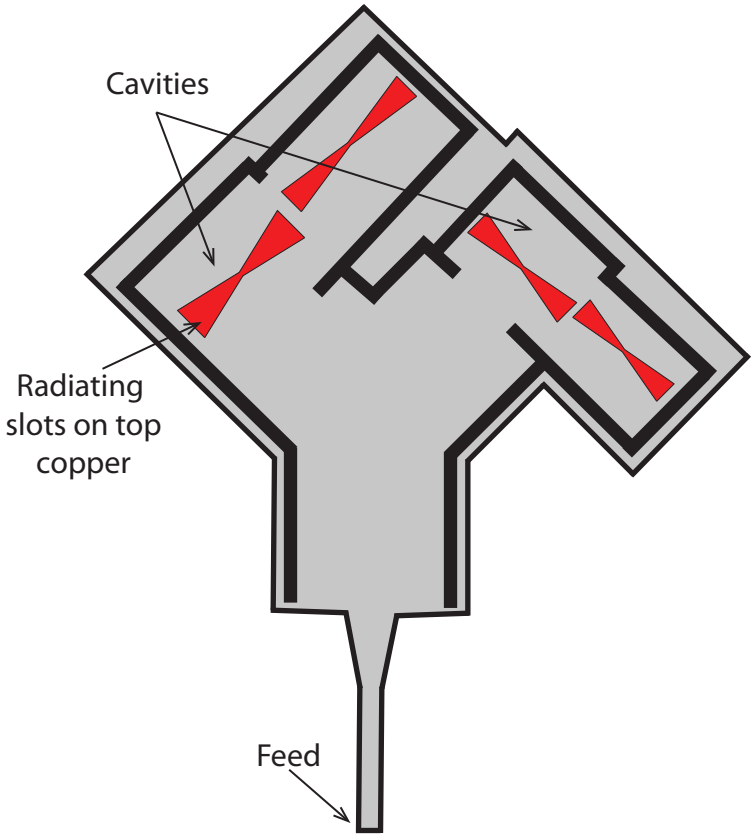

Figure 4.1 Top view of the SIW dual band slot antenna [49]

Cavity backed radiating slots have been reported in the literature. Size and orientation of a

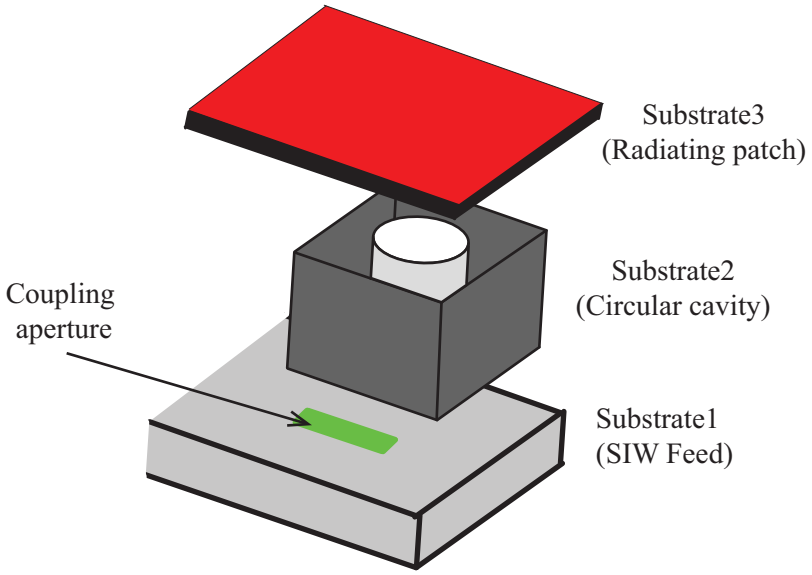

Figure 4.2 Geometry of the proposed SIW antenna array[53].

cavity backed slot are used in [49] to realize dual-band dual-polarization radiators as shown in Figure 4.1. However, as single radiator consists of multiple cavities, the large radiator size limits the array forming capacity. Another technique to implement a polarization diverse array is to use a cavity operating in some higher order mode. In [50], a 2×2 polarization diverse array is realized by using a cavity operating in TM_{220} mode. Scaling this structure to different array sizes for a desired FoV can be challenging. A diode loaded C slot on a cavity resonating in TE_{120} mode is presented in [51]. Similarly, a rectangular slot in a TE_{120} mode cavity is short-circuited at different positions in [52] to vary the polarization state of the radiated signal.

In addition to the cavity backed slots, aperture coupled cavities are also reported in the literature. In [53], circular cavities are aperture coupled with SIW line as shown in Figure 4.2. These cavities excite an array of patch antennas to radiate linear polarization. Two-dimensional topology for similar configuration is also reported in [54]. Configuration of these structures forces higher inter-element spacing for one- or two-dimensional arrays, limiting the array steering angle due to grating lobes.

The radiating element proposed in this chapter consists of a cavity that operates in its fundamental mode (TE_{110}). Due to this mode, the size of the cavity is compact. This cavity excites a radiating slot that can be oriented in an arbitrary direction without significantly changing the input impedance. Hence, this radiating element is compact yet it can be designed for an arbitrary polarization. In an array configuration, this radiating element

can provide smaller inter-element distance, limiting grating lobes for wide beam steering. Moreover, one- and two-dimensional arrays can be realized to provide beamforming flexibility in the resultant array.

4.2 Antenna Configuration

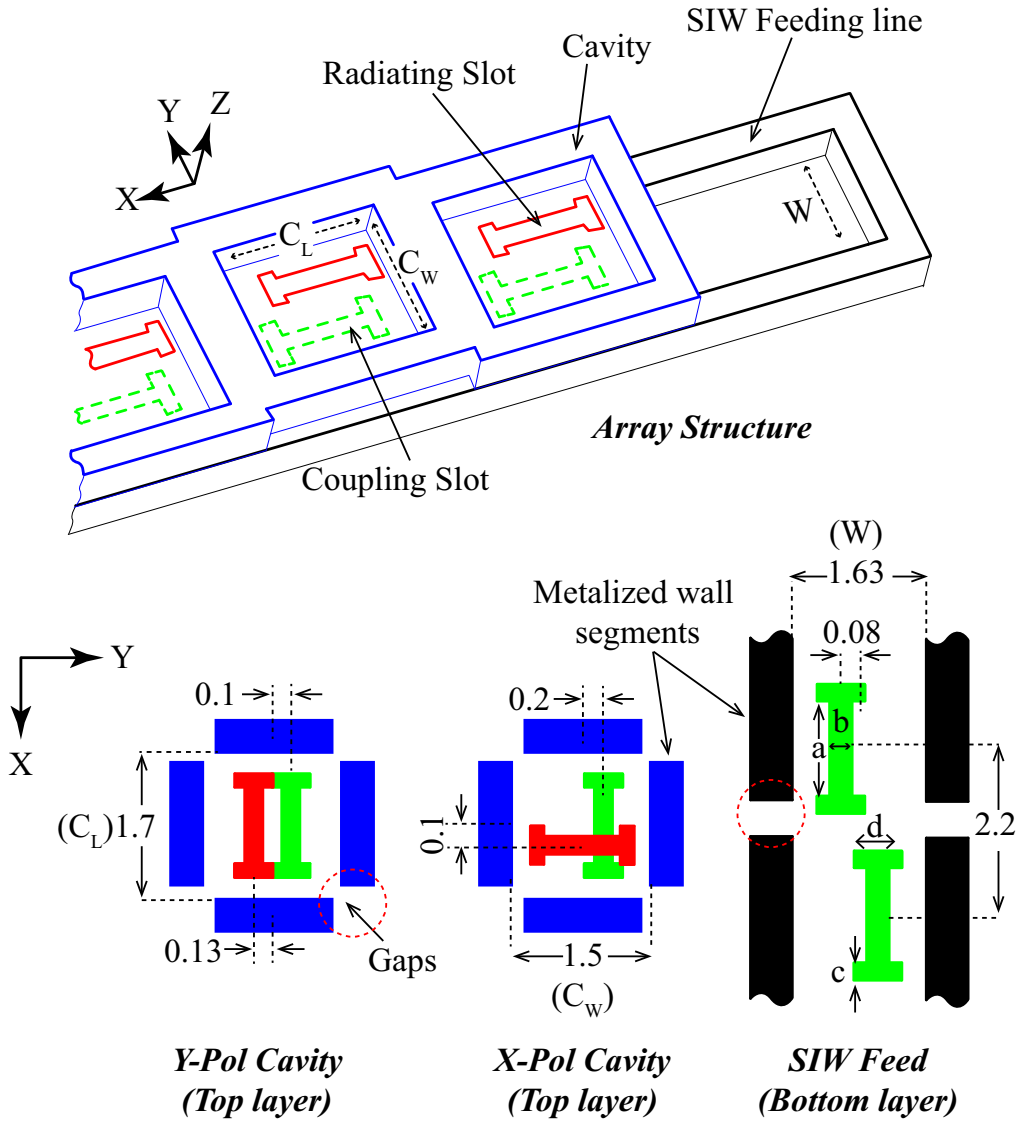

Figure 4.3 Antenna array structure (dimensions are in mm).

An illustration of a section of the proposed antenna array is shown on the top of Figure 4.3. It consists of radiating elements, series fed by a short-circuited SIW line. This structure consists of two layers. The feeding SIW and cavities are supported by the bottom and top layers, respectively. The polarizations are defined according to the coordinate system presented

in this figure. The rectangular cavities are designed to operate in their fundamental mode (TE_{110}). These cavities are excited by a coupling slot (green) between the SIW and the cavities. The cavities excite the radiating slots (red). The coupling apertures load the SIW as shunt impedances irrespective to the orientation of the radiating slots at the top of the cavities. Hence, the same input impedance can be achieved for arbitrarily polarized radiating slots.

The fundamental mode of the cavity is related to the cavity dimensions by the following equation:

$$f_{110} = \frac{c}{2\pi\sqrt{\mu_r \epsilon_r}} \sqrt{\left(\frac{\pi}{C_W}\right)^2 + \left(\frac{\pi}{C_L}\right)^2} \tag{4.1}$$

The inter-element spacing between the radiating elements mainly depends on the dimensions of the cavity. For a given inter-element distance, these dimensions can be designed by exploiting the above equation along with the proper selection of dielectric constant of the substrate used in the implementation of the antenna structure. The coupling and radiating slots' dimensions can be controlled by capacitively loading the slot ends, resulting in the dogbone shaped slots as shown in the Figure 4.3. For the two polarizations realized in this dissertation, cavity dimensions (C_W and C_L) are the same.

The positions of the coupling and radiating slots are determined by the current distributions on the cavities and SIW. The coupling slots are required to be alternating with respect to the SIW axis for in-phase excitation of the cavities as shown in [47], resulting in the cavity positions shown in Figure 4.3. The coupling and radiating slots are also placed with a slight offset with respect to the center of the cavity for proper excitation and radiation. This offset determines the excitation level and impedance of the radiator [46]. All the series fed radiating elements are uniformly excited in the proposed arrays. The optimized structure dimensions and relative positions are given in Table 4.1 and Figure 4.3.

For series feed, the cavities are placed half SIW wavelength apart. The SIW wavelength is determined by the width (W) of the SIW. Therefore, the cavity inter-element spacing is determined by the SIW width that can be varied to achieve the desired spacing. This control

Table 4.1 Slot dimensions(in mm) (Slot type and polarization are given in Figure 4.3)

Slot,Polarization	a	b	c	d
Coupling, X-pol	0.86	0.15	0.15	0.41
Coupling, Y-pol	0.84	0.15	0.15	0.46
Radiating, X-pol	0.63	0.2	0.18	0.51
Radiating, Y-pol	0.84	0.2	0.15	0.36

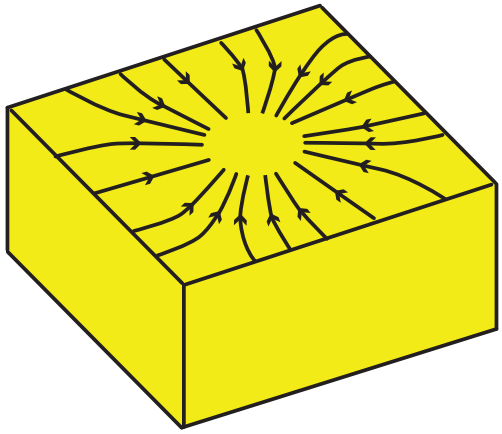

Figure 4.4 Current distribution on top cavity wall for TE_{110} mode.

on the inter-element spacing is an advantage of SIW as feed line. Hence, flexibility of selection of W and substrate dielectric constant, along with cavity dimensions related with one another by the fundamental mode equation, allow us to design the proposed one-dimensional arrays with desired inter-element spacing.

The current distribution on the top cavity wall in its fundamental mode is shown in Figure 4.4. The radiating slots can be coupled with this distribution in an arbitrary orientation. Hence, this structure can be designed to have an arbitrary polarization.

Although the proposed structure is compact and can be designed for an arbitrary polarization, this structure is inherently narrowband due to its small size and the resonant nature of the cavity. The material characteristics and fabrication tolerances make it challenging to achieve a precise bandwidth particularly in W-band. Hence, a good understanding of the material characteristics in the band of interest and the fabrication tolerances is required to achieve a precise bandwidth in millimeter-wave frequency range.

4.2.1 Prototype Fabrication

The cavities and SIW are realized using plated slots inside the substrate. The slots are created using laser machining followed by electroplating the slot walls. In order to preserve the overall mechanical integrity of the structure, small openings (red dotted circles in Figures 4.3 and 4.6) are introduced in the metallic walls of cavities and SIW. As these openings may result in the field leakage, the structures were optimized for maximum efficiency.

There are certain tolerances associated with the fabrication process used to realize the antenna prototypes. Firstly, as the laser burns through the substrate, the fabricated cavities and SIW have slightly different dimensions resulting in some fabrication tolerances. Additionally,

the coupling and radiating slots are realized by chemically etching the copper cladding of the substrate treated with photosensitive masks. These masks are manually aligned under a microscope. This type of alignment results in positioning tolerances of several microns. All these fabrication tolerances cause deviation of the measured results from the simulations.

The two layers (top layer containing cavities and bottom SIW layer) are fabricated separately and are assembled together with an inbetween adhesive layer of about 5 microns. This adhesive layer is a dielectric with $\epsilon_r = 3.5$. This layer was also included in the simulations to accurately predict the structure response.

Rt/Duroid 6002 from Rogers Corporation is the substrate selected for the realization of the proposed antenna structure. The material characteristics, given in the manufacturer's datasheet, are measured at 10 GHz. While working in W-band, a deviation of the dielectric constant and tangent loss of this material is expected. In order to estimate the dielectric constant, an SIW cavity was fabricated and its measured resonance frequency was compared with the simulated one. A reduction of 7% of the dielectric constant of the material was required to have a match between the measured and simulated resonance frequencies. This lower dielectric constant is expected to cause an upshift in the operating band of the fabricated prototypes. Similarly, the loss of the material in the band of interest was estimated by measuring the transmission coefficient magnitude of a straight SIW segment. In the measurements, transmission coefficient of a 4 cm long straight SIW was about -3.6 dB as compared to -1.5 dB in the simulation. Hence, it is estimated that the actual dielectric is about 0.52 dB/cm lossier than the simulation models for a straight SIW based on the 10 GHz loss tangent. This finding is also reported in [44]. This high loss is expected to lower the measured gains for one- and two-dimensional array prototypes fabricated to demonstrate the validity of the proposed design.

In order to validate the proposed radiator, one- and two-dimensional arrays with X- and Y-polarizations were designed and prototyped. The array configurations are illustrated in Figure 4.5. One-dimensional arrays have nine elements to achieve HPBW of 9° in the elevation FoV of the proposed tag. The inter-element spacing of these one-dimensional array elements is 2.2 mm which is $0.43\lambda_g$ (wavelength inside SIW) at the design frequency of 77 GHz. The feed line of the resonant array is terminated with a short-circuit that results in a resonant array with broadside beam. The width of this one-dimension array is 1.85 mm (0.47λ at 77 GHz). This one-dimensional array is arranged in alternating configuration as shown in Figure 4.5 to realize compactly packed two-dimensional arrays. As the width of the one-dimensional array is small, this two-dimensional array is expected to support wide angle beam tilt from the broadside in the yz plane without exhibiting grating lobes.

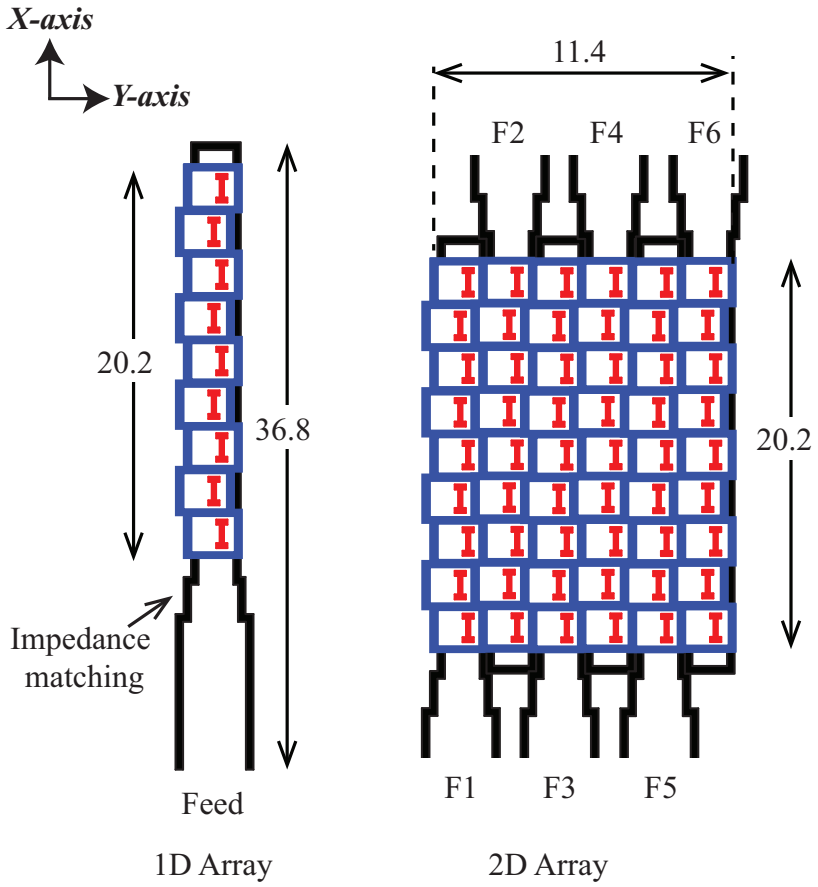

Figure 4.5 Description of one- and two-dimensional (Y-pol) arrays (units in mm).

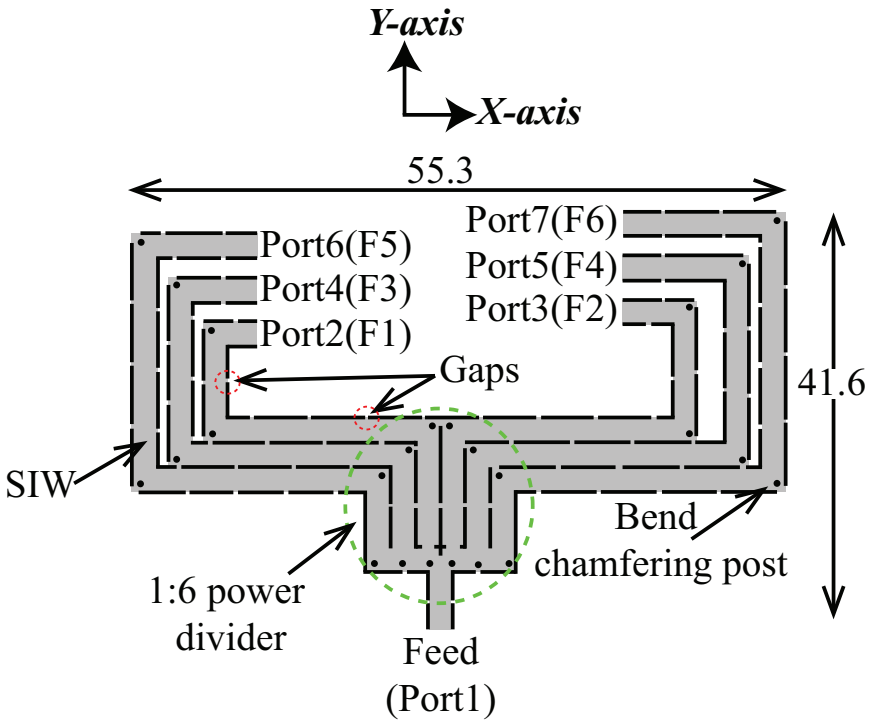

Figure 4.6 Description of feed network for two-dimensional arrays (units in mm).

A beam forming network (BFN) is designed to validate the wide angle beamforming characteristic of the proposed two-dimensional arrays. The BFN structure is shown in Figure 4.6. The port numbers of the BFN are consistent with the two-dimensional array illustration in Figure 4.5. The BFN consists of a 1:6 equal power divider [55]. The progressive phase delay, needed to tilt a beam at a fixed angle for phased arrays, is achieved by different length SIWs, adjusting the phase at the output of the power divider. Ansys-HFSS was used to design and optimize the fabricated arrays.

4.3 Results and Discussions

4.3.1 One-Dimensional arrays

The fabricated one- and two-dimensional arrays for two orthogonal polarizations (X-pol and Y-pol) are shown in Figure 4.7. One-dimensional arrays of X- and Y-pol are shown in Figure 4.7(a) and (b) followed by two-dimensional arrays in (c) and (d), respectively. Figure 4.7(e) and (f) show fabricated feed networks for both polarizations, for one- and two-dimensional arrays, respectively. As the feed line is SIW, a transition is used to connect this feed to WR10 waveguide ports of the vector network analyzer (VNA) [56]. The VNA is cali-

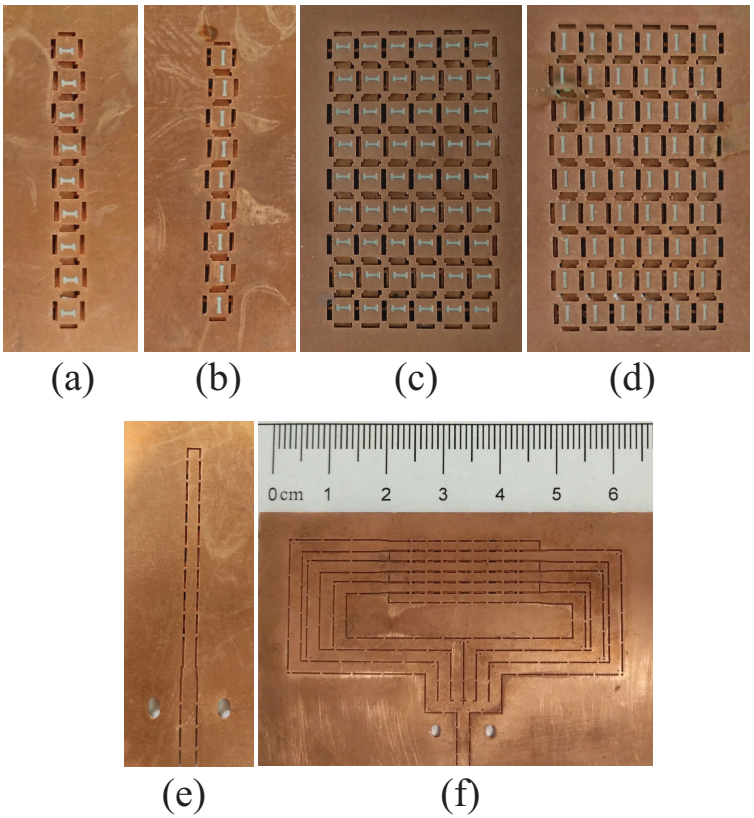

Figure 4.7 Fabricated prototypes, (a) 1D X-pol radiation slots, (b) 1D Y-pol radiation slots, (c) 2D X-pol radiation slots, (d) 1D Y-pol radiation slots, (e) 1D feed network for both polarizations, (f) 2D feed network for both polarizations.

brated with the reference planes at the SIW-WR10 transition input [44], hence the measured results do not de-embed the transition effects. That can also contribute to discrepancies in the measured results. Calibration to de-embed the transition requires same connection state for repeated measurements which is challenging to achieve due to the connection between the feeding SIW and the transition used for these measurement. A calibration was carried out using TRL kit is SIW technology, however, the VNA response for the calibration standards was not correct. Hence, TRL calibration in rectangular waveguide technology was used to get the antenna S parameters.

The S parameters of the X-pol one-dimensional array, shown in Figure 4.8, reveal a -10 dB bandwidths of 1.7 GHz (79.5 GHz - 81.2 GHz) and 3 GHz (79 GHz - 82 GHz) for simulation and measurement, respectively. Similarly, Y-pol one-dimensional array S parameters are shown in Figure 4.9, exhibiting -10 dB impedance bandwidths of 2.08 GHz (79.24 GHz - 81.32 GHz) and 3.2 GHz (78.8 GHz - 82 GHz) for simulations and measurements, respectively.

The X-pol radiation patterns of the one-dimensional array are shown in Figures 4.10 and

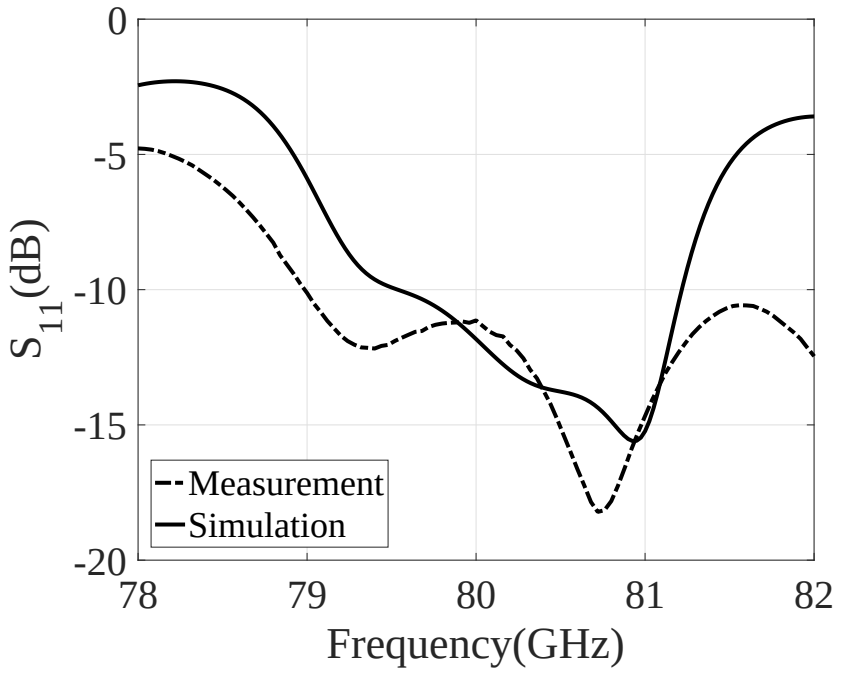

Figure 4.8 Simulated and measured reflection coefficient for X-pol.

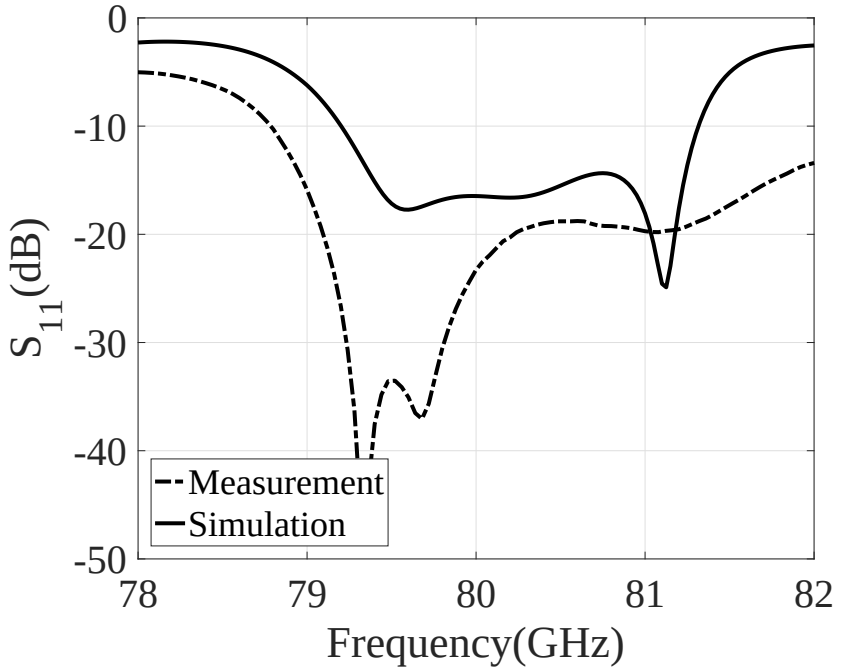

Figure 4.9 Simulated and measured reflection coefficient for Y-pol.

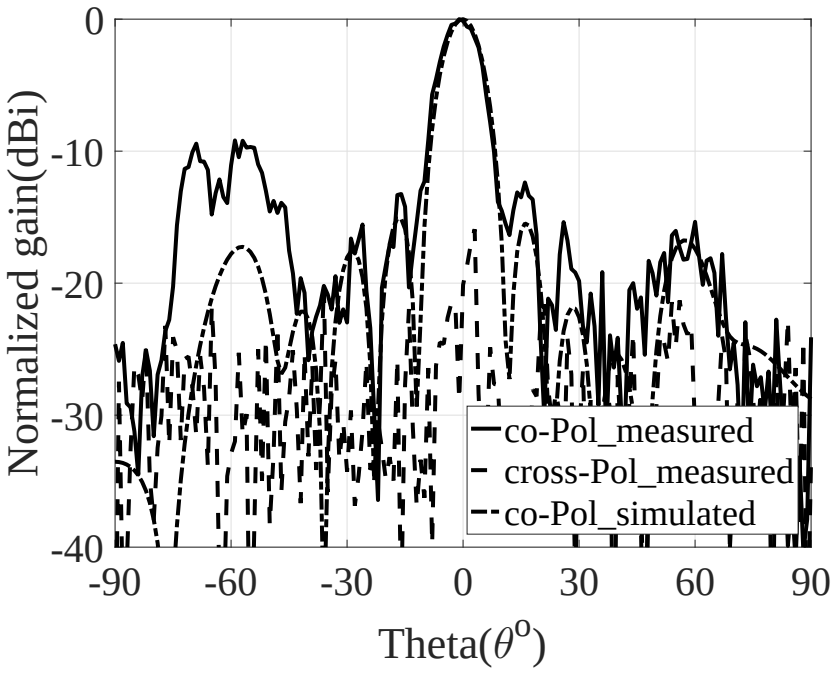

Figure 4.10 X-pol radiation patterns in xz-plane.

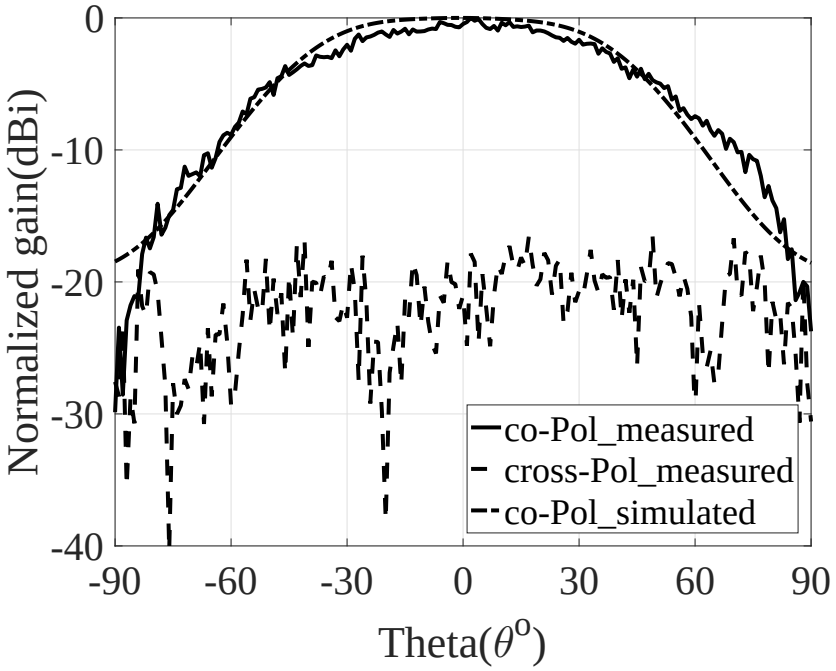

Figure 4.11 X-pol radiation patterns in yz-planes.

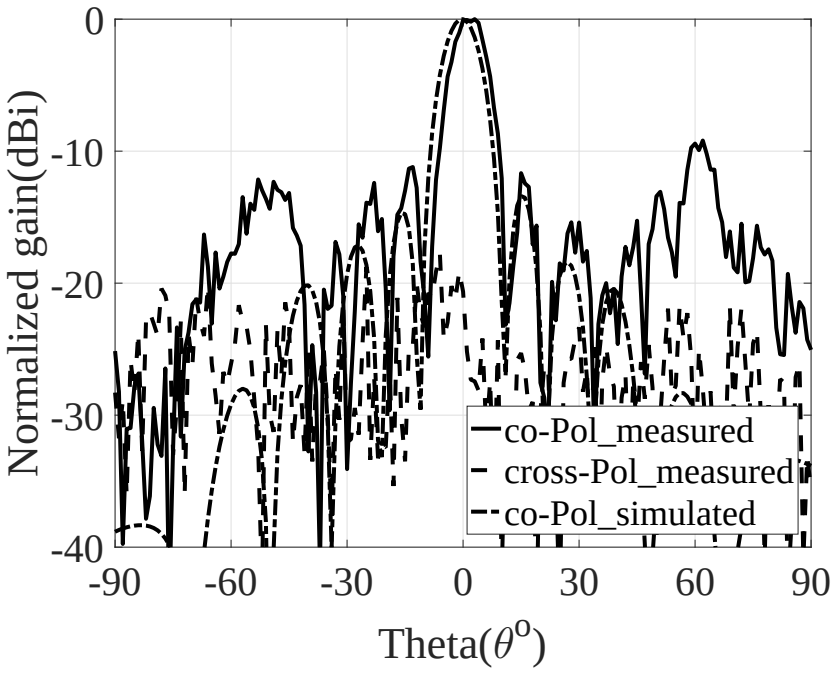

Figure 4.12 Y-pol simulated and measured radiation patterns in xz-plane.

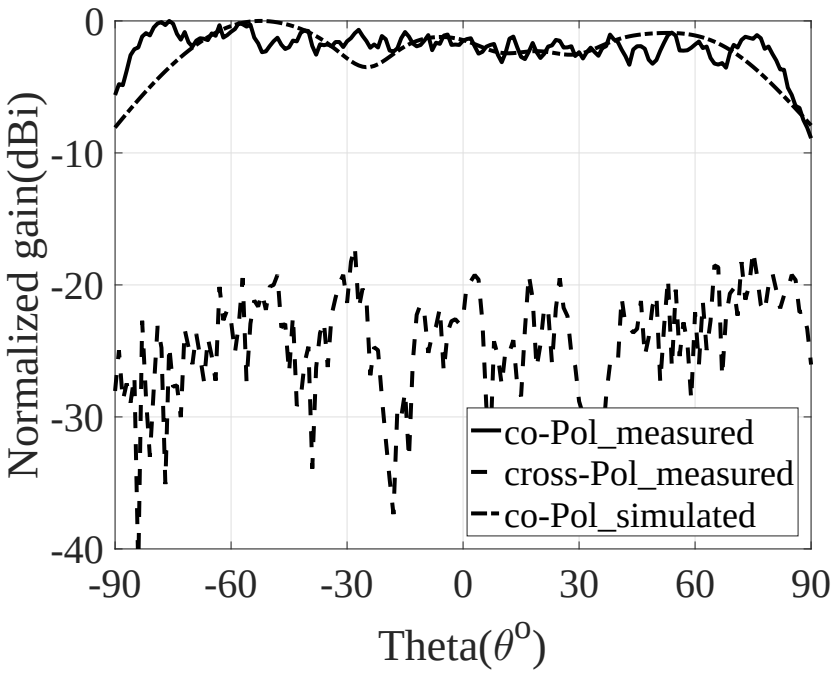

Figure 4.13 Y-pol simulated and measured radiation patterns in yz-plane.

4.11 for xz- and yz-planes (E and H planes, respectively) according the the coordinate system presented in Figure 4.3. For both polarizations (X- and Y-pol) and configurations (one- and two-dimensions), the radiation patterns are measured at 79.5 GHz. As the array axis is along X-axis, the xz-plane radiation pattern exhibits a narrow beam due to one-dimensional array. A measured half-power beamwidth (HPBW) of 10^o is observed in Figures 4.10. The radiation in yz-plane is due to the individual array element. As slot can be modeled as magnetic dipole, nulls at $\pm$90^o are thus expected in Figure 4.11 due to the X-pol slot orientation. The measured gain of this polarization is 9.8 dB which is 4 dB lower than the simulated one. This 4 dB loss is quite high, however, it is due to inaccurate loss tangent value in the simulation model. As the measured transmission coefficient of a straight SIW is 0.52 dB/cm lossier than the simulations, the 3.65 cm long feeding SIW for the two polarizations contributes about 2 dB loss. Additional loss is expected in the dielectric filled cavities. Accurate loss tangent value is required to update the simulation models for a better comparison between the simulated and measured results. Characterization of losses due to conductor and its roughness is also required to further improve the simulation model.

Similarly, for Y-pol, the radiation patterns in xz- and yz-planes (H and E planes) are shown in Figures 4.12 and 4.13, respectively. In the xz-plane, HPBW of 9^o is observed. The measured gain of 9.4 dB is 3 dB less than the simulated one. The yz-plane pattern is E-plane for the slot in this polarization. Theoretically, the slot should be omnidirectional in this plane. However, 3.3 dB ripples are observed due to diffraction through the edges of the finite 19×45 mm^2 sized ground plane.

A slight tilt of the main beam is observed in the xz-plane radiation pattern. It is due to the dielectric constant difference between the simulation model and actual substrate. Due to this difference, the actual wavelength in the feed line is slightly different, causing a small progressive phase error resulting in this beam tilt.

The radiation patterns in xz-plane show a side lobe level (SLL) of -12.3 dB and -11.2 dB for X-pol and Y-pol, respectively. As these one-dimensional linear arrays are designed to have uniform excitation, theoretically, SLL should be -13.5 dB. However, due to material characteristics variations, it is difficult to maintain uniform amplitude and phase distributions for series fed array elements.

For both principal planes, the cross-polarization isolation in measurements is approximately 20 dB for the two polarizations. This isolation is at least 5 dB poorer than the simulated values. This discrepancy is attributed to the measurement setup that has high noise floor. In this frequency band, the measurements in the anechoic chamber show average signal at this power level even without any antenna connected to the measurement port. Detecting

weak signals below the noise floor is quite challenging.

There are also some spikes observed in the measured radiation patterns in xz-plane. These spikes are caused by the SIW-WR10 transition. This cube shaped metallic transition [44] cause reflections at about -55^{o} and diffractions at about 60^{o}, raising spikes in the xz-plane measured radiation patterns. As this transition is not included in simulations, the spikes are absent in the simulated radiation patterns.

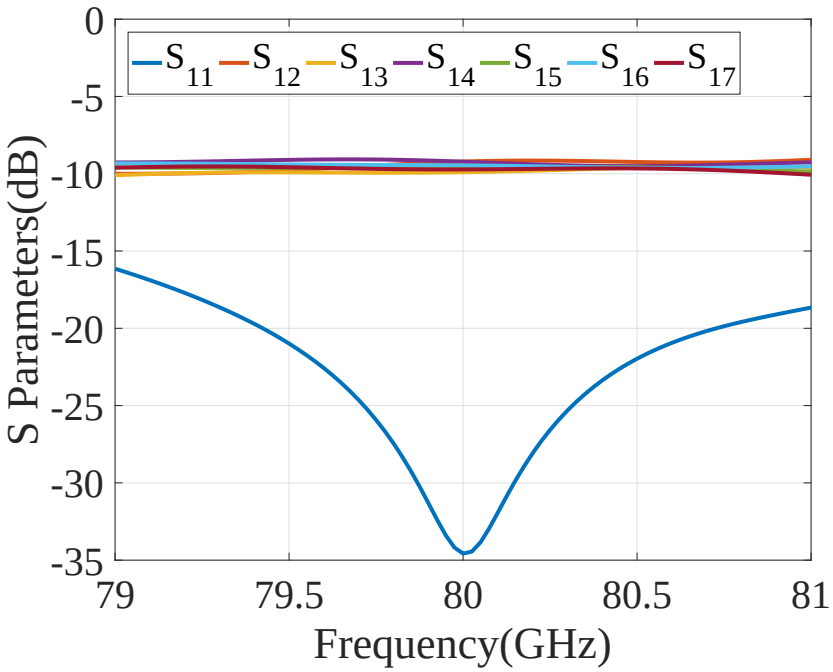

Figure 4.14 Simulated magnitude response of BFN.

4.3.2 Two-Dimensional arrays

The BFN is characterized in Figures 4.14 and 4.15. This network equally splits the input power into six output ports (Figure 4.14) and provide a progressive phase of 88^{o} to steer the broadside beam by 30^{o} for 1.85 mm inter-element spacing at 79.5 GHz by using different length SIWs. The material dielectric constant estimated for W-band is used for these simulations. However, the loss tangent of the material is different in practice and the magnitude response is expected to vary from the simulated one shown in Figure 4.14. The maximum difference of the feeding SIWs lengths is 2.3 cm causing estimated feed magnitude variation of about 1.2 dB (the measured transmission coefficient of a straight SIW is 0.52 dB/cm lossier as compare to the simulation). Array factor manipulation for six elements reveals that this

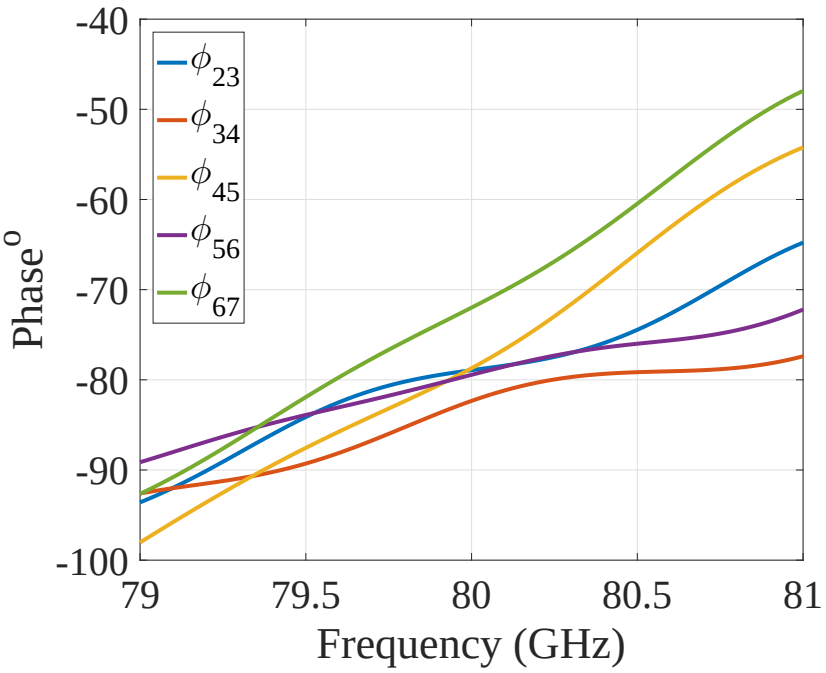

Figure 4.15 Simulated phase for adjacent feed BFN ports.

variation does not have significant affect of the HPBW and SLL of the phased array with 30° beam steering. There is also a phase error (a deviation of the phase between adjacent antenna ports from the desired progressive phase) of 6° as shown in Figure 4.15. However, eliminating this error requires fine adjustments in the SIW lengths that are quite challenging to realize.

The simulated radiation patterns for different beam tilts are shown in Figures 4.16 and 4.17 for X- and Y-pol two-dimensional arrays, respectively. The two-dimensional array configuration for Y-pol is shown in Figure 4.5 (right). The simulation models are excited by the ports on the opposite sides of the two-dimensional array axis and the beam is steered by changing the phase of the adjacent elements of the array. For the beam steering of 30°, the excitation magnitude and phase are the same as realized by the designed BFN. In case of Y-pol, a beam scan of 55° is achieved. However, for the X-pol, the beam scan is limited to 45° due to the element radiation pattern of this polarization shown in Figure 4.11. This element pattern imposes a null at ±90° in yz-plane, limiting the two-dimensional array FoV in this plane. It is important to mention that for two-dimensional arrays, the grating lobes are limited to less than -10 dB level for both polarizations. Hence, a wide angle beamforming for polarization diverse radiating element is achieved without raising the grating lobes. The beam scan loss is 4 dB and 0.5 dB for X- and Y-pol two-dimensional arrays, respectively. The high X-pol

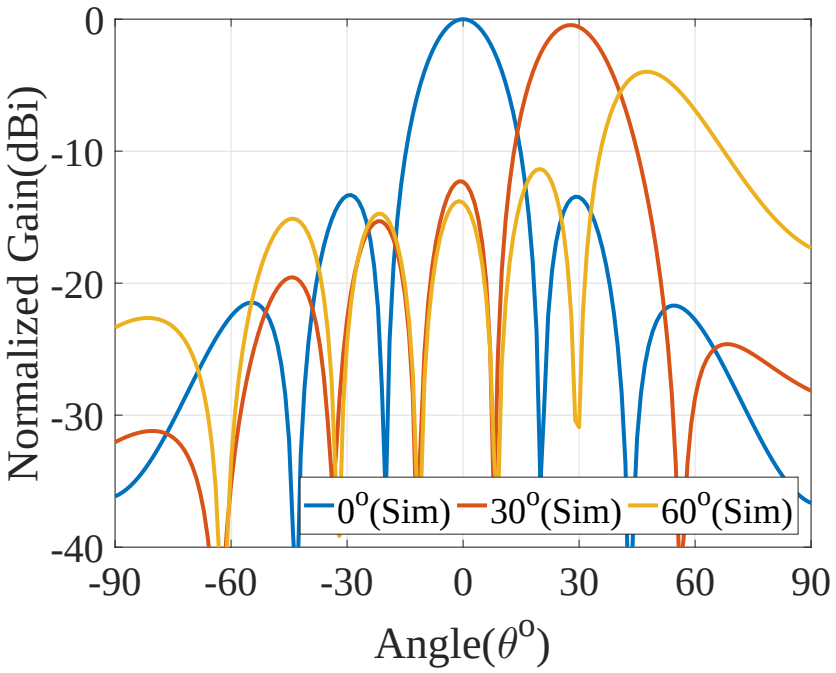

Figure 4.16 Simulated radiation patterns for two-dimensional X-pol array.

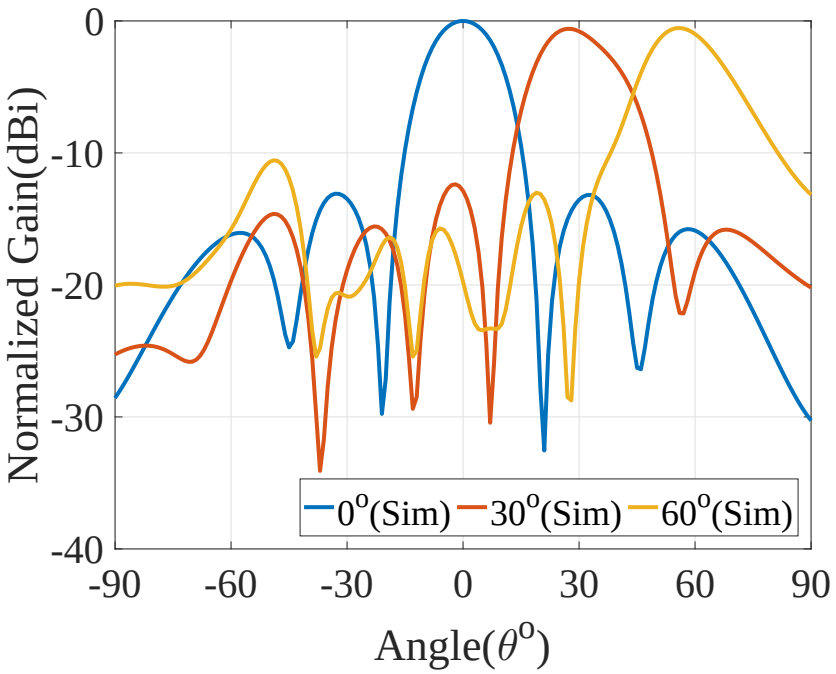

Figure 4.17 Simulated radiation patterns for two-dimensional Y-pol array.

scan loss can be attributed to the element factor as explained earlier.

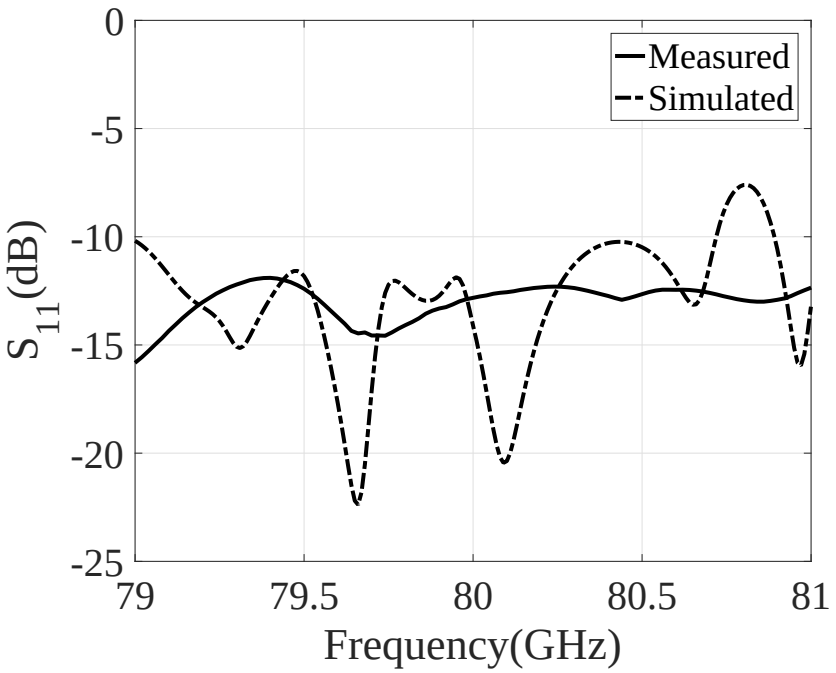

Figure 4.18 S parameters for two-dimensional X-pol array with fixed beams steered at 30 degrees in the yz-plane.

Two two-dimensional arrays were fabricated to validate the wide angle beamforming. The BFN steers the broadside beam at an angle of 30°. The measured and simulated S parameters for the two dimensional arrays are shown in Figures 4.18 and 4.19 for X- and Y-pol two dimensional arrays. The measured radiation patterns are shown in Figures 4.20 and 4.21, for X- and Y-pol arrays, respectively. The main beam steering angle and the SLL closely agree with the simulation results, hence, validating the proposed radiating element wide angle characteristics.

4.4 Conclusions

A compact radiating element is proposed in this chapter. It consists of a radiating slot on a rectangular cavity which is operating in its fundamental mode. This cavity is excited using a slot, coupling it to an SIW passing below the cavity. The proposed radiating element can be designed for arbitrary polarization. Its compact size provides flexibility in two dimensional array forming. One- and two-dimensional arrays are designed and fabricated for two orthogonal polarizations using this radiating element. One-dimensional arrays (1×9) provide 2.5%

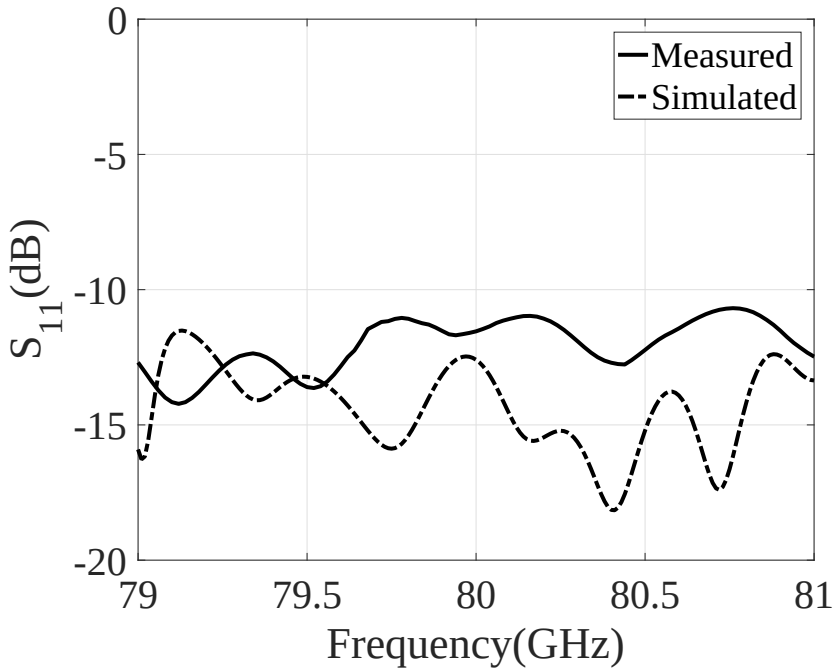

Figure 4.19 S parameters for two-dimensional Y-pol array with fixed beams steered at 30 degrees in the yz-plane.

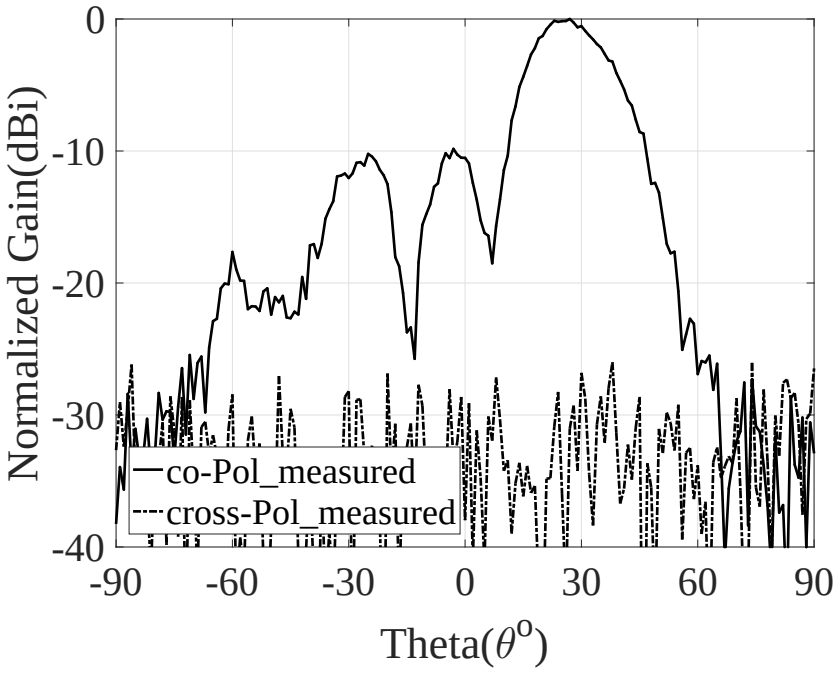

Figure 4.20 X-pol Measured radiation patterns for two-dimensional array with 30° tilt angle.

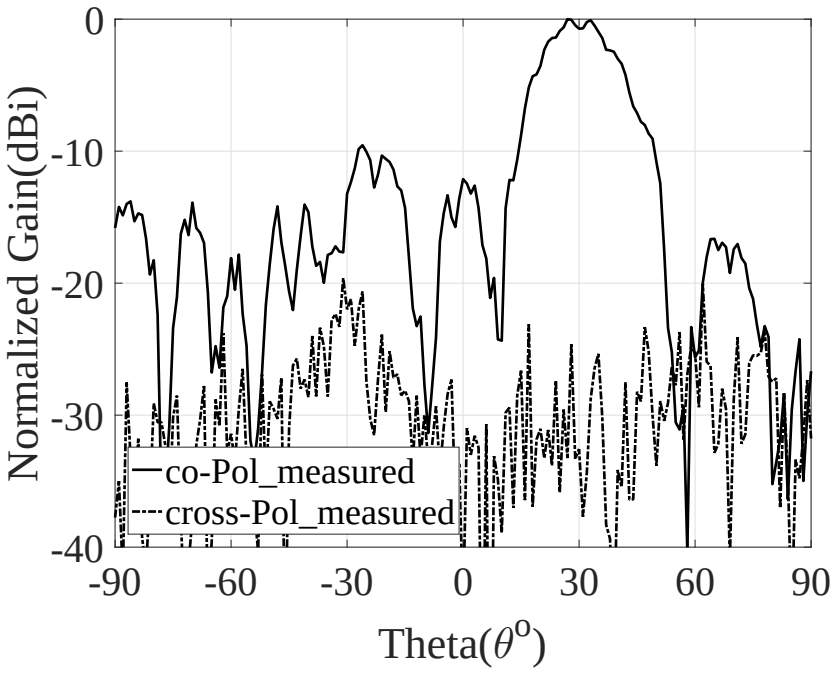

Figure 4.21 Y-pol Measured radiation patterns for two-dimensional array with 30º tilt angle.

impedance bandwidth in W-band. Their radiation FoV has about 9º HPBW in plane parallel to the array axis and wide HPBW in the perpendicular principal plane. The worst case SLL is -11.2 dB. This one-dimensional array is used to create two-dimensional arrays (9×6). The width of one-dimensional arrays are designed to be 0.47λ at 77 GHz to achieve wide angle beam forming capacity (120º for Y-pol and 90º for X-pol) while limiting the grating lobes under -10 dB level relative to the main beam. A feeding network of this two-dimensional array is also designed and analyzed in this chapter. Good agreement between simulated and measured results validate the proposed design. Measured HPBW, side-lobe levels and beam steering angles closely match with the simulations. Generally, the radiation patterns should have better agreement with the simulation, however, structure complexity, fabrication tolerances and measurement setup caused discrepancies in the measured radiation patterns. Better characterization of the material in W-band is also required to update the simulation models to have an accurate comparison between the simulated and measured result.

CHAPTER 5 MODULATION SWITCH DESIGN

In addition to polarization modulation which improves the target visibility in highly cluttered environment, back scattering signal modulation by the tag can also enhance the system functionality. Amplitude modulation is suggested for the proposed tag. This modulation can not only communicate additional information between the tagged target and automotive radar but also improve the received signal SNR by using spread spectrum like techniques. A general rule of thumb is that an on/off amplitude modulated sequence of length N will provide a SNR boost of $10 * log10(N)$. This SNR boost can be seen as RCS boost for the proposed tag presented in the following chapter. That is, the target RCS will be boosted by $10 * log10(N)$.

In this chapter, a novel switch in SIW technology is proposed for this purpose. This switch utilizes a high impedance load on the transmission line which is switched by coupling the load with a diode. This load is realized by placing a resonant slot on an SIW line with the slot length perpendicular to the SIW axis. This slot is loaded with a PIN diode that can switch the slot impedance by applying forward or reverse DC-biasing.

A PIN diode is an essential component of the proposed switch. The proposed concept was validated in K-band. A switch was also implemented in W-band, by emulating an on-state PIN diode with a short-circuited slot at its center as discussed in Chapter 6, to incorporate amplitude modulation in the proposed tag.

The switch presented in this chapter is compared with different other switch topologies appearing in the literature in Section 5.1. The switch concept and design are presented in Section 5.2. The measured and simulated results are discussed in Section 5.3 followed by conclusions in Section 5.4.

5.1 Introduction

A switch is an essential component in various RF systems. Substrate integrated waveguide (SIW) is the preferred transmission line for high frequency RF circuitries due to its lower radiation losses. Several SIW switch topologies are reported in the literature, however, these topologies are not suited for the particular tag application.

In [57], vias are introduced inside an SIW operating from 8.24 GHz to 10.36 GHz. Annular slots are used in the top SIW wall to disconnect these vias from this wall. As these vias are not connected with the top wall of the SIW, they have minimum effect on the transmission

mode supported by the SIW, acting as on-state switch. However, the annular slots can be loaded with PIN diodes to connect these vias with the top wall. In case of forward biased diodes, these vias are connected with the SIW wall, behaving as shunt loads. These shunt loads reflect back the signal, causing minimum transmission. Hence, the switch is in off-state. This type of topology has a serious drawback as the operating frequency is shifted to higher frequencies. In millimeter wave frequency range, the SIW becomes narrower, rendering significant vias discontinuity in on-state switch. Hence, These vias cause low transmission and high reflection for on-state switch in millimeter wave frequency range.

In [58], an SIW operating in the range 9.5 GHz to 11 GHz is loaded with a patch of ferrite material on its top wall. This material changes its relative permeability with the application of external DC magnetic field. The SIW and the ferrite material are selected such that on the application of the external magnetic field, the SIW is switched to a cut-off state, resulting in an off-state switch. In the absence of the external magnetic field, the operating frequency is above the cut-off frequency, causing a high transmission. Similarly, in [59], side SIW walls are loaded with ferrite material that switches the SIW in cut-off state with the application of an external magnetic field.

In [60], a half-mode SIW switch is presented. A slot along the axis of a full-mode SIW is used to realize a half-mode SIW operating between 3 GHz and 4.7 GHz. The cut-off frequency of the full-mode SIW is higher than the operating band of the half-mode SIW. The slot that realizes the half-mode SIW is loaded with PIN diodes. For the reverse biased PIN diodes, the SIW operates in half-mode, resulting in on-state switch. When the diodes are forward biased, the half-mode SIW is switched to full-mode SIW which is designed to be in cut-off state, realizing an off-state switch. Similarly, in [61], two quarter wavelength open-circuited stubs are connected with half-mode SIW via PIN diodes. These stubs realize RF short-circuits on the half-mode SIW when diodes are forward biased, realizing the off-state switch.

All the SIW switch topologies discussed in the above paragraphs require vias inside SIW, external magnetic field or half-mode operation. A simple switch circuit can instead be proposed by realizing a switchable load on an SIW. Resonant slots on broad side wall of a rectangular waveguide, inclined with respect to the waveguide axis are well known to behave as a series load on that waveguide [62]. Hence, a slot on an SIW top or bottom wall can realize a simple series load on this transmission line. The slot impedance can be switched by loading this slot with a PIN diode [63]. This diode loaded slot can realize a switchable load on an SIW without the use of vias inside SIW, external magnetic field or half-mode operation. Additionally, this configuration facilitates the diode integration in SIW technology which usually requires

transitions from SIW to some other transmission line (microstrip line, coplanar waveguide etc.) [64]. These features are critical for switch design in the millimeter wave frequency range with strict space constraints and lossy substrates.

5.2 Switch Concept and Design

A slot on an SIW is shown in Figure 5.1(a). This slot can be modeled as a series load on a transmission line as shown in an equivalent circuit diagram in Figure 5.1(b). The series loading on the transmission line depends on the slot inclination angle θ, defined in this figure. This loading can be characterized by observing the reflection coefficients of the transmission line with different inclination angles. Such simulated reflection coefficients for an SIW are shown in Figure 5.2 for different values of θ. Ansys-HFSS was used to simulated an SIW of 5.08 mm width in 0.508 mm thick RT/Duroid 6002 substrate with $\epsilon_r = 2.94$. For the SIW mode (TE_{10}), the resonant slot length varies with change in the inclination angles. Different slot lengths, mentioned in this figure, were used to get simulation results where the same resonance frequency is achieved for all values of θ. A slot width of 0.33 mm was used in all these simulations. These graphs show that the slot impedance increases monotonically with increase in the inclination angle causing higher reflection coefficients [65]. The maximum loading is achieved by placing the slot perpendicular ($\theta = 90^o$) to the SIW axis. Moreover, the reflection coefficients are less than -1 dB for inclination angles greater than 45^o. Hence, a high isolation switch can be realized by placing a slot on an SIW with $45^o \leq \theta \leq 90^o$. Only the slot oriented at $\theta = 90^o$ is considered in this work.

A diode can be loaded on this slot to switch its impedance. Ideally, a diode can change its state from high to low impedance by applying appropriate DC-biasing. If such a diode is placed at the middle of the slot, a high impedance loading can be achieved by reverse biasing the diode. In forward biased diode case, the slot is short-circuited at its middle, eliminating the high impedance by shifting the slot resonance outside the band of interest.

A slot, being similar to a magnetic dipole, resonates when its length is somewhere between $\lambda/2$ and $\lambda_g/2$ where λ and λ_g are respectively the wavelengths in air and inside the SIW. When this slot is loaded with a practical diode with parasitic and reverse biased capacitances, the resonant slot length is expected to change. A proper understanding of these capacitances is required to design the switchable load in a band of interest. A full-wave simulation with the diode capacitance values available in its datasheet is essential to determine the slot length. The slot width depends on the physical length of the diode that is selected to be placed on the slot.

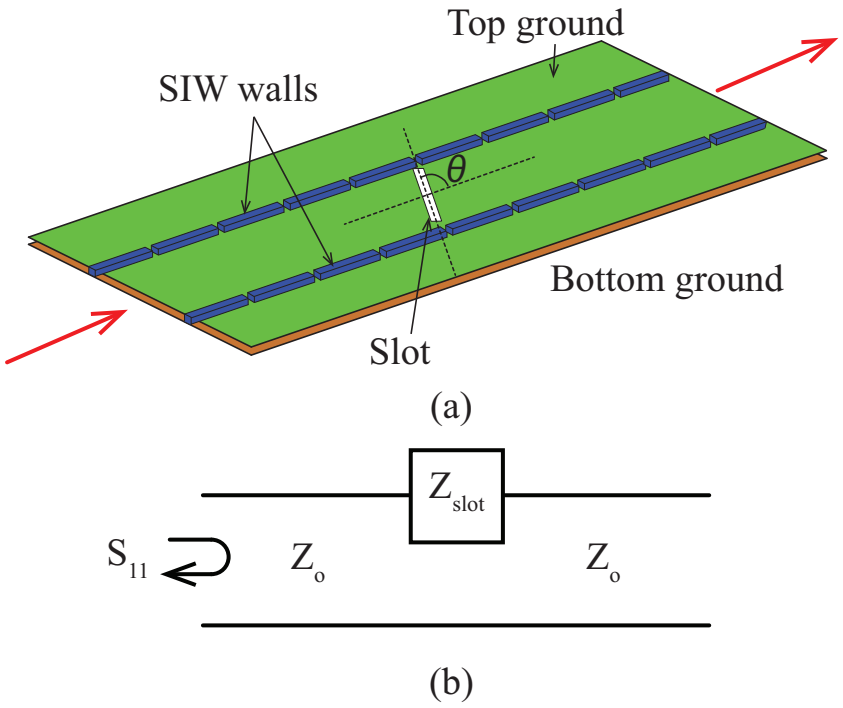

Figure 5.1 A slot on an SIW. (a) structure; (b) equivalent circuit model.

Open-circuit and short-circuit diode characteristics for forward and reverse biasing are necessary requirements for the proposed switch. A PIN diode with high reverse biased isolation and low forward biased insertion loss is ideal for this application. For a K-band switch implemented in this work to validate the proposed design, part MA4AGFCP910 from MACOM was used, as it provides the required characteristics for up to 50 GHz. The operating band of a diode is closely related to its parasitic capacitances. As the diode is placed on the slot in the proposed design, a high parasitic capacitance can bypass the high impedance of the slot, leaving the switch in on-state irrespective to the DC-biasing. In W-band, commercially available Schottky diode cannot be used for this application as it provides low off-state isolation and high junction capacitance which by pass the high impedance slot in off-state switch.

A diode loaded slot impedance on an SIW can be determined by using the simulated reflection coefficient [65]. According to the simulations, the unloaded slot on an SIW provides a series impedance of 23 times the SIW characteristic impedance. To characterize the effect of the diode on this slot, a lumped impedance of 0.02 pF was placed across the slot in its middle. The slot impedance dropped from 23 to 9 times the characteristic impedance of the SIW. This diode loaded slot was sufficient enough to provide more than 10 dB isolation for off-state switch within the band of interest. For the forward biased switch, the 0.02 pF capacitance was replaced with a 5 ohms resistance according to the manufacturer datasheet of the selected

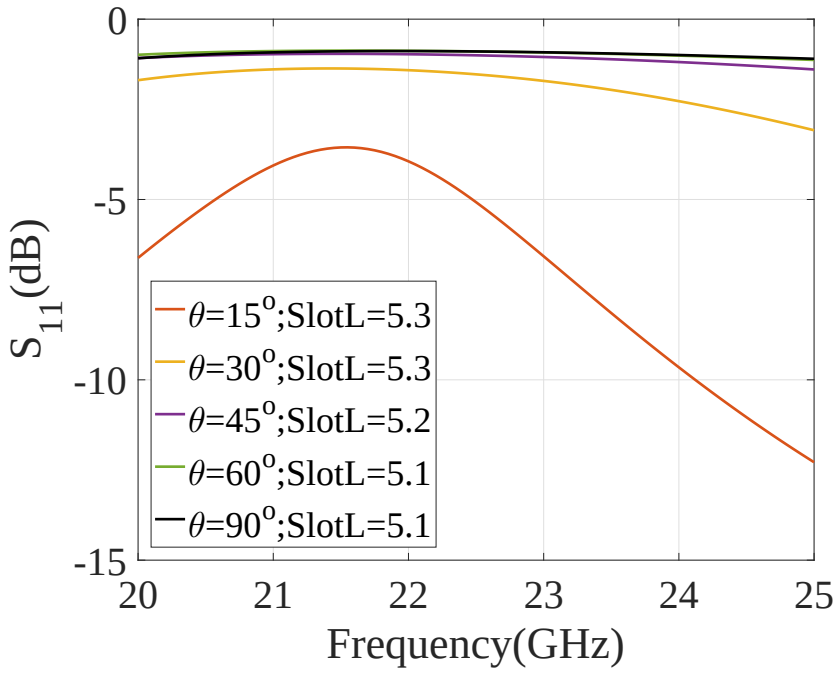

Figure 5.2 Reflection coefficient variation of a slot-loaded SIW with change in the slot inclination angle θ. The slot length (SlotL in mm) was adjust to have the same resonance frequency in all cases.

diode. The simulated reflection coefficients of a diode loaded slot with forward and reverse biased diode are shown in Figure. 5.3. Corresponding equivalent circuit models are also presented in this figure to understand the slot behavior for different biasing states. For the resonant diode loaded slot at 22 GHz, the optimized length is 3.94 mm, which is 1.16 mm less than the unloaded slot length due to diode parasitic capacitances.

5.3 Measurement and Simulation Results

The layout for the proposed switch structure is shown in Figure 5.4. Different dimensions mentioned in this figure are given in Table 5.1. In order to load the slot with a diode, DC isolation for the diode and RF isolation for the DC-biasing circuit are required. As the slot

Table 5.1 Structure dimensions

a	b	c	d	e	Slot Length	Slot Width	Stub Angle	Stub Radius
mm	mm	mm	mm	mm	mm	mm	deg	mm
5.08	2.03	1.27	1.75	1.9	3.94	0.33	70	1.14

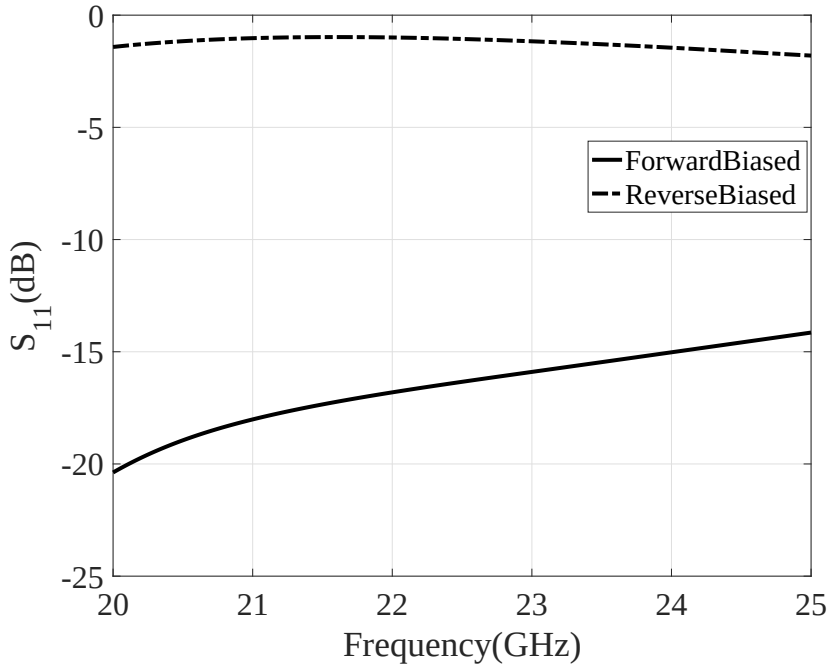

(a)

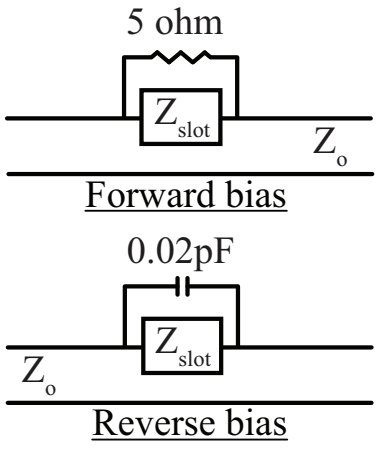

(b)

Figure 5.3 Reflection coefficient variations (a) and equivalent circuit models (b) of an SIW with diode-loaded slot.

is an aperture in a metal sheet, the anode and cathode of a diode directly placed on the slot would be electrically connected. Hence, a DC voltage cannot be applied to the diode. DC isolation of the diode is therefore required for proper switch operation. A thin laminate layer can be introduced to address this issue. Electrically disconnected anode and cathode pads can be introduced on this laminate to bias the diode. As the laminate is thin, the diode is still RF coupled with the slot to switch its impedance.

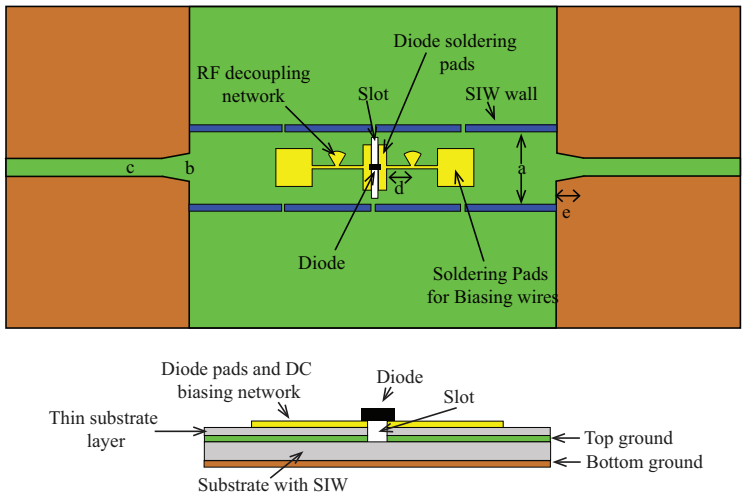

Figure 5.4 Layout of the fabricated switch.

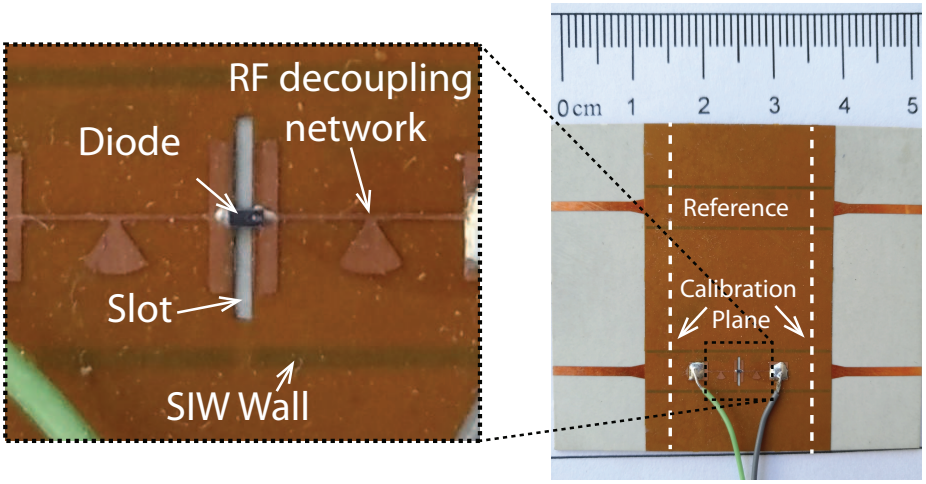

Figure 5.5 Fabricated switch prototype.

Also, an RF decoupling network is required to cutoff RF signal flow in the DC-biasing network. This can be achieved by introducing open-circuited quarter wavelength stubs in DC-biasing networks. These stubs are placed at quarter wavelength distance from the diode soldering pads, effectively creating an RF open-circuit at these pads. This allows DC-biasing while blocking the RF signal flow in the DC-biasing network. Such an RF decoupling networks can be introduced on each side of the slot as shown in Figure 5.4. Thin laminate along with the RF decoupling networks provide the required DC isolation and RF coupling for proper operation of the proposed switch. For the prototype fabrication, RT/Duroid 6002 of 0.508 mm thickness from Rogers Corporation is used as the substrate and 25 micron thick Kapton laminate is used for DC isolation. A picture of the fabricated prototype is shown in

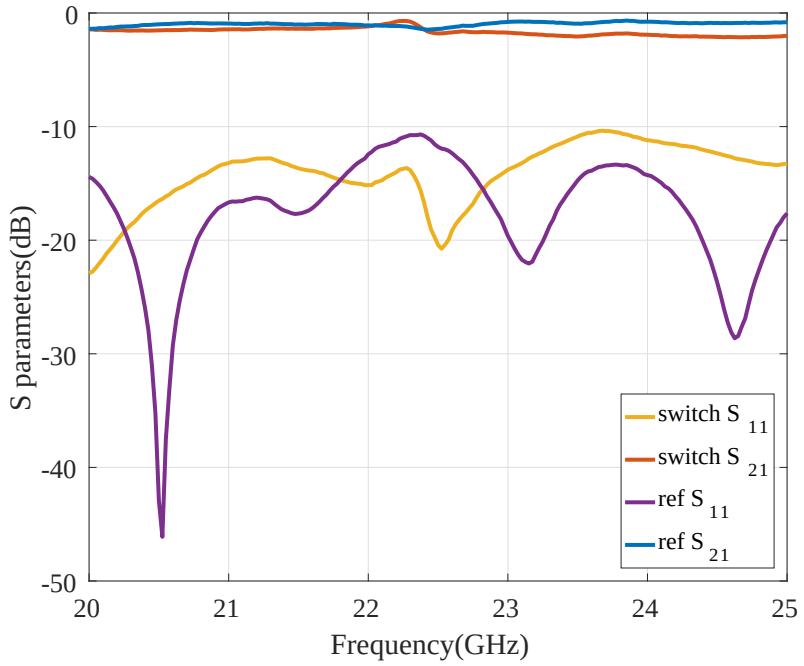

Figure 5.6 Measured S parameters for on-state switch and a reference line.

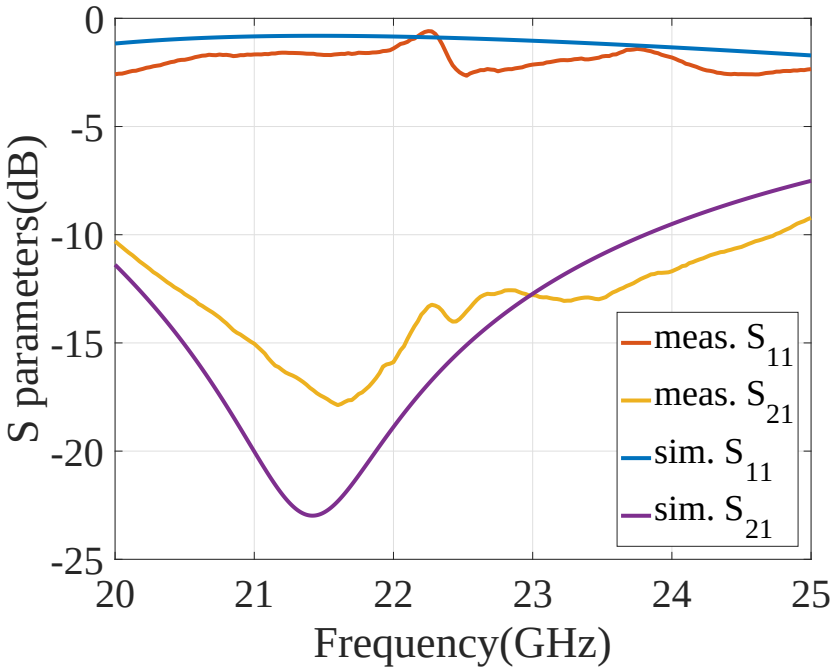

Figure 5.7 S parameters of switch in off-state.

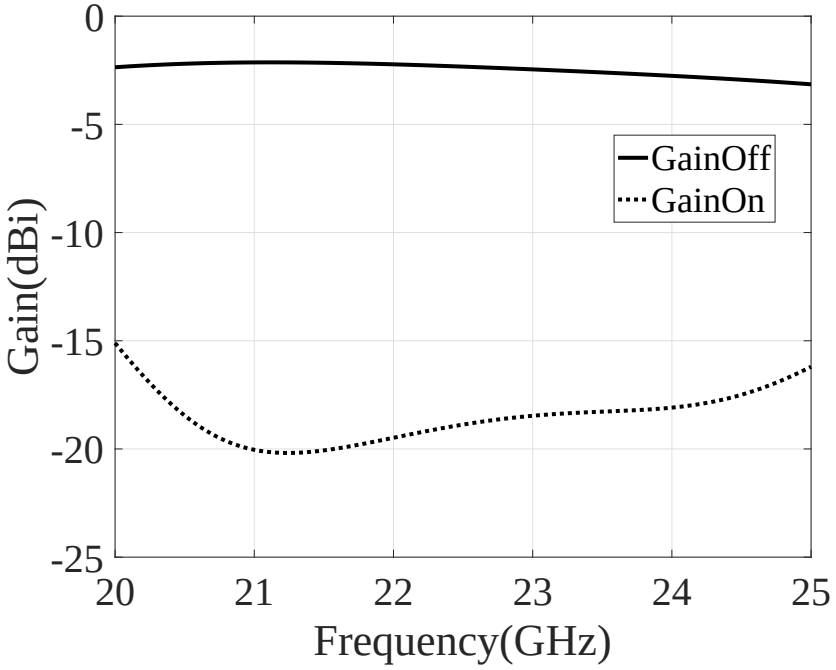

Figure 5.8 Simulated broadside gain for the switch in on- and off-state.

Figure 5.5.

For the on-state switch, the diode is forward biased, eliminating the slot impedance by short-circuiting it at its middle. The switch is in the off-state when the diode is reverse biased, realizing a high impedance slot on the SIW loaded with the reverse biased diode capacitance.

The S parameters for the two switch states of the fabricated prototype are shown in Figures 5.6 and 5.7, respectively. The SIW is connected to a VNA through an SIW to microstrip transition. A TRL calibration kit was also fabricated in SIW technology to eliminate the effects of this transition. For the on-state case, the insertion loss of the switch is determined by comparing the transmission coefficient with that of a reference SIW line without a switch. The calibration planes and the reference line are shown in Figure 5.5.

The measured on-state S parameters (Figure 5.6) show an insertion loss of 1.3 dB in the 20 GHz to 25 GHz frequency band compared to the reference line. The on-state switch is well matched with the SIW line as the reflection coefficients are less than -10 dB for the whole band of interest. For the off-state switch (Figure 5.7), the transmission isolation is more than 10 dB for 20 GHz - 23.8 GHz (17.5% at 22 GHz) and 20 GHz to 24.6 GHz (21% at 22 GHz) bands for simulations and measurements, respectively. In comparison, a recently reported SIW switch design with similar topology [57] operating in the X-band had an on-

state insertion loss of 2.55 dB and an off-state isolation of 10 dB within a bandwidth of 23%.

As a slot is a radiating structure, using it as a switch may result in unwanted radiation that can interfere with some other signal source. Hence, it is important to analyze the radiating characteristic of the switch. Simulated broadside gains for on- and off-state switch are shown in Figure 5.8. These gain show that the slot is radiating in off-state with maximum broadside gain of -2.1 dB. On the other hand the gain is quite low in on-state switch. These gain values are in line with our understanding of the proposed switch as the switch slot is resonant in off-state causing weak radiation due to its high impedance. For on-state switch, the slot is nonresonant, resulting in very low radiation gain. The off-state radiations interference with a linearly polarized source can be avoided by rotating the switching slot from $45^o \leq \theta \leq 90^o$ without significantly affecting the off-state transmission isolation.

5.4 Conclusion

A simple SIW switch is presented in this chapter. A SPST switch is designed and fabricated in K-band to validate this concept. The fabricated switch provided maximum measured insertion loss of 1.3 dB in on-state and minimum isolation of 10 dB in off-state for 21% bandwidth at 22 GHz. The radiation characteristics of this slot based switch are also analyzed in this chapter. A good agreement is observed between the measured and simulated results. The proposed switch topology is simpler as compared to the previously proposed switches for substrate integrated waveguide. This switch can easily be integrated in the feed network of the proposed retroreflector to introduce amplitude modulation in the reflected signal.

CHAPTER 6 W-BAND RETROREFLECTOR TAG WITH POLARIZATION AND AMPLITUDE MODULATION

This chapter presents the proposed tag to improve automotive targets radar cross section (RCS). This tag reflects the incident signal in the direction of incidence. This property is known as retroreflection. It helps to achieve higher RCS at various radar to target incident angles as compared to surfaces without retroreflection. The tag also integrates polarization and amplitude modulation to further enhance the target delectability. Polarization modulation is achieved in this tag by using the radiating elements introduced in Chapter 4. Amplitude modulation is incorporated by using the switch concept presented in Chapter 5. Tags are designed and fabricated in the band allocated to the automotive radar (76 GHz - 81 GHz) to validate the concept.

The retroreflection characteristic of the proposed tag is achieved by arranging the one-dimensional arrays (Chapter 4) in a Van-Atta array configuration. FoV, structure components and design procedure of the tag are discussed in this chapter. Monostatic and bistatic RCSs are used to characterize the fabricated prototypes. Fabrication tolerances are analyzed by comparing the measured results with the simulations.

A brief tag description and its comparison with other retroreflectors described in the literature are presented in Section 6.1. The Van-Atta array, radiating elements, modulation switch, and tag delay lines are presented in Section 6.2. Fabricated prototypes, measurement setup and procedures, and measured and simulated result are discussed in Section 6.3. Finally, the chapter is concluded in Section 6.4.

6.1 Introduction

Electrically large targets such as cars exhibit complex RCS. This RCS varies significantly with slight change in the target orientation [66]. This inconsistent RCS can hinder the application of super resolution algorithms in the proposed collision avoidance system. This problem can be solved by improving the automotive targets RCS with the help of reflectors that enhance their visibility to the automotive radars for a large range of target orientation.

Design of such reflector is constrained by its application. An efficient reflector should reflect back the incident signal in the direction of incidence. This type of reflectors are known as retroreflector. The designed reflector should provide retroreflection for wide field of view (FoV). The operating band of this reflector should match with that of an automotive radar.

This tag should also be capable of modulating the reflected signal in order to facilitate the target detection. Additionally, cost is an important factor to consider in designing this tag.

The simplest form of retroreflector is a corner reflector. However, it has high profile and limited functionality. Active phase conjugation methods [67, 68, 69] provide enhanced functionality at the cost of complex and expensive systems. On the other hand Van-Atta arrays [70] provide perfect compromise between system complexity and functionality. It has simple and low-cost structure. Radiating elements can also be designed based on the concepts introduced in Chapter 4 to have wide FoV and polarization diversity. The reflected signal can be modulated by introducing modulators in the delay lines [71, 72]. Hence, for the proposed system, a Van-Atta array based tag is designed to ameliorate the target RCS.

Several retroreflectors can be found in the literature. A rectangular patches based retroreflector is presented in [73]. In this work, coplanar waveguides based transmission lines connect series fed rectangular patch arrays to realize a retroreflector at 26 GHz. The adjacent distance of the rectangular patches is 0.8λ. This distance is a limiting factor for wide FoV of this retroreflector. Due to this large distance, the reflector losses its retroreflection property at wide incident angles due to grating lobes caused by high interelement distance. For uniform linear arrays with interelement distance of 0.8λ, the grating lobes start raising above -10 dB level relative to the main beam at $\pm 8^{o}$ of beam steering. Hence, the FoV of the retroreflector is limited to 16^{o}. These grating lobes will reflect the incident signals in unwanted directions, reducing the tag RCS and causing interference for nearby systems. Rectangular patches are replaced by single polarization slots in SIW in [74], operating at 30 GHz. The interelement spacing for Van-Atta array is 0.7λ in this case. A RCS enhancing rectangular patch based retroreflector is presented in [75] for low profile targets such as human beings. This reflector operates at 77 GHz at single linear polarization with interelement spacing of 0.77λ. A circular polarized reflector operating at 25.45 GHz is presented in [76] with interelement distance of 0.75λ. All these reflectors have high interelement distance, limiting the broadside FoV.

In addition to linear or circular polarizations, reflectors with different incident and reflected signal polarization are also available in the literature. A wideband linearly polarized slot is used to realize a W-band polarization rotating retroreflector in [77]. This reflector has limited elevation beamforming capacity due to the wideband slot. Distance between the adjacent slots is 0.79λ at 79 GHz with FoV of $\pm 17^{o}$. An L-band polarization rotation reflector for airborne synthetic aperture radar calibration is presented in [78] with interelement distance of 0.7λ.

In this chapter, a wide FoV retroreflector tag is designed using polarization diverse antenna arrays presented in Chapter 4. The interelement distance of the proposed tag is 0.48λ at

79 GHz. Due to this small distance, the FoV of the designed tag is limited by the radiation pattern characteristics of the radiating slots, while limiting the grating lobes under -10 dB for 120^o beamscan. Beamforming in the elevation direction allows to control FoV in this plane. Arbitrary incident and reflected signal polarizations can be realized by using the propose radiating elements. The reflected signal can also be modulated by adding amplitude modulators in the delay lines. A 90^o polarization rotation tag with amplitude modulation is designed and prototyped in this chapter.

6.2 Tag Concept and Design

A Van-Atta array implements phase conjugation by connecting corresponding radiating elements in the array with equal length delay lines to achieve a center symmetric structure as shown in Figure 6.1(a). The phase conjugation directs the reflected signal in the direction of incidence without introducing active components in the structure. The FoV of the resulting array depends on the radiation patterns of the radiating elements and their interelement distance. For the automotive application, this FoV is directed by the automotive radar [79], as shown in Figure 6.1(b). This figure shows that the tag is required to have 120^o retroreflective FoV in azimuth plane. The beamforming in the elevation plane is required to have narrow FoV in this plane to avoid unwanted reflections from roads and overhead installations. However, this elevation FoV should be wide enough to cover the terrain unevenness. For this application, 9^o half-power FoV is targeted for this plane. The tag should operate in the band allocated to the future automotive radar i.e. 76 GHz -81 GHz [80].

The radiating elements and arrays for X and Y polarizations are shown in Figure 6.2. The radiating elements (Figure 6.2(a) and (b)) are slots on cavities which are excited by coupling slots on SIWs. The radiating slot is rotated to realize polarization diverse antenna arrays. The coordinate system shown in this figure defines the polarization states of these radiating elements. Series fed one dimensional configuration of these radiating elements (Figure 6.2(c) and (d)) provide fan beam with wide and narrow FoV are in the tag's retroreflector and elevation planes, respectively. The HPBW of these arrays defines the elevation FoV of the retroreflector tag.

A Van-Atta array can be realized using these one-dimensional arrays as shown in Figure 6.3. The polarization diverse arrays are alternated in YZ-plane with respect to their centers. This configuration allowed to reduce the length of the delay lines upto 14%. This reduction helps to improve the tag performance by limiting the loss in the delay lines that is significantly high due to high tangent loss of the substrate in W-band. However, phase continuity is required along Y-axis after alternating the one dimensional arrays. This continuity is essential to

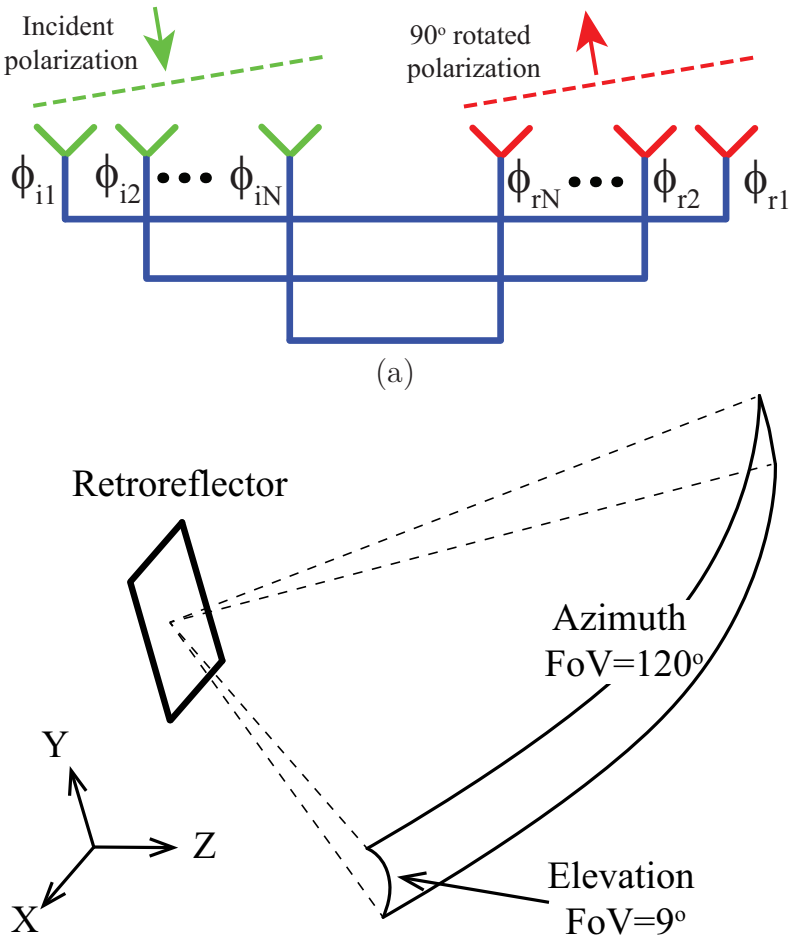

Figure 6.1 Retroreflective tag (a) Van-Atta array description, (b)Required FoV.

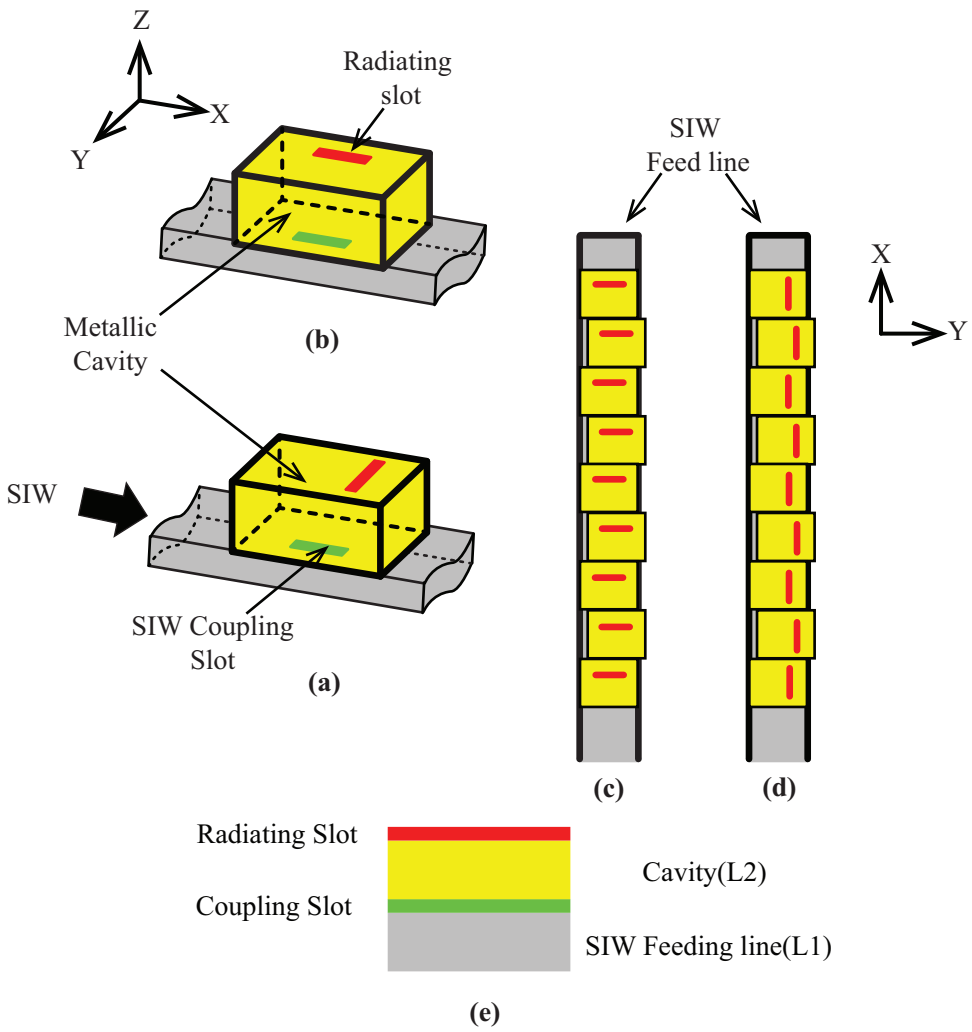

Figure 6.2 Building blocks of Van-Atta array (a) X-pol radiating element, (b) Y-pol radiating element, (c) nine element X-pol array, (d) nine element Y-pol array, (e) layers stackup.

direct the beam in broadside direction. If this alternated configuration causes out of phase excitation along Y-axis, radiating slots in one of the adjacent array can be mirrored with respect to the center of the cavity to create a 180° phase shift in the radiated signal. This mirroring allows to avoid alternation in the delay lines that can complicate the Van-Atta array design.

As mentioned in Chapter 4, the one-dimensional arrays are designed with compact size. This compact size provides interelement distance of 0.48λ at 79 GHz for the designed Van-Atta array. Smaller interelement distance results in 120° beam steering while limiting the grating lobes under -10 dB level with respect to the main beam.

The delay lines are designed to have same phase delay for all the Van-Atta array pairs at

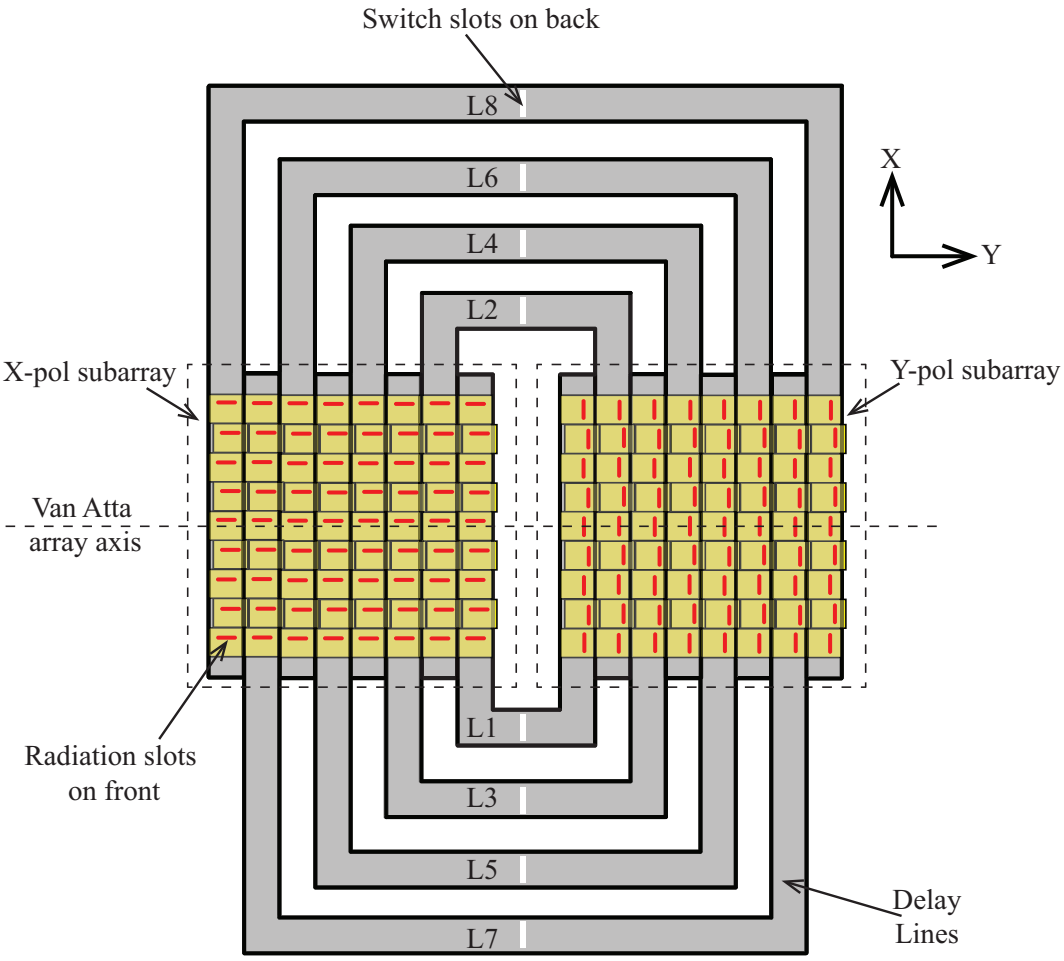

Figure 6.3 Description of the proposed retroreflective tag.

the design frequency (77 GHz). The same phase delay can be achieved by having equal physical lengths of all the delay lines. This equal phase condition can also be achieved by using different physical length transmission lines with length variation equal to an integral multiple of the guided wavelength inside the transmission line. Equal physical length delay lines would be preferred as they provide the retroreflection for the whole band of the radiating elements. Different physical length delay lines have different phase slopes, satisfying the equal phase condition for only one frequency. A beam squint is expected as we deviate from the equal phase frequency due to different phase slopes for different physical length delay lines. As the phase slope depends on the physical length of a transmission line, limiting the line length of the delay lines using the alternating configuration limits the phase slope, increasing the retroreflection bandwidth of the designed tag.

Though equal physical length delay lines are desirable, realizing these lines for planar technology is quite challenging. Crossovers in planar technology are essential to achieve equal length delay lines, however, they can increase coupling between the lines and result in a nonlinear phase slope [81].

6.2.1 Tag design

As discussed in Chapter 4, one-dimensional arrays were prototyped to validate their bandwidth and radiation patterns [82]. The measured reflection coefficients for X- and Y-polarized arrays are shown in Figure 6.4(a). The design frequency for the tag is 77 GHz. Hence, all the one dimensional arrays were designed at this frequency. However, due to the fabrication and material characteristics tolerances, up to 3% of frequency variation is observed in the measurements. The measured S_{11} graphs show that the arrays with both polarizations have about 2.5% -10 dB bandwidth at 79 GHz.

The measured radiation characteristics shown in Figure 6.4(b) illustrates that both arrays provide fan beams. In the principal planes parallel to the array axis, the HPBWs are 10^o and 9^o for X and Y polarizations, respectively. In the perpendicular principal planes, Y-polarized array provides wider FoV in comparison with the X-polarized array due to the orientation of the radiating slots. The HPBWs in the principal plane parallel to the array axis determine the elevation FoV of the tag and the perpendicular principal plane is the plane of retroreflection where wide FoV is desirable.

After validating the building blocks of the proposed tag, delay lines were designed to realize a Van-Atta array. Those are SIW lines, designed to have equal phase at the design frequency. The transmission phase of these lines is shown in Figure 6.5(a). All the lines have some phase deviation at 77 GHz, with a maximum phase variation of 6.2^o for all delay lines.

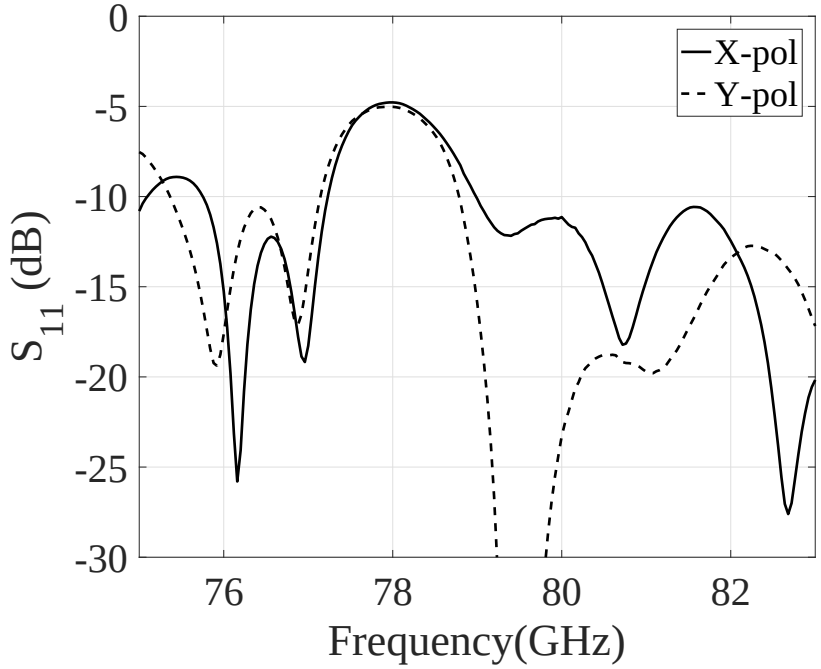

(a)

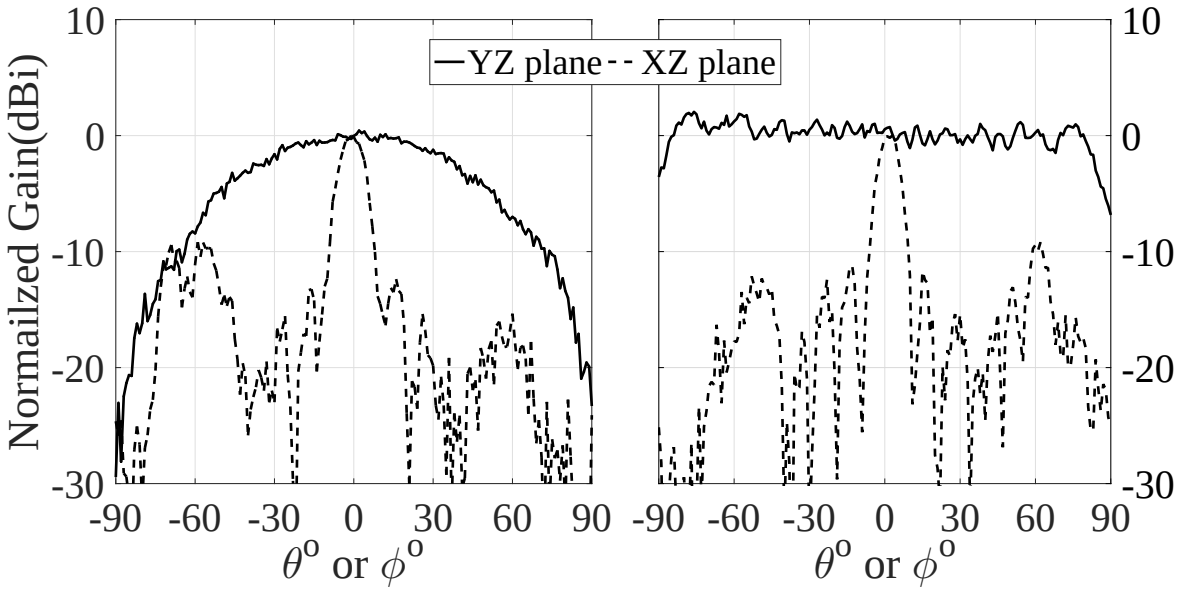

(b)

Figure 6.4 Tag elements characteristics, (a) S parameters, (b) Radiation patterns for X-pol (left) and Y-pol (right) one-dimensional (1×9) arrays.

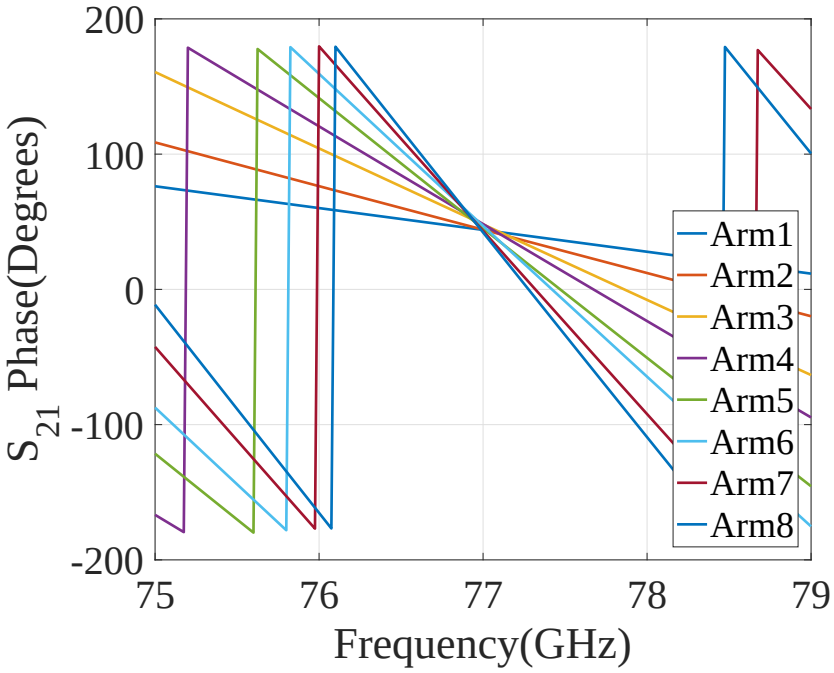

(a)

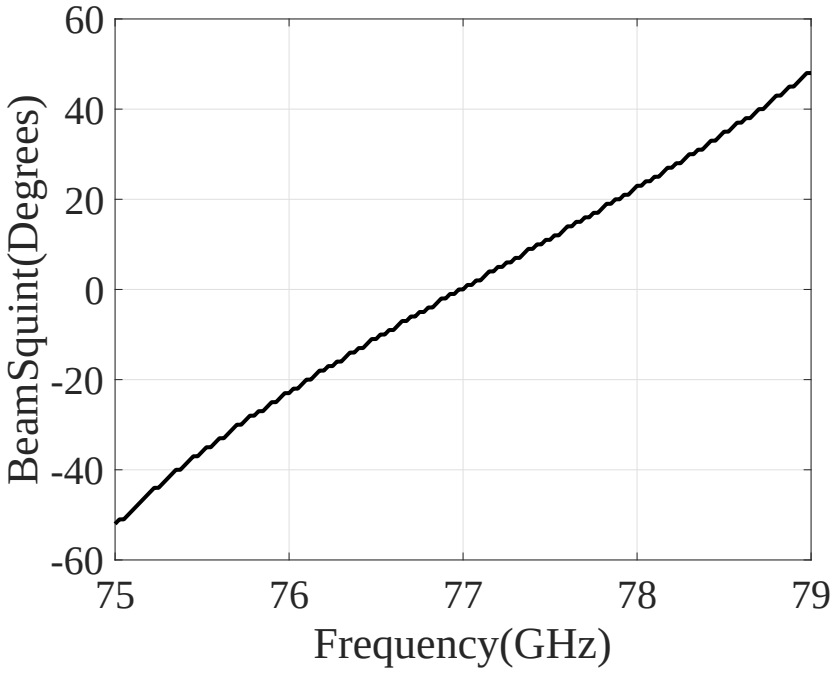

(b)

Figure 6.5 Delay lines simulated characteristics, (a) Transmission phase, (b) Beam squint with frequency.

Fine line length adjustment is required to eliminate this error which is quite challenging to fabricate with the available fabrication process. Deviation from the design frequency causes a progressive phase between the adjacent elements, resulting in a beam squint in the retroreflector from the direction of incidence.

The beam squint due to phase error can be analyzed using the magnitude and phase of the delay lines. For a broadside incidence, the magnitudes and phases of the delay lines are related to the beam squint by the following array factor equation:

$$AF(\theta) = \sum_{n=1}^{8} A_n e^{jkndsin\theta+\alpha_n}; -90^o \leq \theta \leq +90^o \tag{6.1}$$

where A_n and α_n are the magnitude and phase of the transmission coefficient of the nth delay line, respectively. The beam squint with respect to frequency is plotted in Figure 6.5(b). This figure show that the beam squint rate around the design frequency is approximately 23^o/GHz.

6.2.2 Switch Concept

Using amplitude modulation, additional information can be induced in the reflected signal. Moreover, the signal to noise ratio (SNR) can also be enhanced. Hence, a tag with modulation can enhance the system performance and functionality. Amplitude modulation can be introduced in Van-Atta arrays by adding switches in the delay lines.

A switch can be implemented by realizing a switchable high impedance on a transmission line. An inclined diode loaded slot, placed at the center of an SIW can act a switchable load as discussed in Chapter 5. The switch model is shown in Figure 6.6(a). For a reverse biased diode, the resonant slot acts as a series high impedance load, impeding the signal transmission. In case of a forward biased diode, the slot is short-circuited at its center, shifting its resonance frequency outside the band of interest. This eliminates the high impedance of the slot from the SIW, resulting in a high transmission through the waveguide.

A hard-wired switch was prototyped in W-band as shown in Figure 6.6(b) to validate the concept. A slot on an SIW behaves as an off-state switch. For the on-state switch, the slot is short-circuited at its center to emulate a forward biased PIN diode. The measured off-state switch S parameters, shown in Figure 6.7(a), show at least 12 dB of isolation in the band of interest. The measured S parameters of on-state switch are shown in Figure 6.7(b) along with the S parameters of a reference SIW line of same length. A comparison between the transmission coefficients of the reference line and the hard-wired on-state switch shows negligible switch insertion loss. Thus, an amplitude variation of at least 10.6 dB can be

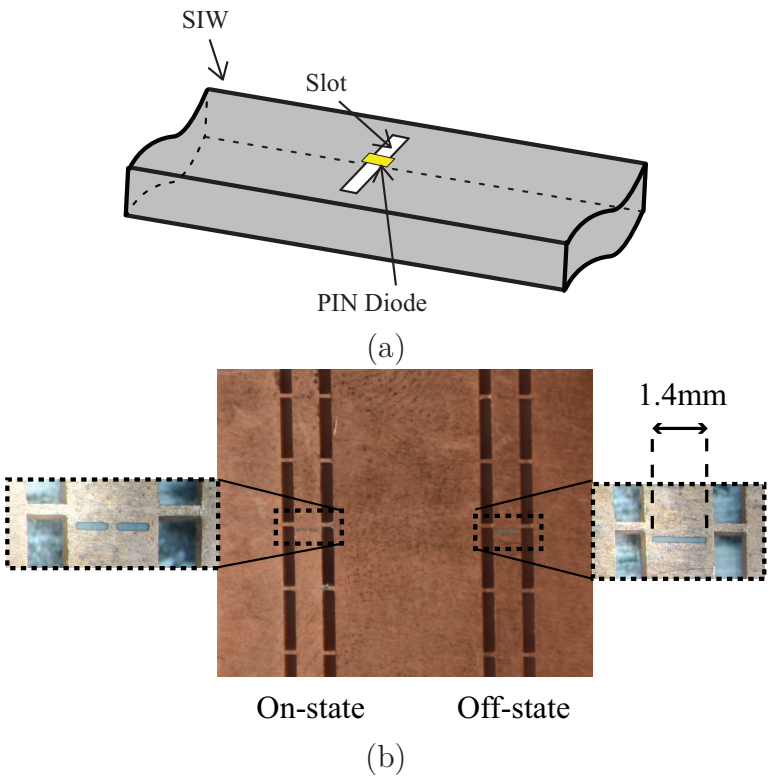

Figure 6.6 Switch concept. (a) layout, (b) hardwired prototype.

achieved between the on and off state by using this type of switch.

The proposed switch topology can be easily integrated with the tag by adding slots on delay lines as shown in Figure 6.3. The amplitude modulation of the proposed tag is characterized by measuring the monostatic RCS of tag prototypes with and without the switch slots. A functional amplitude modulating tag can be realized by loading PIN diodes on the switch slots. However, prototypes with hard-wired switch were fabricated in W-band to study the amplitude variations of the signal reflected by the tag with the two switch states as the PIN diode was not commercially accessible in this band.

6.3 Fabrication and Measurements

The proposed tag was designed using RT/Duiroid 6002 substrate with 0.508 mm thickness using Ansys-HFSS. In this simulator, this substrate is characterized by a dielectric constant and tangent loss of 2.94 and 0.0012, respectively, as given in the manufacturer datasheet. However, these material properties are evaluated in X-band and recommended up to Ka-band. Thus, material properties are expected to change in W-band. This variation is discussed in Chapter 4. The dielectric constant variation is determined by comparing simulated and

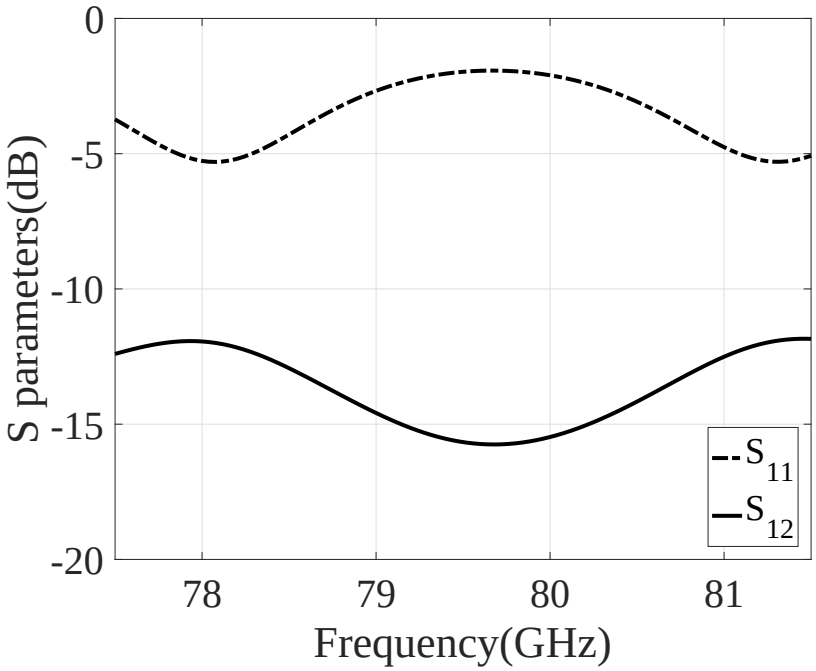

(a)

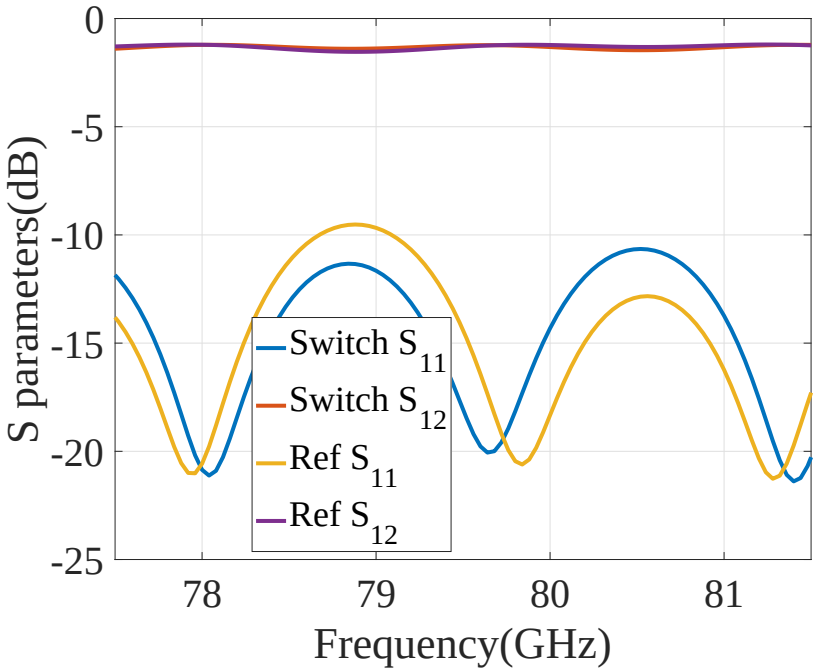

(b)

Figure 6.7 Measured S parameters for hardwired switch. (a) off-state, (b) on-state.

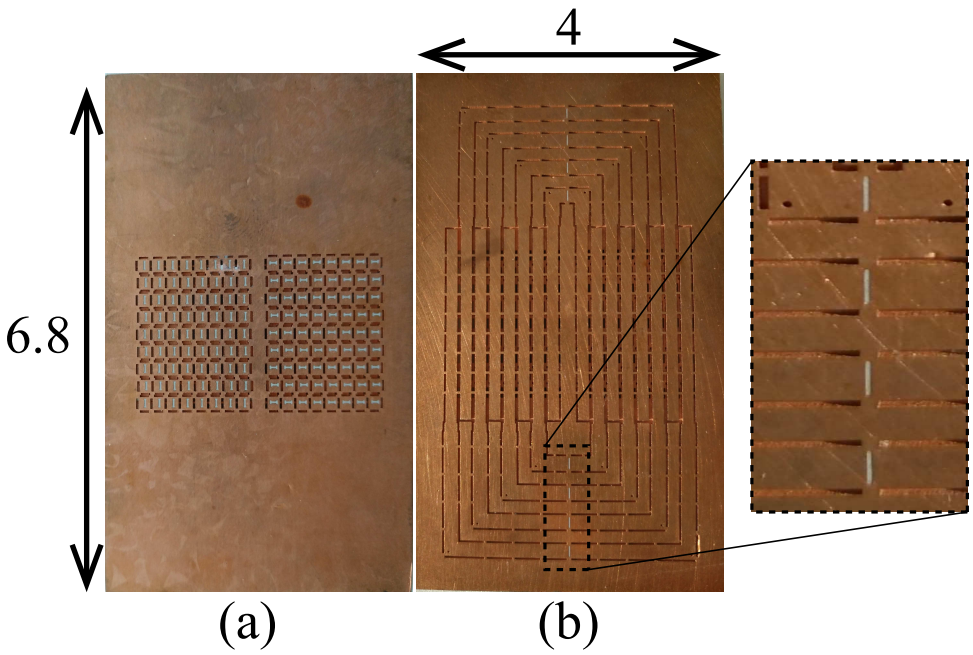

Figure 6.8 Fabricated tag prototypes. (units in cm), (a) Radiating front side, (b) Feeding back side with switch slots.

measured resonance frequency of an SIW cavity. The dielectric constant value is 7% lower in W-band in comparison with the X-band value. This lower value is expected to upshift the operating band of the fabricated prototypes. The tangent loss estimation was made by comparing the simulated and measured insertion loss of a straight SIW segment. The measurements were 0.52 dB/cm lossier than the simulations. This variation can cause lower tag RCS due to losses in the substrate.

The tag is a two-layer structure where the feeding network and delay lines are fabricated in the first layer substrate. The bottom copper cladding of this substrate has switch slots, and coupling slots are etched out on its top cladding. The cavities are implemented in the second layer. This layer is aligned with the first layer such that the coupling slots on the first layer excite the second layer cavities. The radiating slots are etched on the top copper cladding of the second layer. The two layers are fabricated separately and then stacked together with 5 microns adhesive layer inbetween under high temperature and pressure.

In the fabrication process, the metallic walls of SIWs and cavities are realized by laser machining through the substrate and followed by electroplating of the resulting slots. A chemical process is used to etch out the coupling and radiating slots from the substrate copper cladding treated with a photosensitive mask. Laser machining, manual alignment of the photosensitive mask and layers stack up cause fabrication tolerances that may account for the discrepancies

in the measured results. Tags with and without switch slots were prototyped as shown in Figure 6.8.

6.3.1 Measurement Setup

An in-house measuring setup was established to characterize monostatic and bistatic RCS of the proposed tag as shown in Figure 6.9. In this setup, the tag is installed on a manually controlled turntable. The tag can be rotated by an angle χ about its axis in the retroreflective plane using this turntable. A transmitter (Tx) horn antenna is installed on a rotating arm placed at an angle θ with respect to the normal direction of the tag. This arm places the transmitter at a distance of 72.5 cm from the tag. A fixed receiver is placed at a distance of 75 cm from the tag pivoting axis. The receiver (Rx) is placed slightly higher than the rotating transmitter to facilitate the transmitter rotation. The tag height is properly adjusted to make sure that it is within the transmitter and receiver horn antenna main beam during the measurements.

A waveguide twist is used to rotate the transmitter horn antenna about its axis to make the transmitter and receiver horn antennas 90^o out of polarization. This results in a horizontal and vertical polarizations for transmitter and receiver, respectively. The transmitter and receiver antennas are identical corrugated horns, model QRR-WOOY75 from Quinstar with 25 dB of measured gains. The cross-polarization level for these antennas is -23 dB in the main beam direction, affecting the measured RCS around the broadside of the tag where structural reflections are stronger than the polarization-rotated signal reflected by the tag.

Keysight PNA-X N5247A vector network analyzer (VNA) is used to measure the tag RCS. The horn antennas were connected to Virginia diode (VDI) VNA extenders, extending the VNA operating frequency in W-band. The VNA was calibrated in the 75 GHz to 83 GHz frequency band and the transmission coefficient (S_{21}) were recorded to calculate the tag RCS. Monostatic and bistatic RCS measurement process is illustrated in Figure 6.9(b). The evaluation of the tag elevation FoV is also demonstrated in this figure. Monostatic RCS can be evaluated by rotating the tag on the turntable with fixed Tx and Rx horn antennas at $\theta = 0^o$. This procedure is the same as rotating the Tx and Rx together. The S_{21} is recorded with a resolution of $\theta = 1^o$. The radar equation can then be used to relate this transmission coefficient with the tag RCS σ as shown below:

$$\sigma = S_{21} + 10log_{10}\left(\frac{(4\pi)^3 R_1^2 R_2^2}{G^2\lambda^2}\right) \tag{6.2}$$

where S_{21} is recorded by the VNA, R_1 and R_2 are the tag distances from the Tx and Rx, G

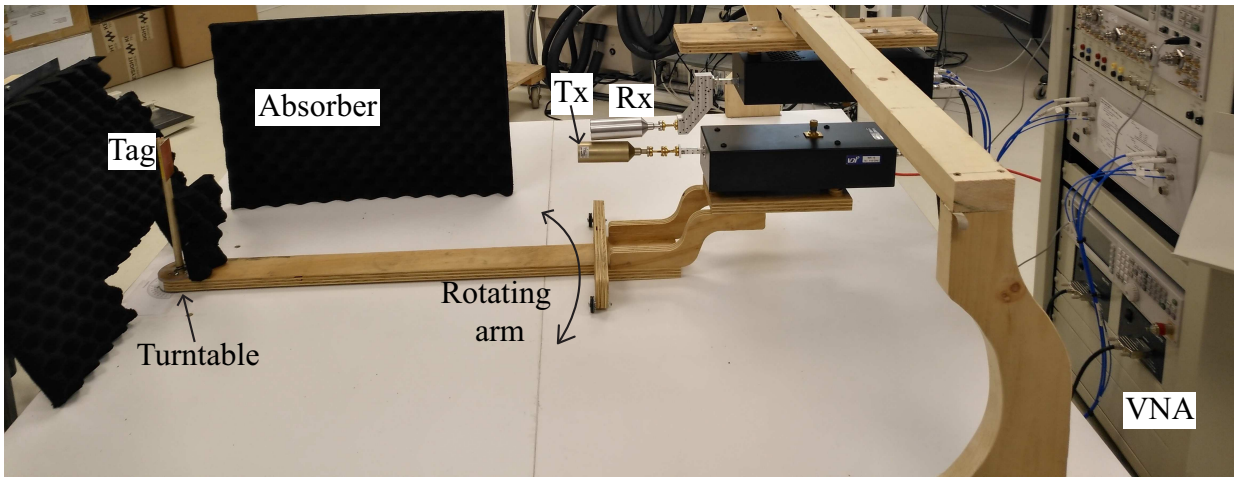

(a)

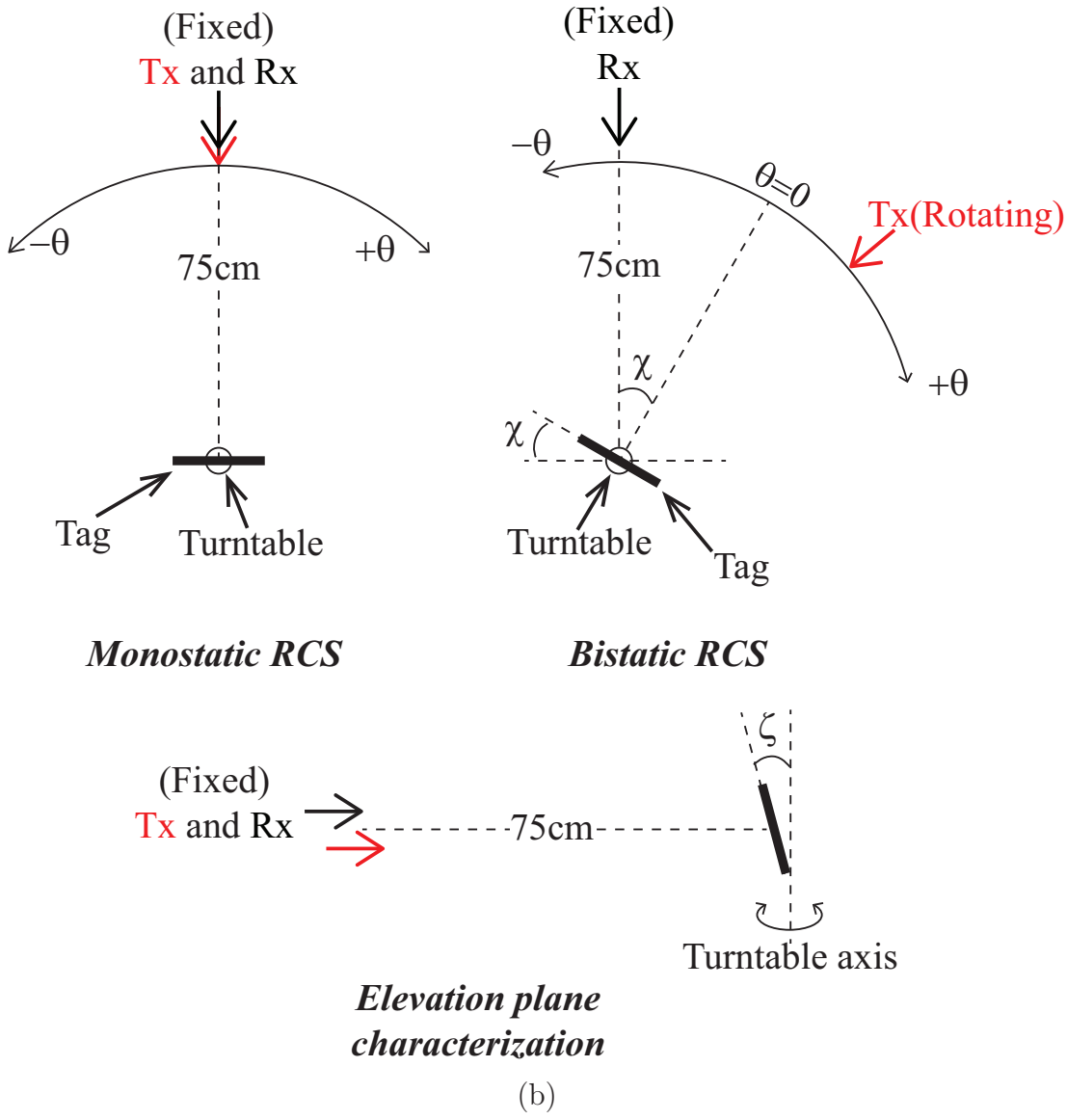

(b)

Figure 6.9 Measurement arrangement, (a) Setup, (b) Process description.

is the transmit and receive horn antenna gain and λ is the operating wavelength.

Strong structural reflection at the broadside of the tag is used to calibrate the system. The tag is rotated on the turntable to maximize the measured S_{21}, marking this angle as $\theta = 0^o$.

For bistatic RCS measurements (Figure 6.9(b)), the receiver is fixed and the transmitter rotates around the tag pivot. First the setup is calibrated as mentioned in the monostatic case and then the tag is rotated at an angle χ. The transmitter reference angle (θ=0) is set in the direction normal to the tag, as shown in Figure 6.9(b), for better presentation of the measured data.

6.3.2 Measurements of Fabricated Prototypes

The tag bandwidth can be characterized by observing its frequency response in the band of interest. In Figure 6.10, the tag monostatic RCS, averaged over the range $\theta = -60^o$ to $\theta = 60^o$ with 1^o resolution is plotted with respect to the frequency. The narrow retroreflective bandwidth is due to the use of different length delay lines, satisfying the phase conjugation criteria for only one frequency. A beam squint is expected with the deviation from the design frequecny, lowering the monostatic RCS. The tag is providing maximum monostatic RCS at 78.6 GHz. The measurements presented in the rest of this sections are taken at this frequency.

Ansys-HFSS simulation was used to estimate the RCS of the designed tag at 77 GHz (the simulation uses substrate permittivity value of 10 GHz, leading to phase conjugation at 77 GHz). The performance of the fabricated prototype is compared with the simulation model in Figure 6.11. The measured monostatic RCS for an aluminium sheet of $0.3 \times 0.3 m^2$ size is also presented in this figure to demonstrate the retroreflection effect of the tag. The fabricated prototype exhibits about 10 dB loss in comparison to the simulation. Higher tangent loss in the substrate can contribute to this discrepancy. Beam squint due to the phase errors in the delay lines can also contribute to this loss. In comparison with the reflections from the aluminium sheet, the designed tag RCS is at least 15 dB higher for 90^o rotated incident and reflected signals for almost whole 120^o FoV. For the broadside direction ($\pm 5^o$), the sheet reflections are stronger due to the limited cross-polarization isolation of the Tx and Rx horn antennas used in the measurement setup. It is important to note that the metal sheet is not illuminated uniformly by the Tx and Rx horn antennas due to their narrow beam. Additionally, the horn antennas are in the near field of the sheet. Hence, Equation 6.2 can not predict the sheet monostatic RCS. However, the reflections from the sheet can be used to demonstrate the retroreflection effect of the tag.

Simulated bistatic RCS of the designed tag is shown in Figure 6.12 for different values of χ

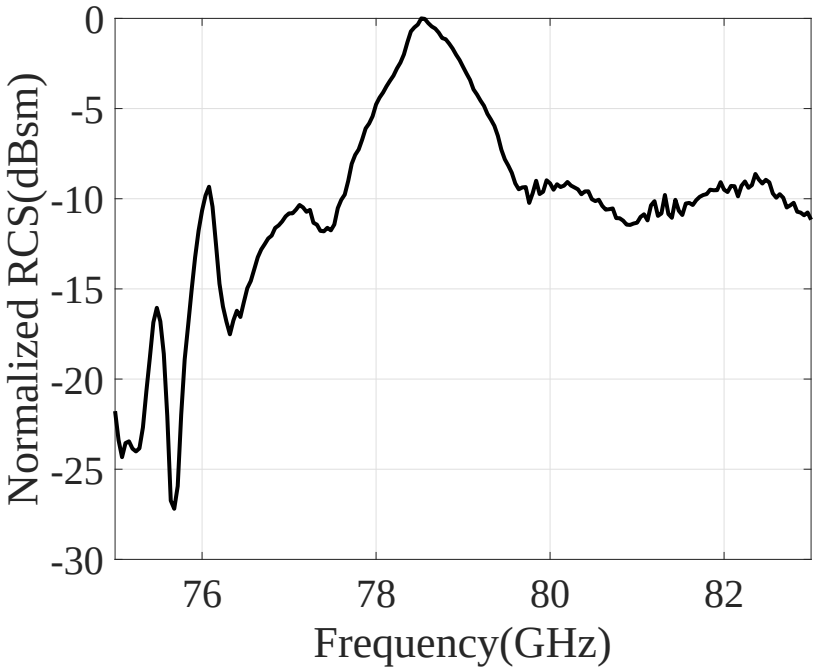

Figure 6.10 Averaged normalized monostatic RCS for the tag.

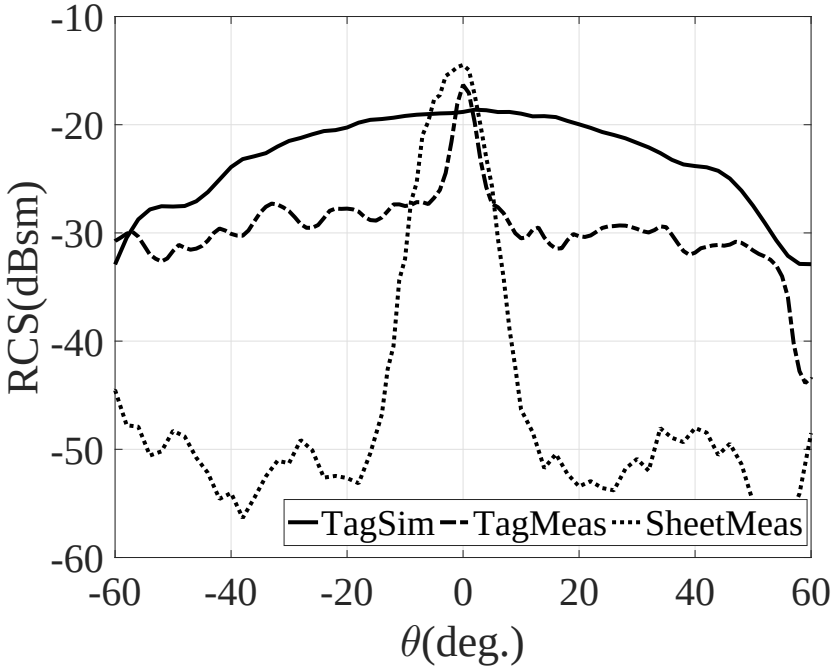

Figure 6.11 Simulated (at 77 GHz) and measured (at 78.6 GHz) monostatic RCS of the tag along with measured RCS of $0.3 \times 0.3\text{m}^2$ metal sheet.

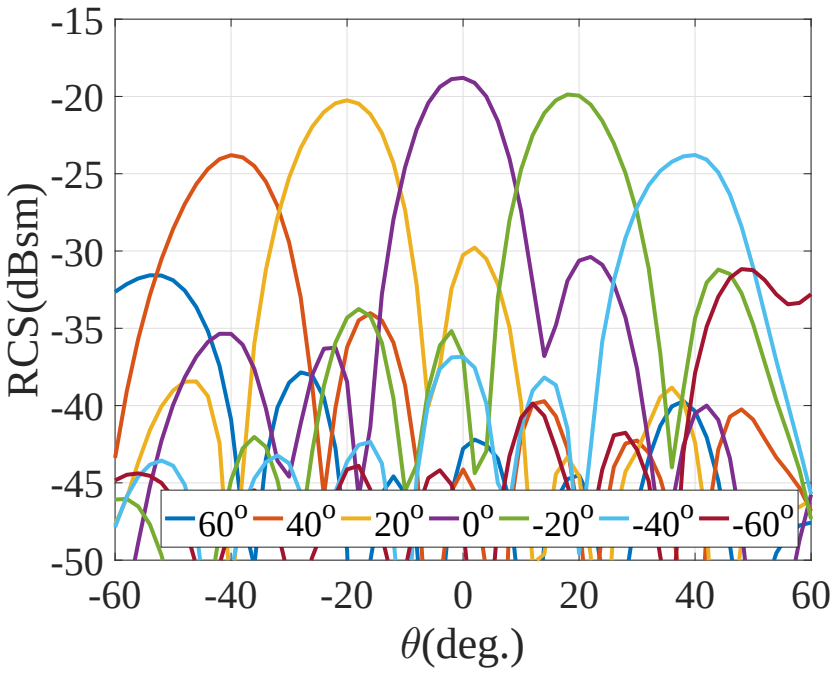

Figure 6.12 Simulated bistatic RCS of the tag at 77 GHz for different values of χ.

defined in Figure 6.9(b). The maximum RCS is achieved for $\theta = -\chi$. Moreover, the simulated bistatic RCS has only one main beam and the grating lobes for all χ values are limited under -10 dB level, hence, satisfying the design criteria set for the tag design. Additionally, a drop in the RCS is observed for $|\theta| > 50^{o}$, mainly due to the retroreflector array elements' radiation pattern shown in Figure 6.4.

Reflected beam squint and phase errors in the delay lines can be perceived by observing the measured bistatic RCS. This RCS for four different frequencies with $\chi = -40^{o}$ is shown in Figure 6.13. Considering the impedance bandwidth of one dimensional arrays (Figure 6.4(a)), this graph shows that the radiating elements start radiating between 78 GHz and 78.6 GHz where we have maximum monostatic RCS. The band below 78 GHz is outside the impedance bandwidth of the radiating elements. Within the impedance bandwidth, the reflected beam squints with increase in the frequency as predicted in the previous section. The gain of the reflected beam reduces with the squint angle increase due to X-polarized elements' radiation pattern. The beam squint rate of the reflected beam is almost the same (23^{o}/GHz) as predicted by the simulated transmission coefficient magnitude and phase of the delay lines (Figure 6.5(b)).

In Figure 6.13, the maximum bistatic RCS, measured at 78.6 GHz, is at $\theta = -47^{o}$ for $\chi = 40^{o}$. This deviation from $-\theta$ for χ provides some information about the delay line phase

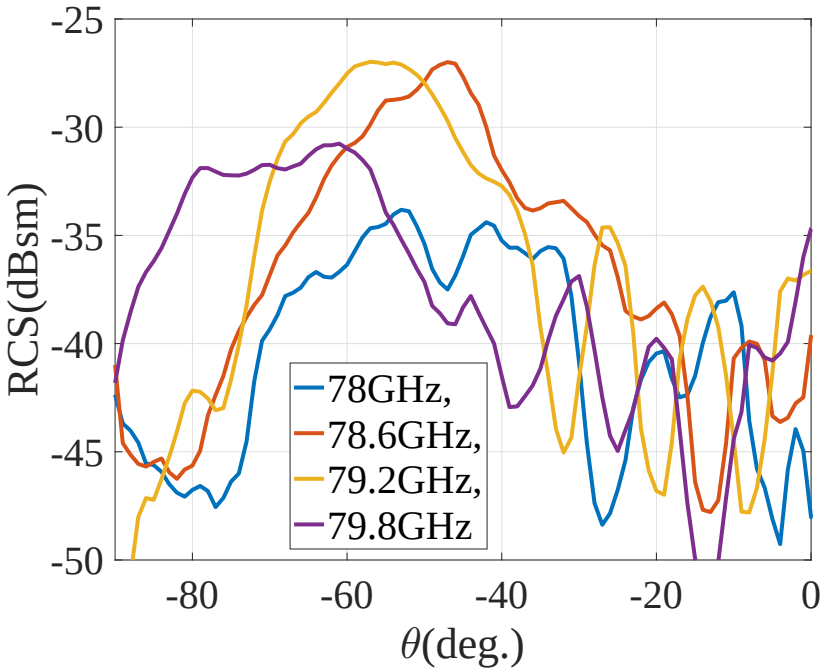

Figure 6.13 Measured tag bistatic RCS variation with frequency for $\chi = 40^{o}$.

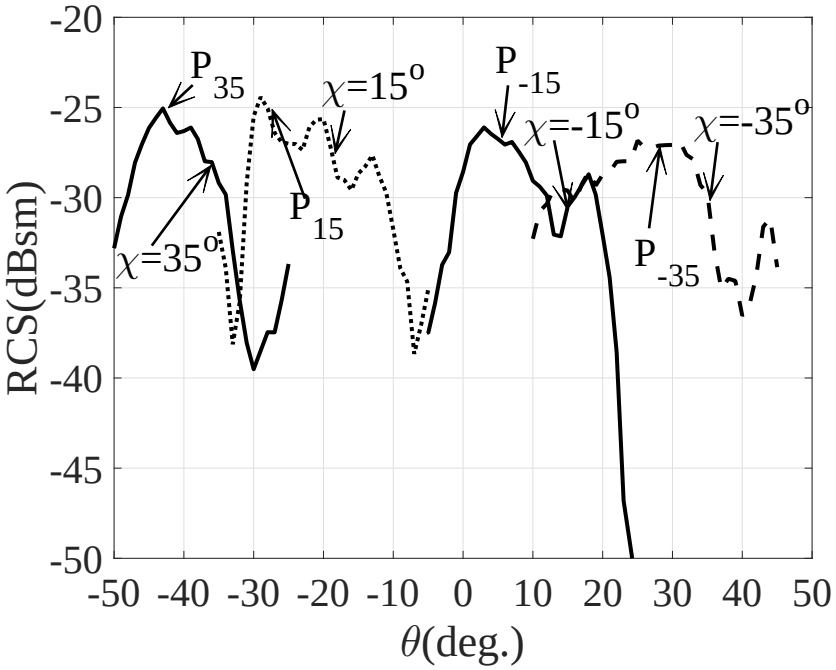

Figure 6.14 Measured bistatic RCS at 78.6 GHz for four different values of χ.

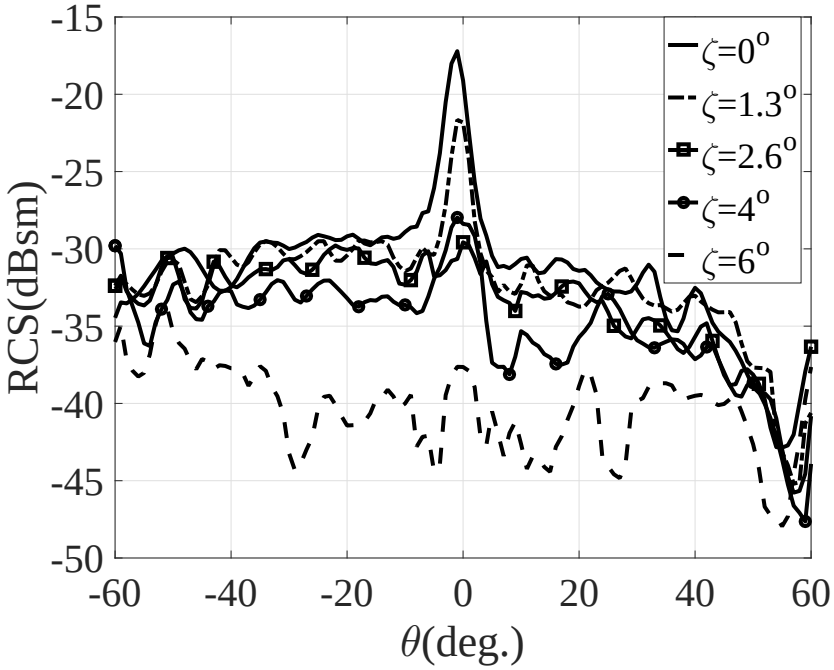

Figure 6.15 Measured RCS variation at 78.6 GHz with different inclination angles.

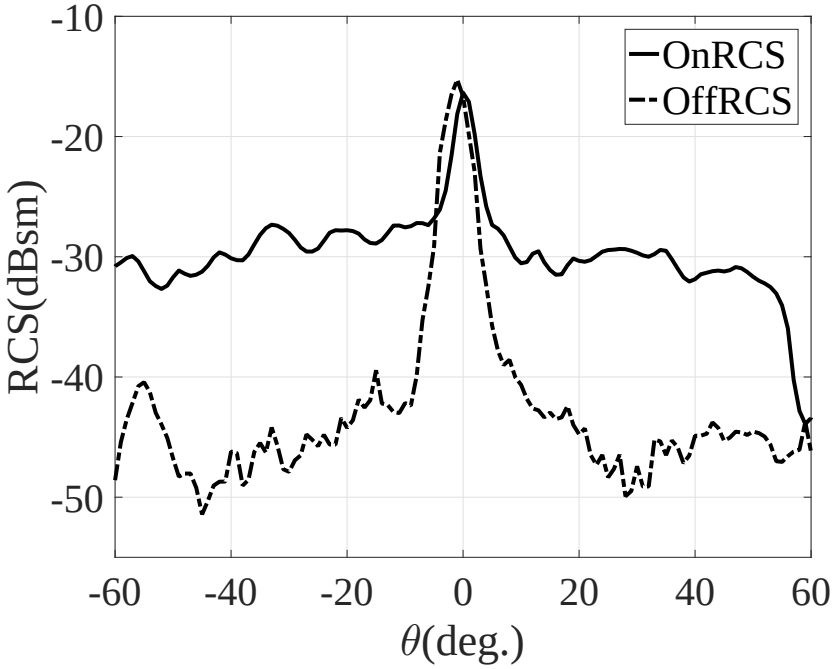

Figure 6.16 Measured monostatic RCS at 78.6 GHz with and without switch slots.

error in the fabricated prototypes. Using the beam squint angle rate with respect to the frequency, estimated from the measured bistatic RCS and simulated delay lines response, it can be stated that the fabricated delay lines provide phase conjugation condition at about 78.3 GHz, which is outside the impedance bandwidth of the retroreflector radiating elements. This phase error is due to the fabrication tolerances that may result in the fabricated SIW with slightly different width. The phase of the delay lines is very sensitive to their width where the simulations show that a width variation of 25 micron shifts the phase conjugation point by 400MHz.

Measured bistatic RCS for different χ values is shown in Figure 6.14. This figure validates that the estimated beam squint is almost the same for different χ values due the the phase error in the fabricated delay lines as predicted in Equation 6.1. This phase error is contributing to the difference between the simulated and measured monostatic RCS, shown in Figure 6.11 by squinting the beam away from the direction of incidence.

The elevation FoV of the tag is characterized in Figure 6.15 by introducing an inclination angle in this plane as shown in Figure 6.9(b). This figure shows that the monostatic RCS decreases monotonically with an increase in ζ. This validates the elevation plane beamforming due to one-dimensional arrays (Figure 6.4) in the designed retroreflector array.

Switching characteristics can easily be added in the proposed tag by introducing a switch slot in the delay lines as shown in Figure 6.3 and 6.8(b). Two switching states were realized by fabricating two tag prototypes, one with and another without switch slots. The monostatic RCS of the two prototypes is shown in Figure 6.16. Outside the strong structural reflection region near $\theta = 0^o$, the difference between the two RCSs is approximately 15 dB, which corresponds to the switch isolation presented in Figure 6.7(a).

6.4 Conclusions

A polarization diverse retroreflective tag, operating in W-band, is presented in this chapter. This tag can provide wide FoV with suppressed grating lobes. The radiating elements, design procedure and fabrication technique are also discussed. A RCS measurement setup and procedures are established to characterize the performance of the proposed tag. Monostatic, bistatic and elevation plane RCS of the fabricated tag prototype are presented in this chapter. The performance of the tag and effect of fabrication tolerances are explained with the help of simulation and measurement results. The tag achieved approximately 120^o FoV while limiting the grating lobes below -10 dB level with respect to the main beam. The tag retroreflection provided 15 to 20 dB higher monostatic RCS in comparison to a flat aluminium sheet for

almost the whole FoV. An amplitude modulation mechanism is also introduced in the tag to modulated the reflected signal. Losses and discrepancies in the fabricated prototype measurement results as compared to the simulations are also addressed in this chapter.

CHAPTER 7 MULTIBEAM W-BAND ANTENNA DESIGN

A multibeam transmit antenna is suggested for the proposed collision avoidance system. This antenna can divide the radar FoV into smaller sectors where each sector is illuminated by a baseband signal orthogonal to the signals of the other sectors. The signal processing unit at the receiver can then distinguish signals reflected within a certain sector. This can help to improve the performance of the super-resolution algorithm used to localize the target by increasing the radar FoV. Such a multibeam antenna is the topic of this chapter.

The proposed antenna consists of a planar Luneburg lens based BFN. A single layer Luneburg lens implementation is suggested for this BFN. Beam ports are placed along the circumference of the lens. The antenna ports are placed in the focused beam region to excite a phased array with desired amplitude and phase distributions. The radiating elements are well known slot arrays on SIW.

Different types of BFNs, brief description of the proposed BFN and previously reported Luneburg lens implementations are presented in Section 7.1. Lens, BFN and multibeam antenna structures are discussed in Section 7.2. Simulation and measurement results of the proposed antenna structure are examined in Section 7.3 to validate the design. Finally, Section 7.4 concludes this chapter.

7.1 Introduction

A phased array based multibeam system can be divided into three main subsystems namely, radiating elements, a BFN and excitations. Radiation from the radiating elements is controlled by the BFN that transforms the excitation fields to amplitudes and phases necessary to radiate with desired directions and beamwidth. BFN can be classified into circuit and quasi-optics based techniques [83]. Couplers and transmission lines are used to realize circuit based BFNs [84, 85, 86]. Field focusing components such as reflectors or lenses are used in quasi-optics based BFN. Parabolic reflectors can be used to realize equal phase plane waves to excite phased arrays as shown in [87, 88, 89, 90, 91]. Parallel plate Rotman lens can also shape the magnitude and phase distributions of the excitations to realize multibeam antennas [92, 93].

Rotman lens based BFN has certain limitations. The maximum beam steering angle and the total number of radiating elements are the design parameters of this implementation. Hence, a different design is required if any of these parameters are changed. The implementation of

this lens based BFN requires realization of different length transmission lines that can be a challenge for certain technologies such as substrate integrated waveguides (SIWs). However, a novel planar Luneburg lens based BFN does not have these limitations. The beam can be steered by merely changing the feed position. Furthermore, the number of radiating elements excited by the lens can be controlled by changing the lens diameter. Hence, a single lens design can be used to realize multibeam antennas, each having its own half-power beamwidth (HPBW). The size of the Luneburg lens based BFN is also compact in comparison with the other quasi-optics based BFN. This factor is particularly important for antennas in millimeter wave range as the substrate loss is significantly high in this band [94]. The proposed BFN is also wideband due to its transverse electromagnetic (TEM) mode.

A sufficient effective refractive index variation is required to implement a Luneburg lens. In the literature, several techniques are proposed for its implementation. In [95], dielectric disks placed along the two walls of a parallel plate waveguide are machined to achieve the Luneburg lens refractive index profile. Instead of placing shaped dielectric discs inside a parallel plate waveguide, the distance between the waveguide plates is varied in [96] to change the waveguide refractive index. A traditional Luneburg lens refractive index profile requires curved surfaces to implement the lens. A flat lens is realized by using Transformation Optics to modify this refractive index profile in [97]. Variation in dielectric foam density can also change the refractive index to realize a lens, as presented in [98, 99]. Different height metal posts in a parallel plate waveguide, arranged in a square lattice, can also be used to implement a lens as described in [100]. Metal or dielectric machining is required in these techniques to implement a lens.

Patterns printed on a substrate can also change the effective refractive index. Crosses of printed microstrip lines, straight and meandered, are used to realize a lens in [101]. Lens based on hexagonal patches on a substrate is presented in [102]. Printed rings based metamaterial, placed inside a parallel plate waveguide is used to implement a lens in [103]. A substrate with printed circular patches of varying diameter is placed in a parallel plate waveguide in [104] for lens realization. All the printed lens implementation are in X- and Ku-band with quite fine printing patterns. Because of the complex precess and machining involved, fabrication of these lens implementations can be quite challenging in millimeter wave frequency range.

Hole density variation in a dielectric material can be used to control its effective refractive index. Changing hole density in a dielectric material placed inside a parallel plate waveguide followed by the material shaping is used to realize a lens in [105]. Lens implementation using holes in the lens core followed by two layers of different dielectric materials, placed in a parallel plate waveguide, is presented in [106]. Both implementations require machining and drilling

of the dielectric materials. Plated vias in a substrate are used to realize concentric rings of only three refractive indices to implement a crude lens in [107]. However this technique has limited refractive index flexibility and bandwidth due to TE_{10} mode of operation.

A low-cost, printed circuit board (PCB) process based W-band Luneburg lens is proposed in this work. This implementation is based on nonplated vias in a substrate. The via diameter is controlled to change the refractive index of the material. A parallel plate structure can be realized by covering these holes on both sides with metal sheets. A high dielectric constant substrate disk is further inserted in the lens core to extend the realizable refractive index variation, necessary to implement a lens.

7.2 Antenna structure

7.2.1 Lens Design

If the background media is air, Luneburg lens effective refractive index profile is given by the following equation:

$$n_{eff} = \sqrt{2 - r^2} \tag{7.1}$$

where r is normalized lens radius. For a lens submerged in some dielectric medium, a multiplying factor is required at the left hand side of the above equation. In either case, this equation shows that an effective refractive index contrast of $\sqrt{2}$ is required to realize the lens.

Controlling lower dielectric constant discontinuities in a high dielectric constant material can provide a variation in the material effective refractive index. This has been demonstrated practically in [105]. Thus, periodic holes in a substrate, covered by metal cladding can also provide refractive index variation with changes in the hole diameter. Such a periodic structure can be analyzed by performing eigenmode analysis on a unit cell (UC) shown in Figure 7.1. The UC consists of a dielectric cuboid with a hole at its center. Master-slave boundary conditions implement a periodic structure in XY-plane with periodicity a. Perfect electric conductor boundary conditions are assigned in planes $Z = 0$ and $Z = t$ to simulate a dielectric with a hole inside a parallel plate waveguide.

The eigenmode analysis is performed using HFSS-Ansys. In this analysis, the frequencies supported by the UC are determined by varying the phase along Y-axis. Due to the square structure and circular hole, the UC behaviour has 4-fold rotational symmetry in XY-plane. The phase P_y and frequency of the UC are related to the effective refractive index by the

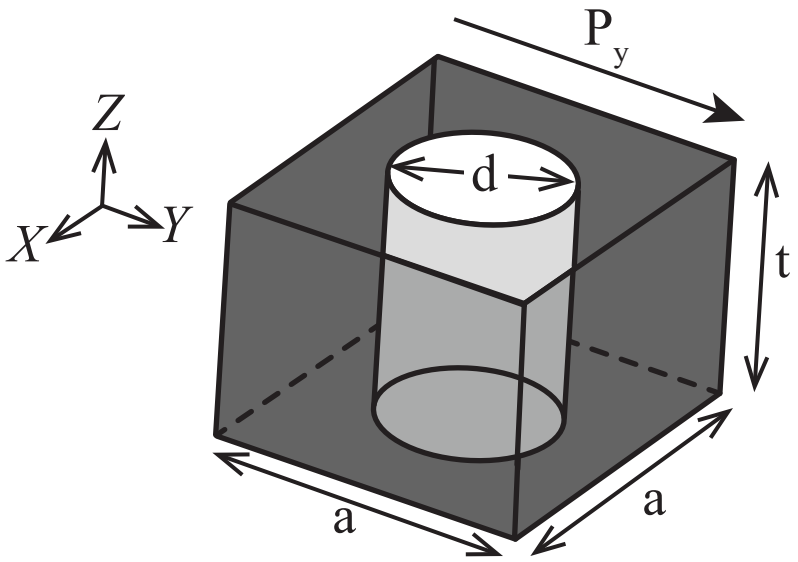

Figure 7.1 Unit cell for Luneburg lens.

following equation:

$$P_y = \frac{2\pi f n_{eff} a}{c} \tag{7.2}$$

According to Equation 7.1, a contrast of $\sqrt{2}$ for effective refractive index is required to implement a Luneburg lens. In the proposed UC, substrates with different dielectric constants can be examined with varying hole diameters to achieve this contrast. For the lens designed in this work, two different substrates are used for this purpose. For the design frequency of 77 GHz, a high dielectric constant substrate RO4350B with $\epsilon_{\mathrm{r}} = 3.66$ from Roger Corporation is proposed for the lens core. The outer region of the lens can be constructed with RT/Duroid 6002 with $\epsilon_{\mathrm{r}} = 2.94$. The holes diameter can be gradually increased from the center to the outer region for both substrates to realize a graded refractive index profile. The periodicity a in XY-plane is 0.63 mm and 0.76 mm for RO4350B and RT/Duroid 6002, respectively. The lens is designed to operate in quasi-TEM mode for wideband operation. Quasi-TEM mode in a parallel plate waveguide can be achieved by limiting the distance between the plates to $\lambda_{\mathrm{g}}/2$ where λ_{g} is the shortest guided wavelength inside the parallel plate waveguide. For the proposed design, substrates with thickness (t) of 0.508 mm are proposed. This thickness is equal to $0.25\lambda_{\mathrm{g}}$ (shortest λ_g=2.04 mm) for the design frequency of 77 GHz. The values of effective refractive index for the two substrates with different hole diameters are shown in Figure 7.2. At 77 GHz, the two substrates cover the effective refractive index range from 1.91 to 1.48, providing the effective refractive index contrast of 1.29. This is less than $\sqrt{2}$,

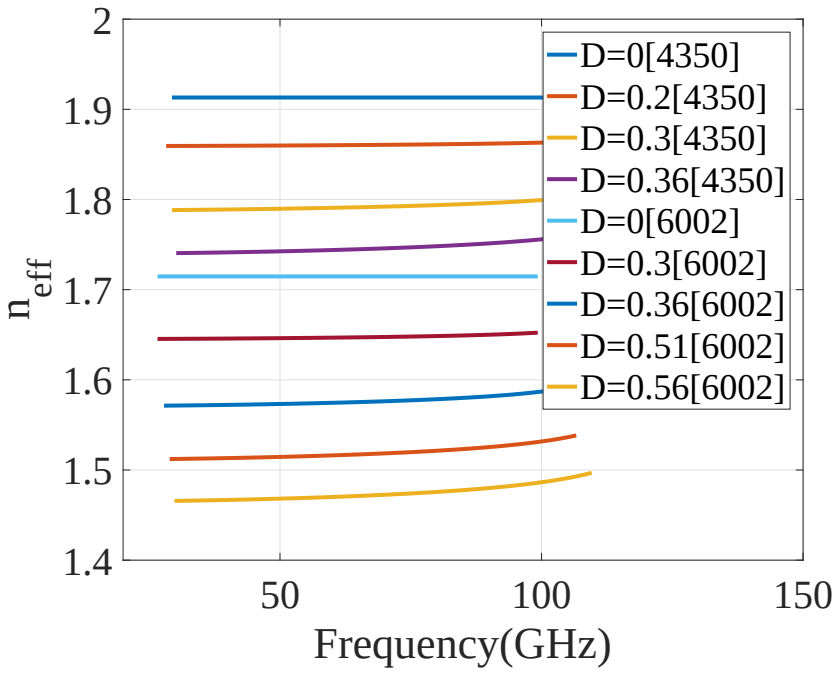

Figure 7.2 Effective refractive index variation for the two substrates with different drill diameters (in mm) for RO4350B (a=0.63mm) and RT/Duroid 6002 (a=0.76mm).

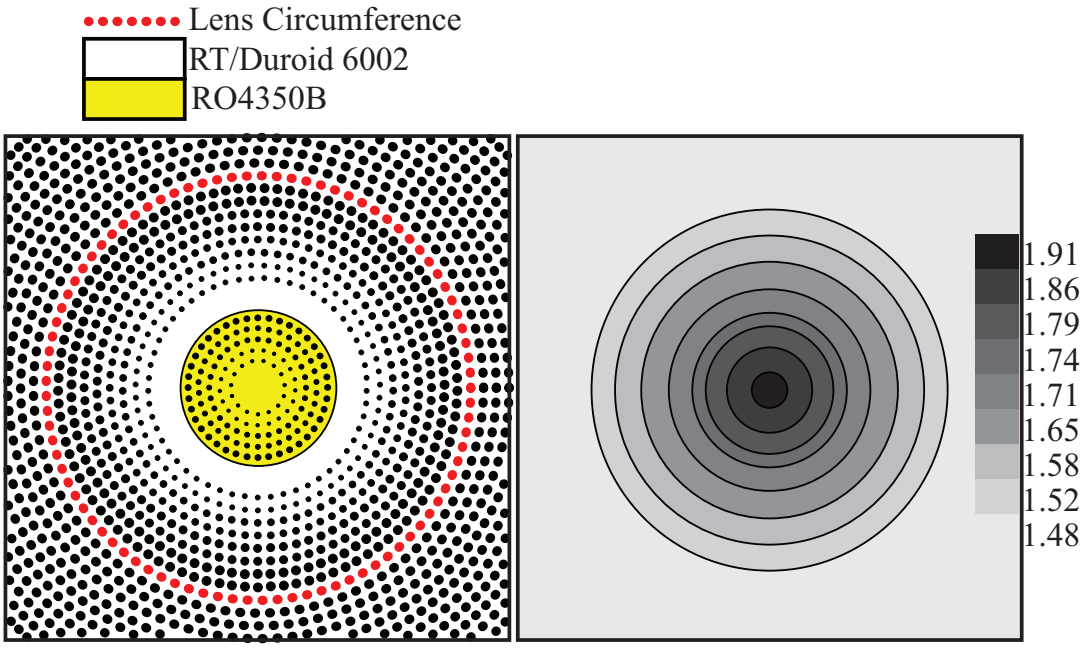

Figure 7.3 Lens structure (left) with effective refractive index distribution (right).

Table 7.1 Dimensions for concentric rings of drills with effective refractive index value

Substrate	Radius (mm)	Drill Diameter (mm)	n_{eff}
4350B	0.63	0	1.91
4350B	2×0.63	0	1.91
4350B	3×0.63	0.2	1.86
4350B	4×0.63	0.2	1.86
4350B	5×0.63	0.3	1.79
4350B	6×0.63	0.3	1.79
4350B	7×0.63	0.36	1.74
6002	7×0.63+0.76	0	1.71
6002	7×0.63+2×0.76	0	1.71
6002	7×0.63+3×0.76	0.3	1.65
6002	7×0.63+4×0.76	0.3	1.65
6002	7×0.63+5×0.76	0.43	1.58
6002	7×0.63+6×0.76	0.43	1.58
6002	7×0.63+7×0.76	0.51	1.52
6002	7×0.63+8×0.76	0.51	1.52
6002	7×0.63+9×0.76	0.56	1.47
6002	7×0.63+10×0.76	0.56	1.47

required for the Luneberg condition, but it is sufficient to implement a lens [99]. The hole diameter varies from $0.09\lambda_g$ to $0.25\lambda_g$ to achieve this contrast. Constant values of effective refractive indices with respect to frequency predict wideband operation of the proposed lens due to its quasi-TEM mode.

Concentric circles of holes in substrates can realize circularly symmetric graded effective refractive index to implement the lens as shown in Figure 7.3. Due to the symmetry of the proposed UC, this circular lattice is expected to provide the same effective refractive indices as predicted by the eigenmode analysis with square lattice. The radii of the concentric circles are multiple of the periodicity constant a. Moreover, the center-to-center distance between the holes in one circle is also approximately equal to a. This satisfies the periodicity criteria used in the eigenmode analysis. A Luneburg lens with diameter of 24.5 mm was realized using the concentric circles of holes with varying diameters. The circle radii, hole diameter and value of resulting effective refractive index are given in Table 7.1 for this lens. The lens diameter can easily be reduced by removing some of the concentric circles of holes provided that the whole effective refractive index range is covered.

SIW lines are using to launch the cylindrical wave at the circumference of the designed lens. Conversion of this incident wave to a planar equiphase wave can be observed in Figure 7.4

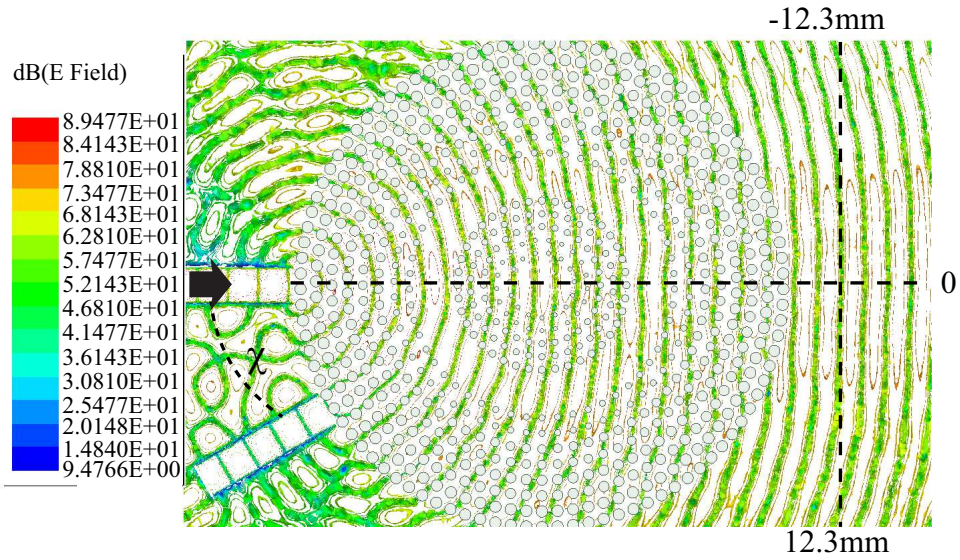

(a)

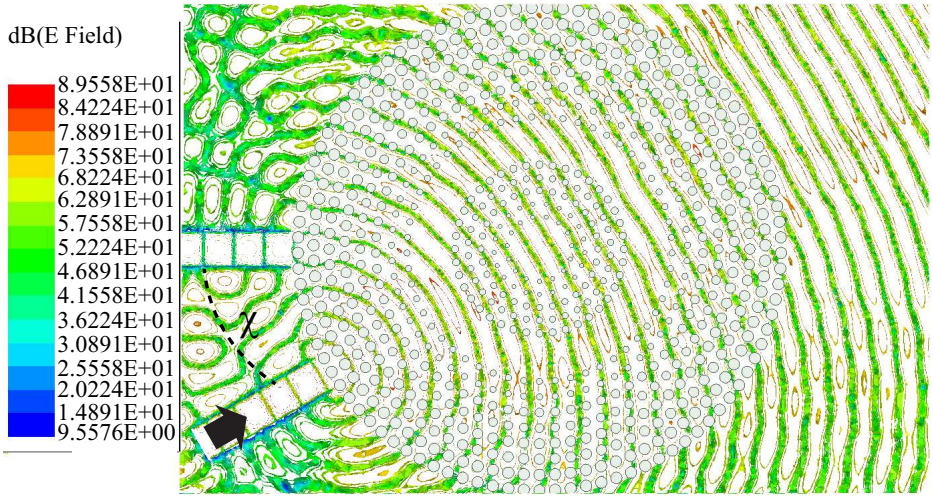

(b)

Figure 7.4 Lens focusing at, (a) $\chi = 0^{o}$, (b) $\chi = 30^{o}$.

where electric field distributions are presented. These distributions can be used to realize a BFN, exciting a phased array with a progressive phase necessary to steer the radiated beam.

The phase plane can be inclined by rotating the excitation SIW along the lens circumference because of its circular symmetry as shown in Figure 7.4(b). The magnitude distribution along an equiphase plane, shown with dotted vertical line in Figure 7.4(a), is presented in Figure 7.5 with respect to the lens diameter. A maxima can be observed in this distribution, inline with the feeding SIW through the lens center. An amplitude tapering can be observed around this maxima. The tapering rate can be controlled with the lens diameter. For the lens designed in this work, the diameter is selected such that a 6 dB tapering covers a distance equal to

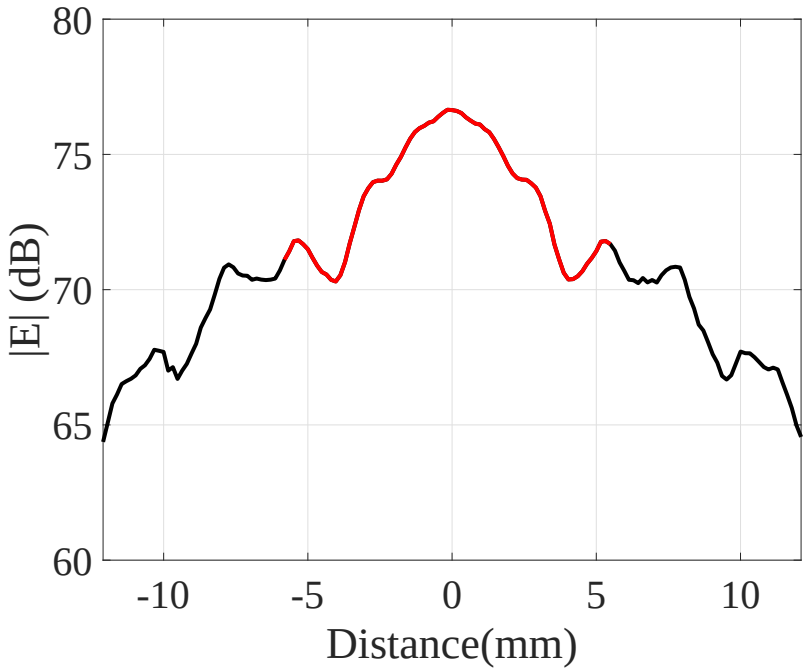

Figure 7.5 Electric field magnitude along an equiphase plane with respect to the lens diameter (lens center as reference).

seven adjacent radiating elements included within the range depicted in red in Figure 7.5. A BFN can be realized by introducing antenna ports in this region, exciting seven phased array elements. Reducing the lens diameter is expected to shrink this region, reducing the number of radiating elements excited by the lens, hence, and increasing the HPBW of the phased array. For the designed lens, the electric field magnitude drops sharply beyond the seven radiating elements. This results in a negligible relative excitation of the adjacent array elements.

The effective refractive index at the lens circumference is 1.48 and the lens is submerged in a parallel plate sructure with effective refractive index of 1.71. Therefore, there is a effective refractive index discontinuity at the lens circumference which causes refraction at this discontinuity. The outer most hole circle of the proposed lens can thus be extended beyond the lens circumference to avoid this diffraction as shown in Figure 7.3.

7.2.2 BFN and Multibeam Antenna Structure

Antenna ports and beam ports can be introduced in this lens structure to realize a BFN as shown in Figure 7.6. The effective refractive index at the lens circumference is extended to cover the antenna ports by drilling holes of diameter equal to the hole diameter of the outer

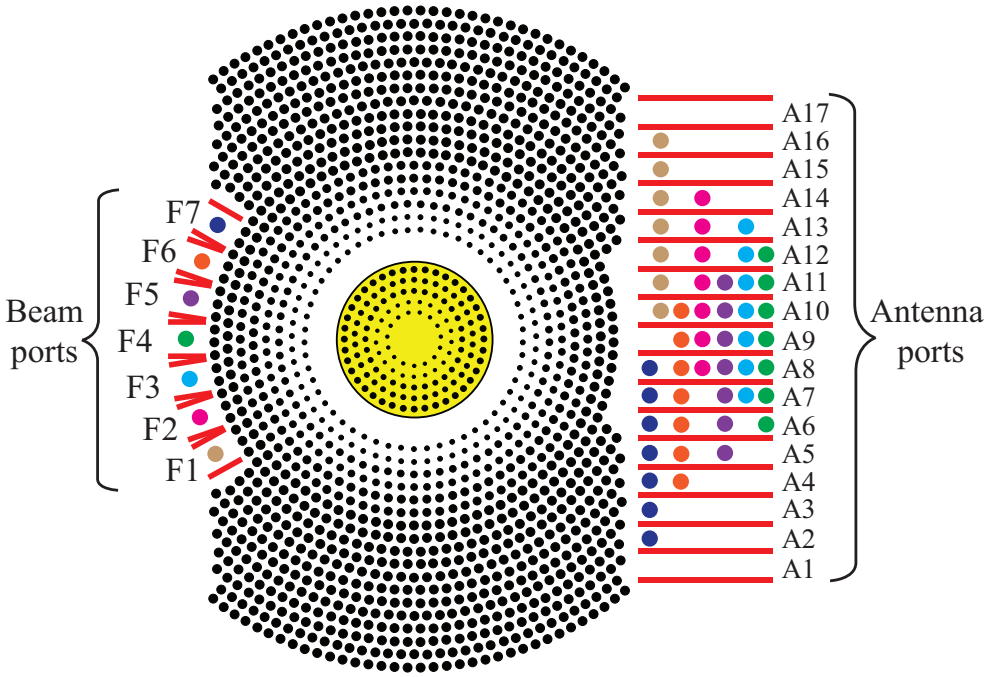

Figure 7.6 BFN comprised of a lens with beam ports and antenna ports.

most concentric hole circle. This helps to avoid the parasitic field due to refraction that can excite unwanted antenna ports. The antenna and beam ports are SIWs. The beam ports are placed radially along the lens circumference. Each beam port generates equiphase planar wave exciting a set of antenna ports identified in Figure 7.6 with color circles. The inclination of the equiphase plane due to rotation of the beam port along the lens circumference excites the antenna ports with a progressive phase to steer the radiated beam. The progressive phase slope depends on the relative position of the antenna and beam ports. The SIWs of the antenna ports have shared walls. This helps to reduce interelement distance between the antenna ports to achieve wide angle beam steering.

In order to evaluate the designed BFN, magnitudes and phases at the antenna ports are used to constitute an array factor (AF) for different beam ports. Two AFs for different diameter lens are shown in Figure 7.7. The AF for 24.6 mm diameter lens, excited by SIW feeds at $\chi = 0^o, \pm 10^o, \pm 20^o, \pm 30^o$ shows 17° of broadside HPBW, -11.4 dB worst case SLL and about $\pm 43^o$ of beam steering. The steering angles (θ_{out}) of the seven main beams are 0, $\pm 14^o$, $\pm 28^o$ and $\pm 43^o$, which are in good agreement with expectations from the refraction angle predicted by Snell's law at the air-dielectric interface (i.e. $1.48 sin(\chi) = sin(\theta_{out})$). For a smaller lens of diameter = 10.16mm exciting the same antenna ports at $\chi = 0^o, \pm 20^o, \pm 40^o$, the broadside HPBW is 30°. The worst case SLL and beam steering angles for this case are 12.5 dB and $\pm 60^o$, respectively. Hence, by using the same lens with different diameters, we can design

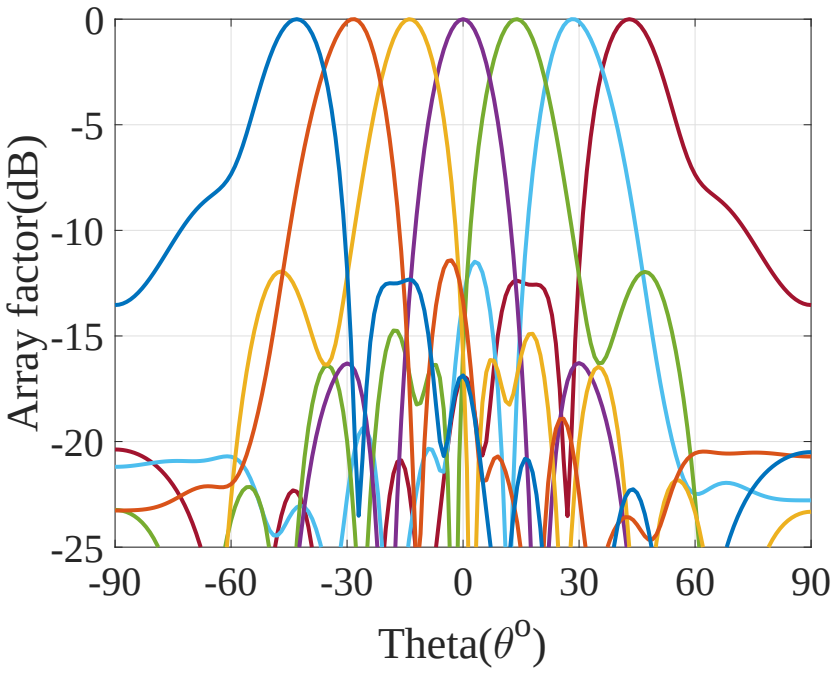

(a)

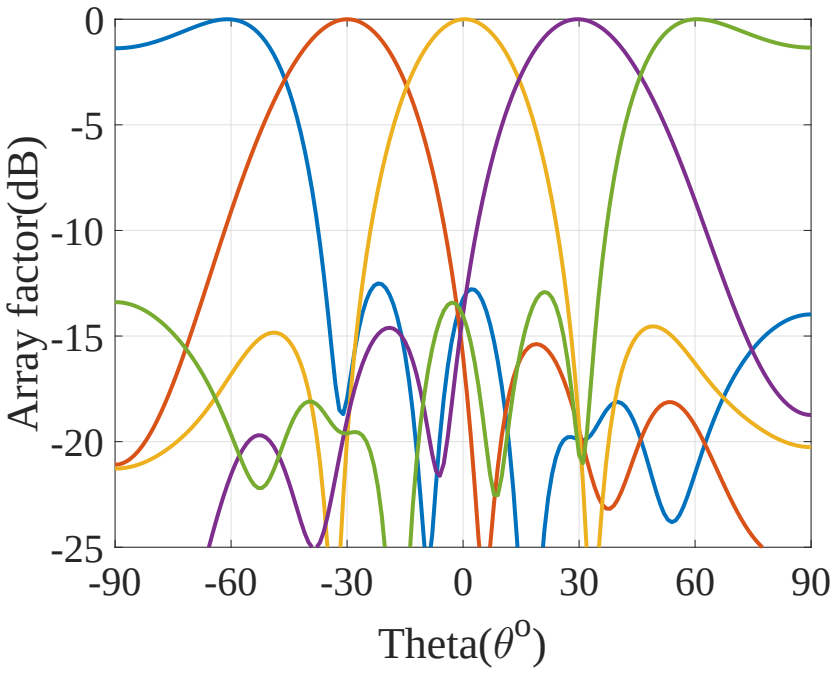

(b)

Figure 7.7 Array factor constituted by the proposed BFN with Luneburg lens diameter of (a)24.6 mm (b) 10.16 mm.

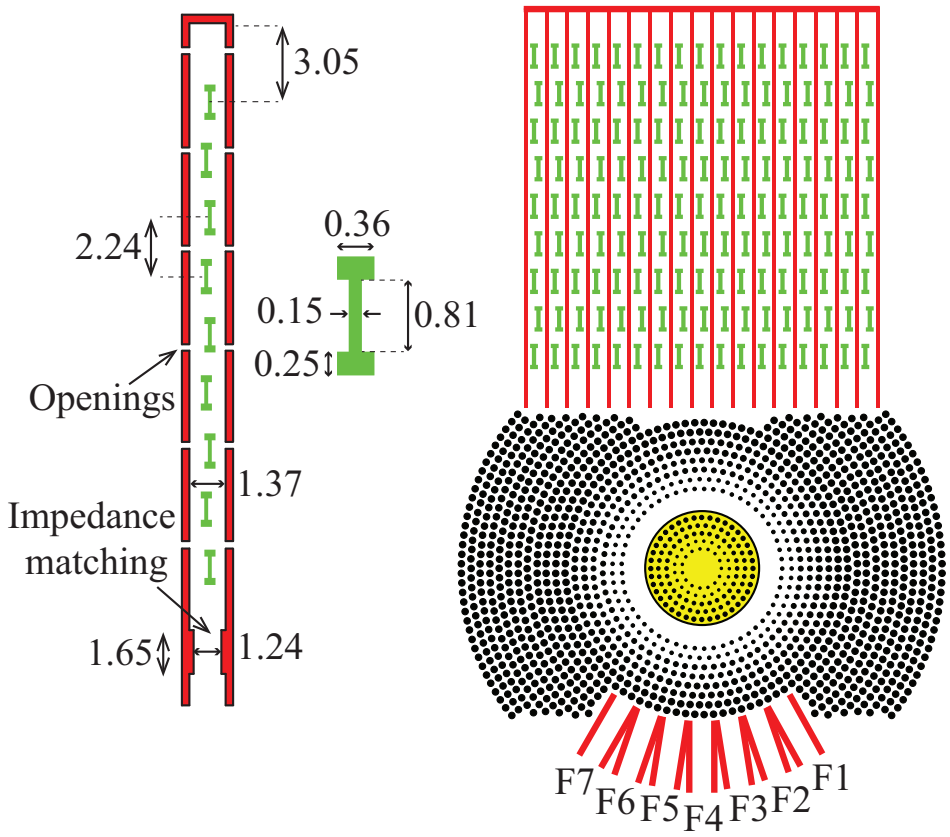

Figure 7.8 Radiating element (left) and multibeam antenna structure (right) (dimensions in mm).

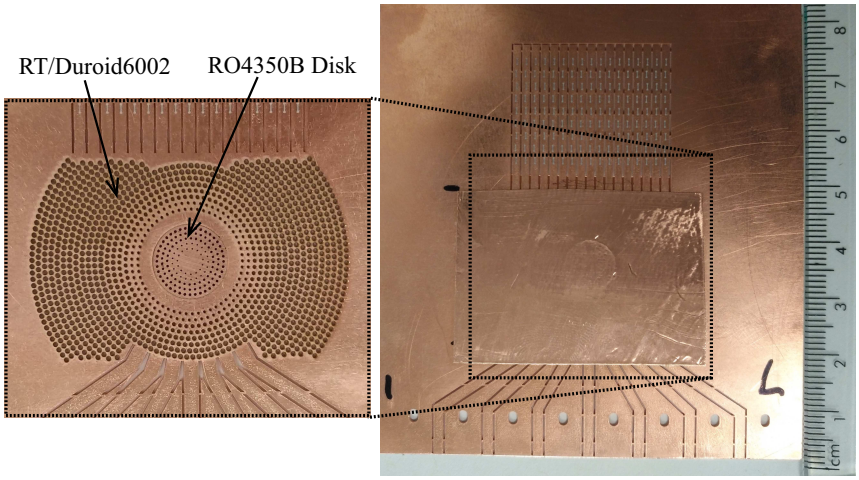

Figure 7.9 Fabricated prototype.

different multibeam antennas, each having different broadside HPBW.

Radiating elements can be integrated at the antenna ports to implement a multibeam antenna

as shown in Fig. 7.8. The radiating element (left in Fig. 7.8) is a series fed slot array on an SIW. This type of arrays is well known in the literature [87, 90]. Different slot and SIW dimensions are also given in this figure. In total, seventeen array ports are used in this structure with interelement spacing of 1.68 mm (0.43λ at 77 GHz). The multibeam antenna is characterized with the help of simulations and measurements of a fabricated prototype in the following section.

7.3 Experimental Validation

A radiating element and multibeam antenna with Luneburg lens based BFN were fabricated to validate the proposed design using a low-cost PCB fabrication process was used. The metallic SIW walls of the beam ports and radiating elements were realized by laser machining through RT/Duroid 6002 substrate and electroplating the resulting slots. The radiating slots were realized by chemically etching the top coper cladding of the substrate, treated with a photosensitive mask. The lens core was realized with an RO4350B substrate disk inserted in a circular opening of 4.6 mm radius created in RT/Duroid 6002 as shown in Figure 7.9. The graded refractive index was realized by introducing hole circles with increasing hole diameter as we move away from the lens center for both of the substrates. These holes were covered with copper tape on both sides to realize the parallel plate waveguide.

The radiating element is characterized in Figure 7.10. The measured and simulated S parameters, shown in Figure 7.10(a), exhibit a 1.6 GHz (78.6-80.2 GHz) -10 dB bandwidth for the measured S_{11}. A transition is used to connect the SIW antenna feed to WR-10 VNA port [94]. A frequency band upshift of about 3% is observed in the fabricated prototype. A possible cause of this variation can be a material dielectric constant variation in W-band. Radiation patterns for the two principal planes of this radiating element are shwon in Figure 7.10(b). HPBW of 10^o is observed in the plane parallel to the array axis (H-plane) and a wide HPBW is observed in E-plane. This is the beam steering plane and the wide FoV in this plane helps to achieve beam steering at wide angles without losing the gain due to the element factor in the proposed multibeam antenna.

Measured port reflections for the prototyped multibeam antenna beam ports are presented in Figure 7.11. For reflection measurement of one port, the other ports were left open due to unavailability of matched loads in SIW technology. However, these measured reflections are expected to closely represent the real reflection coefficients as the minimum simulated isolation between two adjacent ports is 21.4 dB at the design frequency.

The simulated radiation patterns for the multibeam antenna are shown in Figure 7.12. Dif-

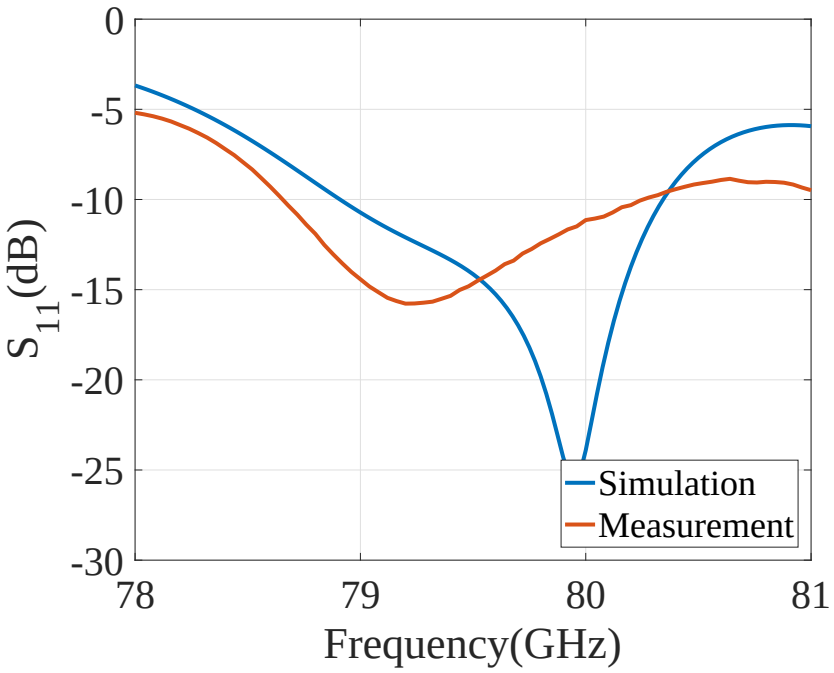

(a)

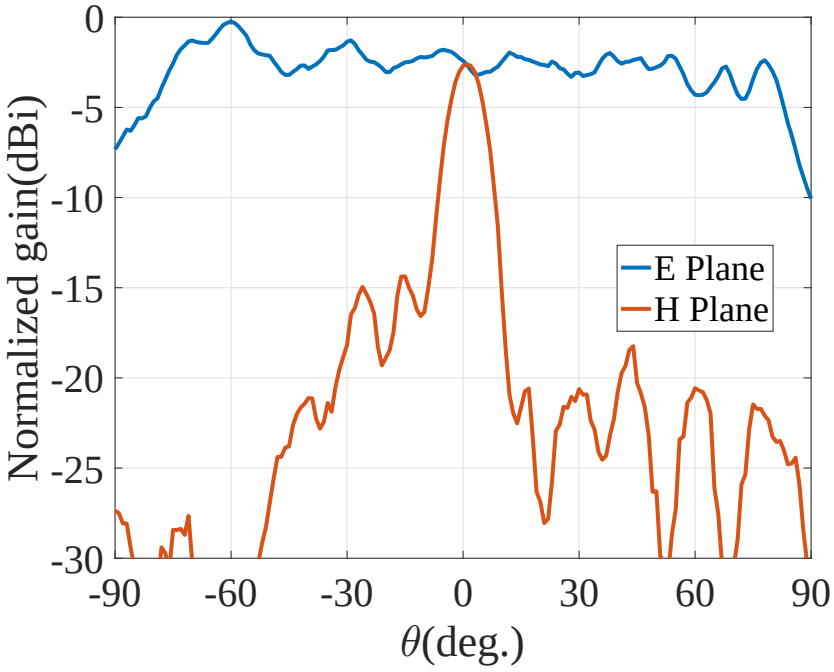

(b)

Figure 7.10 Measurement results for single one-dimensional array (a) S parameters (b) Principal plane radiation patterns.

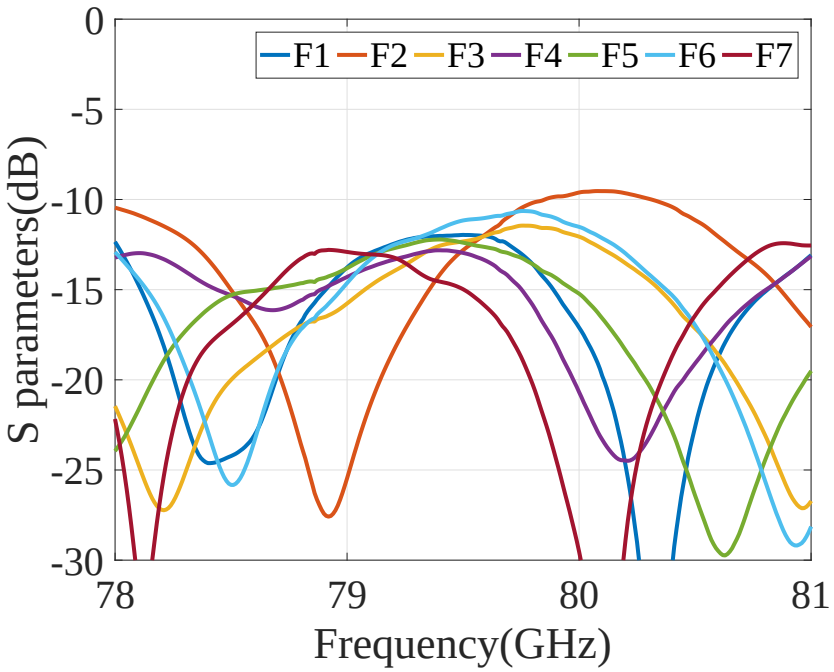

Figure 7.11 Port reflections for the fabricated prototype.

ferent angle beam steering can be observed in E-plane by exciting the antenna from F1 to F4 (The radiation pattern is symmetric for the rest of the beam ports due to symmetry of the structure). Simulated and measured E-plane radiation patterns are shown in Figure 7.13. The beam steering angles for the measured radiation patterns are -42^o, -31^o, -16^o, -4^o, 12^o, 26^o and 41^o for F1 to F7, respectively with $\chi = 0^o, \pm 10^o, \pm 20^o, \pm 30^o$. The HPBW of the measured radiation patterns are 10^o for broadside and 13^o for $\approx \pm 41^o$ steer angles. The measured HPBWs are about 4^o narrower as compared to the simulated ones. Slight defocusing of the fabricated lens due to the fabrication tolerances and material characteristics variations in W-band can expand the red region in Fig. 7.5, exciting additional radiating elements. This effect can contribute to this measurement discrepancy. The measured SLL are 10.4 dB, 9.7 dB, 9 dB, 11 dB, 10.2 dB, 9.9 dB and 7.7 dB for F1 to F7, respectively. Higher SLLs for certain beams support the defocusing in the fabricated prototype. The measured radiation patterns beam steering angle approximately correspond to the simulated values. The simulated radiation efficiencies vary from 63% for broadside radiation to 54% for $\pm 43^o$ beam steering. The simulated gain in the broadside is 18.7 dB which is 6.4 dB higher than the measured gain. This loss is comparable to one- and two-dimensional arrays presented in Chapter 4. This loss can mainly be attributed to high substrate tangent loss in W-band [94].

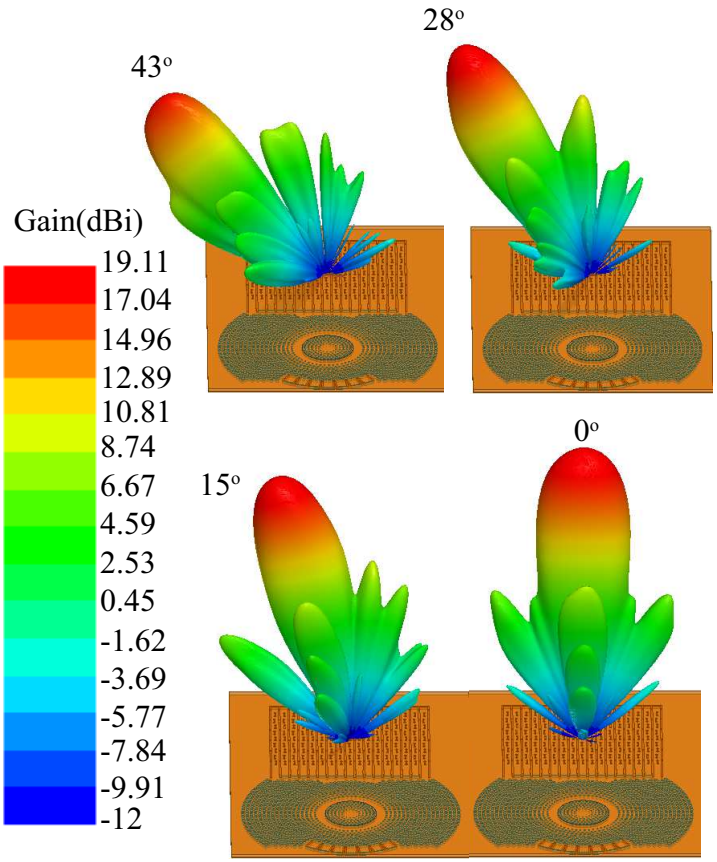

Figure 7.12 Simulated polar plots of multibeam antenna for F1 (top left) to F4 (bottom right).

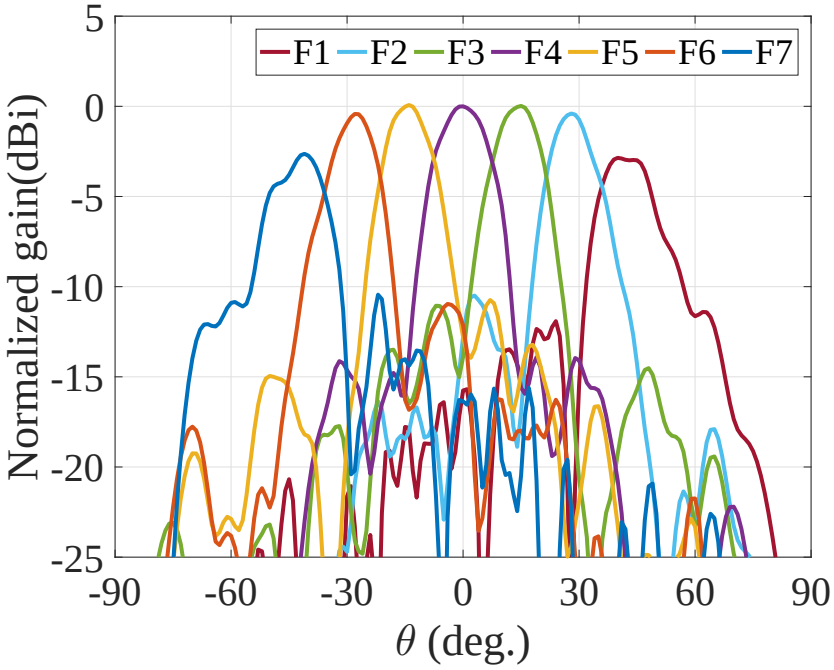

(a)

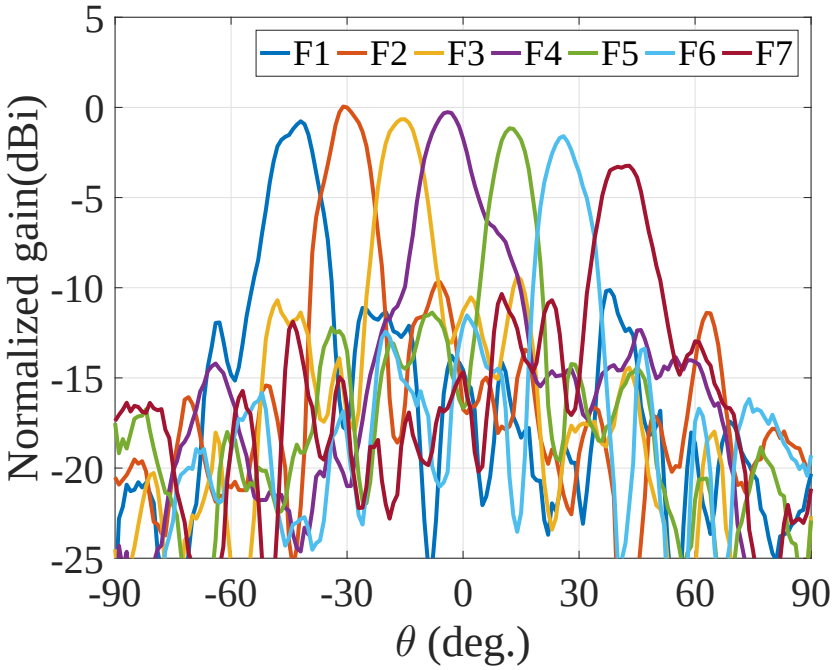

(b)

Figure 7.13 Beam steering of the proposed antenna structure (a) Simulations (b) Measurements.

7.4 Conclusions

A PCB process based single substrate layer wideband Luneburg lens implementation is presented in this chapter. This lens is used to propose a novel BFN to realize a multibeam antenna. The Luneburg lens implementation is based on an effective refractive index variation realized with changing the hole diameters in a dielectric material placed inside a parallel plate waveguide. This structure is realized by drilling holes in a substrate and covering these hole on both side by metal sheet. The required effective refractive index variation is achieved by inserting a higher dielectric constant substrate disc inside a low dielectric constant substrate. Concentric circles of holes with increasing hole diameter are used to achieve effective refractive index profile of the Luneburg lens. TEM mode of operation of the proposed lens predicts a wideband operation. A BFN is realized by adding beam and antenna ports to the designed Luneburg lens. A wide angle beam steering multibeam antenna is designed and prototyped using the proposed BFN, providing approximately $\pm 41^{o}$ beam steering in the measurements. The proposed multibeam antenna provides a design flexibility for HPBW and beam steering angles in comparison to the other BFNs available in the literature. Good agreement of the measured beam steering angles and SLLs with the simulation results validate the proposed Luneburg lens based BFN.

CHAPTER 8 CONCLUSION AND FUTURE WORK

This chapter summarizes the work presented in this dissertation and outlines its possible future extensions.

8.1 Summary

This work proposes a collision avoidance system featuring a super-resolution based target localization and realizes its radiation subsystem. Current state-of-the-art automotive radar is categorized into short range radar (SRR) and long range radar (LRR). SRR covers a wide field of view (FoV) of 120^o in azimuth plane for the range of approximately 50 m. It consists of multiple sensors transmitting picosecond range pulses to calculate the distances from the target. The distance estimated at each sensor is then used to triangulate the target to determine its location. The angular resolution of this system is limited by the pulse width of the transmitted signal. A precise synchronization is required between the sensors in SRR to accurately localize the target. Moreover, pulse based systems are inherently short range. For adaptive intelligent cruise control, LRR uses continuous wave sensor in a narrow FoV ($\approx 18^o$) for approximately 200 m range. Narrow beam antennas scan this FoV to localize the target with angular resolution equal to the beamwidth of the transmit antenna. This system has limited FoV due to high gain transmit antenna.

This work aims to simplify this collision avoidance system which can result in a low-cost and widely useable system. It is done by proposing super-resolution based target localization. Hence, we can combine LRR and SRR and simplify the system hardware at a cost of computationally expensive localization method. The proposed system doesn't require beam scanning, and uses continuous wave transceiver and low gain antennas to cover a wide FoV.

However, super-resolution based localization requires point-source targets and it is sensitive to the signal to noise ratio of the signal reflected by the target. These two characteristics make it challenging to imply super-resolution algorithm for collision avoidance application as the automotive targets are extended targets for automotive radar due to their close range. To overcome these issues it is proposed to introduce a target radar cross-section enhancing tag. This tag can introduce modulation in the reflected signal to enhance its visibility. We used polarization modulation (rotation of the reflected linear polarization by 90^o with respect to the incident polarization) and amplitude modulation (switching the reflected signal on and off) for the tag developed in this work.

ESPRIT algorithm was selected for this work after studying the properties of classical super-resolution algorithms. A MATLAB simulation for ESPRIT algorithm was established to develop the architecture of the proposed the system. The simulation revealed that the efficiency of the ESPRIT algorithm can be improved by dividing the system FoV into small sectors using a multibeam transmit antenna as discussed in Chapter 3. Hence, the proposed system uses a tag to enhance the target visibility and sectors the radar FoV into smaller segments using a multibeam transmit antenna.

A RCS enhancing tag was designed at 77 GHz using novel radiating elements proposed to achieve the design constraints of polarization diversity and wide FoV. Introduced in Chapter 4, the radiating elements exploit the properties of SIW and rectangular waveguide cavity to realize a compact structure with polarization diversity. One- and two-dimensional arrays of this radiating element were designed and fabricated for two orthogonal polarizations to validate the bandwidth, polarization and FoV characteristics specified for the proposed tag. However, these arrays exhibit narrow impedance bandwidth due to small size and resonant nature of the radiating elements. Additionally, the fabricated prototypes are lossy in comparison with the simulation models due to high material losses in W-band. One-dimensional arrays were arranged in a Van-Atta array configuration to implement a polarization rotating tag with retroreflection property as discussed in Chapter 6. A setup and measuring procedure were established to measure monostatic and bistatic RCS of the fabricated tag prototypes. The tag exhibited 9^o elevation FoV and 120^o azimuth retroreflection FoV. The reflected signal had its linear polarization plane rotated by 90^o with respect to that of the incident signal polarization. RCS enhancement of at least 15 dB was measured as compared to the reflections from a flat aluminium plate due to retroreflection. Fabrication tolerances were also investigated by comparing the measured and simulated results. Though the tag is designed to have FoV of 120^o, a sharp drop of the tag broadside monostatic RCS beyond $\pm$50^o is observed due to the unit radiating elements radiation patterns.

Amplitude modulation was achieved by a novel switch proposed for SIW technology presented in Chapter 5. This switch relies on the high impedance of a resonant slot, placed perpendicular to the SIW axis, that can be switched to non-resonant state by coupling the slot with a PIN diode. A fully functional switch was implemented in K-band to validate this concept. A hardwired switch, where a short-circuit at the middle of the slot was used to emulate a forward biased PIN diode, was implemented in the proposed tag due to the lack of commercially available PIN diode in W-band. Amplitude variation of about 15 dB was measured with this switch in the fabricated prototypes.

Sectoring of the radar FoV was achieved by using a novel multibeam antenna designed at

77 GHz as detailed in Chapter 7. This antenna is a phased array, fed by a Luneburg lens based BFN. Each element of this phased array is a one-dimensional slot array on an SIW. The Luneburg lens in the BFN excites a subset of the phased array elements with amplitudes and phases determined by the excitation port placed along the lens circumference. A low-cost single substrate layer implementation using a PCB process was used to fabricate the lens. Beam steering of approximately 82° ($\approx \pm 41°$) was measured for the fabricated prototype of a seven-beam antenna implemented using the proposed BFN. However, just like the arrays and tag, the multibeam antenna prototype also exhibited high loss in measurements.

8.2 Limitations and Future Work

The radiation subsystem of a proposed collision avoidance radar using super-resolution based target localization is developed in this dissertation. However, the components conceived in this thesis exhibit certain limitations that can further be improved. Below is a list of some limitations and their possible solutions.

- Though the proposed radiating element for arrays and tag provides wide-angle beamforming capacity and polarization diversity, the impedance bandwidth is quite small. It is due to high quality factor of the cavity placed inbetween the coupling and radiating slots as explained in Chapter 4. This bandwidth can be improved by lowering the quality factor of the cavity while maintaining the dimensions constraints of the radiating elements.

- The tag is designed to have grating lobes suppressed under -10 dB for broadside FoV of 120°. However, the measured and simulated RCS is limited to about 100° due to the limited radiation patterns of its radiating elements. The radiation pattern FoV could be widened by introducing a dielectric layer on the top of the radiating slots [108].

- The measured impedance bandwidths of the fabricated prototypes are upshifted as compared to the simulation models. The dielectric constant variation is expected to be the reason of this discrepancy. The substrate dielectric constant can be measured in W-band before redesigning the structure to eliminate this frequency variation.

- The measured antenna gains are significantly lower than the simulated ones. It is possibly due to high loss tangent of the material in W-band. Material loss tangent can be meassured in W-band to validate this assumption.

- The proposed switch concept is validated in K-band due to inaccessibility of a PIN diode in W-band. W-band PIN diode has previously appeared in the literature [109],

[110], however, the diode is not commercially available. A functional switch in W-band can be designed.

In addition to the improvements in the designed components, some supplementary work can be suggested for the proposed system. It is a complex system and requires antenna and system design, automotive radar channel estimation and signal processing for proper implementation. This dissertation only targets the radiating subsystem. The measured characteristics of the designed components in this work can be used to further develop the proposed system. Below are some possible extensions.

- Development of the modulation signals, orthogonal to one another.
- Link budget analysis.
- Radar system front end design.
- Baseband signal processing.
- Performance analysis of the proposed system

8.3 Publications and Manuscripts

8.3.1 Journals

- A. B. Numan, J. F. Frigon and J. J. Laurin, "Single-Pole Single-Throw Switch for Substrate-Integrated Waveguide," in *IEEE Microwave and Wireless Components Letters*, vol. 28, no. 3, pp. 221-223, March 2018.
- A. B. Numan, Jean-François Frigon and Jean-Jacques Laurin, "W-band compact slot antenna arrays with polarization flexibility," Submitted minor revision to *Radio Science*, February 2018.
- A. B. Numan, Jean-François Frigon and Jean-Jacques Laurin, "Radar cross-section enhancing tag with polarization diversity and scattering modulation," Submitted to *IEEE Transactions on Antennas and Propagation*, February 2018.
- A. B. Numan, Jean-François Frigon and Jean-Jacques Laurin, "Printed multibeam antenna with Luneburg lens-based beamforming network," Submitted to *IEEE Transactions on Antennas and Propagation*, March 2018.

8.3.2 Conferences

- A. B. Numan, Jean-François Frigon and Jean-Jacques Laurin, "Printed W-band Luneburg lens for beamforming applications", Accepted *APS/URSI*, Boston, MA, July 2018.
- A. B. Numan, Jean-François Frigon and Jean-Jacques Laurin, "Compact W-band antenna for polarization diversity applications", *URSI GASS*, Montreal, Canada, August 2017.
- A. B. Numan, Jean-François Frigon and Jean-Jacques Laurin, "W-band slot antenna array for wide-angle phase scan and polarization flexibility", *IEEE AP-S/URSI*, Fajardo, Puerto Rico, June 2016.
- A. B. Numan, Jean-François Frigon and Jean-Jacques Laurin, "Millimeter wave orthogonally polarized substrate integrated waveguide slot antenna arrays", *GSMM*, Montreal, Canada, June 2015.

REFERENCES

[1] I. Gresham, A. Jenkins, R. Egri, C. Eswarappa, N. Kinayman, N. Jain, R. Anderson, F. Kolak, R. Wohlert, S. Bawell, J. Bennett, and J. Lanteri, "Ultra-wideband radar sensors for short-range vehicular applications," *IEEE Transactions on Microwave Theory and Techniques*, vol. 52, pp. 2105–2122, Sept 2004.

[2] H. H. Meinel and J. Dickmann, "Automotive radar: From its origins to future directions," *Microwave Journal*, vol. 56, pp. 24–40, September 2013.

[3] J. Davis, "Radar system for headway control of a vehicle," Apr. 10 1990, uS Patent 4,916,450. [Online]. Available: http://www.google.ca/patents/US4916450

[4] J. Wenger, "Automotive mm-wave radar: status and trends in system design and technology," in *IEE Colloquium on Automotive Radar and Navigation Techniques*, Feb 1998, pp. 1/1–1/7.

[5] H. H. Meinel, "Millimeterwaves for automotive applications," in *European Microwave Conference*, vol. 2, Sept 1996, pp. 830–835.

[6] S.Zeng and J. N. Nickolaou, "Chapter 9: Automotive radar," in *Small and Short-Range Radar Systems*, G. L. Charvat, Ed. Boca Raton: CRC Press, 2014.

[7] F. Folster and H. Rohling, "Signal processing structure for automotive radar," *Frequenz*, vol. 60, pp. 20–23, 2006.

[8] M. Murad, J. Nickolaou, G. Raz, J. Colburn, and K. Geary, "Next generation short range radar (SRR) for automotive applications," in *IEEE Radar Conference (RADAR)*, May 2012, pp. 0214–0219.

[9] M. Klotz and H. Rohling, "A 24 GHz short range radar network for automotive applications," in *International Conference on Radar*, 2001, pp. 115–119.

[10] N. Obeid, M. Heddebaut, F. Boukour, C. Loyez, and N. Rolland, "Millimeter wave ultra wide band short range radar localization accuracy," in *IEEE Vehicular Technology Conference(VTC)*, April 2009, pp. 1–5.

[11] W. Weidmann and D. Steinbuch, "A high resolution radar for short range automotive applications," in *European Microwave Conference*, vol. 1, Oct 1998, pp. 590–594.

[12] Y. S. Won, C. H. Kim, and S. G. Lee, "Range resolution improvement of a 24 GHz ISM band pulse radar – a feasibility study," *IEEE Sensors Journal*, vol. 15, pp. 7142–7149, Dec 2015.

[13] C. Karnfelt, A. Peden, A. Bazzi, G. El Haj Shhade, M. Abbas, and T. Chonavel, "77 ghz acc radar simulation platform," in *International Conference on Intelligent Transport Systems Telecommunications,(ITST)*, Oct 2009, pp. 209–214.

[14] Y. H. Hsiao, Y. C. Chang, C. H. Tsai, T. Y. Huang, S. Aloui, D. J. Huang, Y. H. Chen, P. H. Tsai, J. C. Kao, Y. H. Lin, B. Y. Chen, J. H. Cheng, T. W. Huang, H. C. Lu, K. Y. Lin, R. B. Wu, S. J. Chung, and H. Wang, "A 77-GHz 2t6r transceiver with injection-lock frequency sextupler using 65-nm CMOS for automotive radar system application," *IEEE Transactions on Microwave Theory and Techniques*, vol. 64, pp. 3031–3048, Oct 2016.

[15] C. Cui, S. K. Kim, R. Song, J. H. Song, S. Nam, and B. S. Kim, "A 77-GHz FMCW radar system using on-chip waveguide feeders in 65-nm CMOS," *IEEE Transactions on Microwave Theory and Techniques*, vol. 63, pp. 3736–3746, Nov 2015.

[16] M. Dudek, I. Nasr, D. Kissinger, R. Weigel, and G. Fischer, "The impact of antenna characteristics on target detection in FMCW-radar system simulations for automotive applications," in *IEEE Radio and Wireless Symposium (RWS)*, Jan 2012, pp. 107–110.

[17] M. Dudek, R. Wahl, D. Kissinger, R. Weigel, and G. Fischer, "Millimeter wave FMCW radar system simulations including a 3D ray tracing channel simulator," in *Asia-Pacific Microwave Conference Proceedings (APMC)*, Dec 2010, pp. 1665–1668.

[18] M. Dudek, D. Kissinger, R. Weigel, and G. Fischer, "A versatile system simulation environment for millimeter-wave phased-array FMCW-radar sensors for automotive applications," in *Asia-Pacific Microwave Conference Proceedings (APMC)*, Dec 2011, pp. 1478–1481.

[19] M. Dudek, D. Kissinger, and R. Weigel, "A millimeter-wave FMCW radar system simulator for automotive applications including nonlinear component models," in *European Radar Conference (EuRAD)*, Oct 2011, pp. 89–92.

[20] J. Hasch, E. Topak, R. Schnabel, T. Zwick, R. Weigel, and C. Waldschmidt, "Millimeter-wave technology for automotive radar sensors in the 77 GHz frequency band," *IEEE Transactions on Microwave Theory and Techniques*, vol. 60, pp. 845–860, March 2012.

[21] A. Bazzi, C. Kärnfelt, A. Péden, T. Chonavel, P. Galaup, and F. Bodereau, "Estimation techniques and simulation platforms for 77 GHz FMCW ACC radars," *The European Physical Journal Applied Physics*, vol. 57, 1 2012.

[22] N. T. Nguyen, R. Sauleau, M. Ettorre, and L. Le Coq, "Focal array fed dielectric lenses: An attractive solution for beam reconfiguration at millimeter waves," *IEEE Transactions on Antennas and Propagation*, vol. 59, pp. 2152–2159, June 2011.

[23] X. Wu and J. Laurin, "Fan-beam millimeter-wave antenna design based on the cylindrical Luneberg lens," *IEEE Transactions on Antennas and Propagation*, vol. 55, pp. 2147–2156, Aug 2007.

[24] N. Fonseca, M. Coudyser, J. Laurin, and J. Brault, "On the design of a compact neural network-based DOA estimation system," *IEEE Transactions on Antennas and Propagation,*, vol. 58, pp. 357–366, Feb 2010.

[25] S. Tokoro, K. Kuroda, A. Kawakubo, K. Fujita, and H. Fujinami, "Electronically scanned millimeter-wave radar for pre-crash safety and adaptive cruise control system," in *IEEE Intelligent Vehicles Symposium*, June 2003, pp. 304–309.

[26] W. Menzel and A. Moebius, "Antenna concepts for millimeter-wave automotive radar sensors," *Proceedings of the IEEE*, vol. 100, pp. 2372–2379, July 2012.

[27] J. Schoebel and P. Herrero, "Planar antenna technology for mm-wave automotive radar, sensing, and communications," in *Radar Technology*. Intech, 2010.

[28] S. V. Schell and W. A. Gardner, "High-resolution direction finding," in *Signal Processing and its Applications*, ser. Handbook of Statistics, N. Bose and C. Rao, Eds. Elsevier, 1993, vol. 10, pp. 755 – 817. [Online]. Available: http://www.sciencedirect.com/science/article/pii/S0169716105800847

[29] B. Friedlander, "Chapter 1 - wireless direction-finding fundamentals," in *Classical and Modern Direction-of-Arrival Estimation*, T. E. T. Friedlander, Ed. Boston: Academic Press, 2009, pp. 1 – 51.

[30] M. Ogawa, Y. Asana, S. Ohshima, T. Harada, N. Yamada, T. Watanabe, and K. Nishikawa, "Electrically scanned millimeter-wave radar with antenna switching," vol. 89, pp. 10–20, 2006.

[31] M. Morinaga, H. Shinoda, and H. Kondoh, "Doa estimation of coherent waves for 77GHz automotive radar with three receiving antennas," in *European Radar Conference (EuRAD)*, Sept 2009, pp. 145–148.

[32] P. Wenig, M. Schoor, O. Gunther, B. Yang, and R. Weigel, "System design of a 77 GHz automotive radar sensor with superresolution doa estimation," in *International Symposium on Signals, Systems and Electronics (ISSSE)*, July 2007, pp. 537–540.

[33] K. Geary, J. Colburn, A. Bekaryan, S. Zeng, B. Litkouhi, and M. Murad, "Automotive radar target characterization from 22 to 29 GHz and 76 to 81 GHz," in *IEEE Radar Conference (RADAR),*, April 2013, pp. 1–6.

[34] W. Buller, B. Wilson, L. van Nieuwstadt, and J. Ebling, "Statistical modelling of measured automotive radar reflections," in *IEEE International Instrumentation and Measurement Technology Conference (I2MTC)*, May 2013, pp. 349–352.

[35] N. Yamada, Y. Tanaka, and K. Nishikawa, "Radar cross section for pedestrian in 76GHz band," in *European Microwave Conference,*, vol. 2, Oct 2005, pp. 4 pp.–.

[36] D. J. Belgiovane, C. C. Chen, S. Y. P. Chien, and R. Sherony, "Surrogate bicycle design for millimeter-wave automotive radar pre-collision testing," *IEEE Transactions on Intelligent Transportation Systems*, vol. 18, pp. 2413–2422, Sept 2017.

[37] J. Choi, J. Park, and D. Yeom, "High angular resolution estimation methods for vehicle FMCW radar," in *IEEE International Conference on Radar*, vol. 2, Oct 2011, pp. 1868–1871.

[38] C. Koelen, M.-M. Meinecke, and T. Teubner, "High resolution DOA automotive radar with four receiving antennae," in *International Radar Symposium (IRS)*, May 2006, pp. 1–4.

[39] F. Belfiori, W. van Rossum, and P. Hoogeboom, "Coherent MUSIC technique for range/angle information retrieval: application to a frequency-modulated continuous wave MIMO radar," *IET Radar, Sonar Navigation*, vol. 8, pp. 75–83, February 2014.

[40] N. Liu, L.-R. Zhang, J. Zhang, and D. Shen, "Direction finding of MIMO radar through ESPRIT and Kalman filter," *Electronics Letters*, vol. 45, pp. 908–910, Aug 2009.

[41] M. Rübsamen and A. B. Gershman, "Chapter 5 - search-free DOA estimation algorithms for nonuniform sensor arrays," in *Classical and Modern Direction-of-Arrival Estimation*, T. E. T. Friedlander, Ed. Boston: Academic Press, 2009, pp. 161 – 183. [Online]. Available: http://www.sciencedirect.com/science/article/pii/B978012374524800009X

[42] K. Schuler, D. Becker, and W. Wiesbeck, "Extraction of virtual scattering centers of vehicles by ray-tracing simulations," *IEEE Transactions on Antennas and Propagation*, vol. 56, pp. 3543–3551, Nov 2008.

[43] F. Somda, O. Lafond, L. Le Coq, and M. Himdi, "RCS measuring procedure and distribution for automotives in the context of ITS," in *International Conference on Intelligent Transport Systems Telecommunications (ITST)*, Oct 2009, pp. 215–217.

[44] N. Ghassemi, K. Wu, S. Claude, X. Zhang, and J. Bornemann, "Low-cost and high-efficient w-band substrate integrated waveguide antenna array made of printed circuit board process," *IEEE Transactions on Antennas and Propagation*, vol. 60, no. 3, pp. 1648–1653, March 2012.

[45] H. Oraizi and M. T. Noghani, "Design and optimization of waveguide-fed centered inclined slot arrays," *IEEE Transactions on Antennas and Propagation*, vol. 57, no. 12, pp. 3993–3997, Dec 2009.

[46] A. F. Stevenson, "Theory of slots in rectangular wave-guides," *Journal of Applied Physics*, vol. 19, no. 1, pp. 24–38, 1948. [Online]. Available: https://doi.org/10.1063/1.1697868

[47] R. Elliott and L. Kurtz, "The design of small slot arrays," *IEEE Transactions on Antennas and Propagation*, vol. 26, no. 2, pp. 214–219, Mar 1978.

[48] D. y. Kim, W. S. Chung, C. H. Park, S. J. Lee, and S. Nam, "A series slot array antenna for 45°-inclined linear polarization with siw technology," *IEEE Transactions on Antennas and Propagation*, vol. 60, no. 4, pp. 1785–1795, April 2012.

[49] S. Mukherjee and A. Biswas, "Design of dual band and dual-polarised dual band siw cavity backed bow-tie slot antennas," *IET Microwaves, Antennas Propagation*, vol. 10, no. 9, pp. 1002–1009, 2016.

[50] R. Bayderkhani, K. Forooraghi, and B. Abbasi-Arand, "Gain-enhanced siw cavity-backed slot antenna with arbitrary levels of inclined polarization," *IEEE Antennas and Wireless Propagation Letters*, vol. 14, pp. 931–934, 2015.

[51] J. Hu, Z. C. Hao, and Z. W. Miao, "Design and implementation of a planar polarization-reconfigurable antenna," *IEEE Antennas and Wireless Propagation Letters*, vol. 16, pp. 1557–1560, 2017.

[52] H. Lee, Y. Sung, C. T. M. Wu, and T. Itoh, "Dual-band and polarization-flexible cavity antenna based on substrate integrated waveguide," *IEEE Antennas and Wireless Propagation Letters*, vol. 15, pp. 488–491, 2016.

[53] S. J. Park, D. H. Shin, and S. O. Park, "Low side-lobe substrate-integrated-waveguide antenna array using broadband unequal feeding network for millimeter-wave handset device," *IEEE Transactions on Antennas and Propagation*, vol. 64, no. 3, pp. 923–932, March 2016.

[54] Y. Li and K. M. Luk, "Low-cost high-gain and broadband substrate- integrated-waveguide-fed patch antenna array for 60-ghz band," *IEEE Transactions on Antennas and Propagation*, vol. 62, no. 11, pp. 5531–5538, Nov 2014.

[55] X. P. Chen, K. Wu, L. Han, and F. He, "Low-cost high gain planar antenna array for 60-ghz band applications," *IEEE Transactions on Antennas and Propagation*, vol. 58, no. 6, pp. 2126–2129, June 2010.

[56] D. Dousset, K. Wu, and S. Claude, "Millimetre-wave broadband transition of substrate-integrated waveguide to rectangular waveguide," *Electronics Letters*, vol. 46, no. 24, pp. 1610–1611, November 2010.

[57] I. Lim and S. Lim, "Substrate-integrated-waveguide (SIW) single-pole-double-throw (SPDT) switch for X-band applications," *IEEE Microw. Compon. Lett.*, vol. 24, pp. 536–538, Aug. 2014.

[58] Q. D. Huang, Y. J. Cheng, and J. L. W. Li, "Surface-loaded ferrite substrate integrated waveguide switch," *IEEE Microw. Compon. Lett.*, vol. 25, pp. 232–234, April 2015.

[59] A. Ghiotto, S. Adhikari, and K. Wu, "Ferrite-loaded substrate integrated waveguide switch," *IEEE Microw. Compon. Lett.*, vol. 22, pp. 120–122, March 2012.

[60] R. F. Xu, B. S. Izquierdo, and P. R. Young, "Switchable substrate integrated waveguide," *IEEE Microw. Compon. Lett.*, vol. 21, pp. 194–196, April 2011.

[61] H. Chen, W. Che, Y. Cao, W. Feng, and K. Sarabandi, "Function-reconfigurable between SPDT switch and power divider based on switchable HMSIW unit," *IEEE Microw. Compon. Lett.*, vol. 27, pp. 275–277, March 2017.

[62] M. Orefice and R. S. Elliott, "Design of waveguide-fed series slot arrays," *IEE Proceedings H-Microwaves, Optics and Antennas*, vol. 129, pp. 165–169, August 1982.

[63] L. Wu, A. J. Farrall, and P. R. Young, "Substrate integrated waveguide switched beam antenna," *IEEE Trans. Antennas Propag.*, vol. 63, pp. 2301–2305, May 2015.

[64] M. Bozzi, L. Perregrini, K. Wu, and P. Arcioni, "Current and future research trends in substrate integrated waveguide technology," *Radioengineering*, vol. 18, pp. 201–209, June 2009.

[65] D. Y. Kim, W. S. Chung, C. H. Park, S. J. Lee, and S. Nam, "A series slot array antenna for 45^o-inclined linear polarization with SIW technology," *IEEE Trans. Antenna Propag.*, vol. 60, pp. 1785–1795, April 2012.

[66] K. Geary, J. S. Colburn, A. Bekaryan, S. Zeng, B. Litkouhi, and M. Murad, "Automotive radar target characterization from 22 to 29 GHz and 76 to 81 GHz," in *IEEE Radar Conference*, April 2013, pp. 1–6.

[67] J. H. Choi, Y. Dong, J. S. Sun, and T. Itoh, "Retrodirective array immune to incident waves with arbitrary polarizations," *IEEE Transactions on Antennas and Propagation*, vol. 61, pp. 6008–6013, December 2013.

[68] S. L. Karode and V. F. Fusco, "Self-tracking duplex communication link using planar retrodirective antennas," *IEEE Transactions on Antennas and Propagation*, vol. 47, pp. 993–1000, June 1999.

[69] C. W. Pobanz and T. Itoh, "A conformal retrodirective array for radar applications using a heterodyne phased scattering element," in *Proceedings of 1995 IEEE MTT-S International Microwave Symposium*, May 1995, pp. 905–908.

[70] L. C. Van-Atta, "Electromagnetic reflector," US Patent 2,908,002, October 1959.

[71] R. Wanselow, "A proposed high gain wide angle coverage, passive, modulated reradiator," *IRE Transactions on Antennas and Propagation*, vol. 10, pp. 785–785, November 1962.

[72] V. F. Fusco, "Retrodirective array techniques for ACC vehicular augmentation," in *IEE Colloquium on Antennas for Automotives (Ref. No. 2000/002)*, 2000, pp. 6/1–6/5.

[73] J. A. Vitaz, A. M. Buerkle, and K. Sarabandi, "Tracking of metallic objects using a retro-reflective array at 26 GHz," *IEEE Transactions on Antennas and Propagation*, vol. 58, pp. 3539–3544, November 2010.

[74] A. A. M. Ali, H. B. El-Shaarawy, and H. Aubert, "Millimeter-wave substrate integrated waveguide passive Van Atta reflector array," *IEEE Transactions on Antennas and Propagation*, vol. 61, pp. 1465–1470, March 2013.

[75] P. Hallbjörner and S. Cheng, "Improvement in 77-GHz radar cross section of road work jacket and side screen by use of planar flexible retrodirective reflectors," *IEEE Antennas and Wireless Propagation Letters*, vol. 12, pp. 1085–1088, September 2013.

[76] Z. W. Miao, Z. C. Hao, and Q. Yuan, "A passive circularly polarized Van Atta reflector for vehicle radar applications," *IEEE Antennas and Wireless Propagation Letters*, vol. 16, pp. 2254–2257, June 2017.

[77] H. Zhou, W. Hong, L. Tian, X. Jiang, X. C. Zhu, M. Jiang, L. Cheng, and J. X. Zhuang, "A retrodirective antenna array with polarization rotation property," *IEEE Transactions on Antennas and Propagation*, vol. 62, pp. 4081–4088, August 2014.

[78] M. Fujita and S. Nakamura, "A polarization-rotating Van Atta array reflector and its application to polarimetric radar calibration," in *IEEE International Geoscience and Remote Sensing Symposium*, vol. 3, September 2004, pp. 1746–1749.

[79] S. Zeng and J. N. Nickolaou, "Automotive radar," in *Small and Short Range Radar Systems*. CRC Press, April 2014, pp. 261–341.

[80] J. Wenger, "Automotive radar - status and perspectives," in *IEEE Compound Semiconductor Integrated Circuit Symposium*, October 2005, pp. 21–24.

[81] T. Djerafi and K. Wu, "60 GHz substrate integrated waveguide crossover structure," in *European Microwave Conference (EuMC)*, September 2009, pp. 1014–1017.

[82] A. B. Numan, J. F. Frigon, and J. J. Laurin, "Compact W-band antenna for polarization diversity applications," in *URSI General Assembly and Scientific Symposium (URSI GASS)*, August 2017, pp. 1–4.

[83] P. S. Hall and S. J. Vetterlein, "Review of radio frequency beamforming techniques for scanned and multiple beam antennas," *IEE Proceedings H-Microwaves, Antennas and Propagation*, vol. 137, pp. 293–303, October 1990.

[84] P. Chen, W. Hong, Z. Kuai, and J. Xu, "A double layer substrate integrated waveguide blass matrix for beamforming applications," *IEEE Microwave and Wireless Components Letters*, vol. 19, pp. 374–376, June 2009.

[85] T. Djerafi and K. Wu, "Multilayered substrate integrated waveguide 4x4 butler matrix," *International Journal of RF and Microwave Computer-Aided Engineering*, vol. 22, pp. 336–344, May 2012.

[86] T. Djerafi, N. J. G. Fonseca, and K. Wu, "Planar Ku-band 4×4 nolen matrix in SIW technology," *IEEE Transactions on Microwave Theory and Techniques*, vol. 58, pp. 259–266, February 2010.

[87] E. Gandini, M. Ettorre, M. Casaletti, K. Tekkouk, L. L. Coq, and R. Sauleau, "SIW slotted waveguide array with pillbox transition for mechanical beam scanning," *IEEE Antennas and Wireless Propagation Letters*, vol. 11, pp. 1572–1575, December 2012.

[88] M. Ettorre, R. Sauleau, and L. L. Coq, "Multi-beam multi-layer leaky-wave SIW pillbox antenna for millimeter-wave applications," *IEEE Transactions on Antennas and Propagation*, vol. 59, pp. 1093–1100, April 2011.

[89] A. Hosseini, S. Kabiri, and F. D. Flaviis, "V-band high-gain printed quasi-parabolic reflector antenna with beam-steering," *IEEE Transactions on Antennas and Propagation*, vol. 65, pp. 1589–1598, April 2017.

[90] Y. J. Cheng, W. Hong, and K. Wu, "Millimeter-wave substrate integrated waveguide multibeam antenna based on the parabolic reflector principle," *IEEE Transactions on Antennas and Propagation*, vol. 56, pp. 3055–3058, September 2008.

[91] Z. L. Ma and C. H. Chan, "A novel surface-wave-based high-impedance surface multibeam antenna with full azimuth coverage," *IEEE Transactions on Antennas and Propagation*, vol. 65, pp. 1579–1588, April 2017.

[92] W. Rotman and R. Turner, "Wide-angle microwave lens for line source applications," *IEEE Transactions on Antennas and Propagation*, vol. 11, pp. 623–632, November 1963.

[93] Y. J. Cheng, W. Hong, K. Wu, Z. Q. Kuai, C. Yu, J. X. Chen, J. Y. Zhou, and H. J. Tang, "Substrate integrated waveguide (SIW) rotman lens and its Ka-band multibeam array antenna applications," *IEEE Transactions on Antennas and Propagation*, vol. 56, pp. 2504–2513, August 2008.

[94] N. Ghassemi, K. Wu, S. Claude, X. Zhang, and J. Bornemann, "Low-cost and high-efficient W-Band substrate integrated waveguide antenna array made of printed circuit board process," *IEEE Transactions on Antennas and Propagation*, vol. 60, pp. 1648–1653, March 2012.

[95] X. Wu and J. J. Laurin, "Fan-beam millimeter-wave antenna design based on the cylindrical Luneberg lens," *IEEE Transactions on Antennas and Propagation*, vol. 55, pp. 2147–2156, August 2007.

[96] G. Peeler and D. Archer, "A two-dimensional microwave Luneberg lens," *Transactions of the IRE Professional Group on Antennas and Propagation*, vol. 1, pp. 12–23, July 1953.

[97] C. Mateo-Segura, A. Dyke, H. Dyke, S. Haq, and Y. Hao, "Flat Luneburg lens via Transformation Optics for directive antenna applications," *IEEE Transactions on Antennas and Propagation*, vol. 62, pp. 1945–1953, April 2014.

[98] J. Bor, O. Lafond, H. Merlet, P. L. Bars, and M. Himdi, "Foam based Luneburg lens antenna at 60 GHz," *Progress In Electromagnetics Research Letters*, vol. 44, pp. 1–7, January 2014.

[99] M. K. Saleem, H. Vettikaladi, M. A. S. Alkanhal, and M. Himdi, "Lens antenna for wide angle beam scanning at 79 GHz for automotive short range radar applications," *IEEE Transactions on Antennas and Propagation*, vol. 65, pp. 2041–2046, April 2017.

[100] Y.-J. Park, A. Herschlein, and W. Wiesbeck, "A photonic bandgap (PBG) structure for guiding and suppressing surface waves in millimeter-wave antennas," *IEEE Transactions on Microwave Theory and Techniques*, vol. 49, pp. 1854–1859, October 2001.

[101] C. Pfeiffer and A. Grbic, "A printed, broadband Luneburg lens antenna," *IEEE Transactions on Antennas and Propagation*, vol. 58, pp. 3055–3059, September 2010.

[102] K. C. Chen, J. W. Yang, Y.-C. Yang, C. F. Khin, and M. N. M. Kehn, "Plasmonic Luneburg lens antenna synthesized by metasurfaces with hexagonal lattices," *Optics Express*, vol. 25, no. 22, pp. 27 405–27 414, October 2017.

[103] A. Dhouibi, S. N. Burokur, A. de Lustrac, and A. Priou, "Compact metamaterial-based substrate-integrated Luneburg lens antenna," *IEEE Antennas and Wireless Propagation Letters*, vol. 11, pp. 1504–1507, December 2012.

[104] M. Bosiljevac, M. Casaletti, F. Caminita, Z. Sipus, and S. Maci, "Non-uniform metasurface Luneburg lens antenna design," *IEEE Transactions on Antennas and Propagation*, vol. 60, pp. 4065–4073, September 2012.

[105] L. Xue and V. F. Fusco, "24 GHz automotive radar planar Luneburg lens," *IET Microwaves, Antennas Propagation*, vol. 1, pp. 624–628, June 2007.

[106] O. Lafond, M. Himdi, H. Merlet, and P. Lebars, "An active reconfigurable antenna at 60 GHz based on plate inhomogeneous lens and feeders," *IEEE Transactions on Antennas and Propagation*, vol. 61, pp. 1672–1678, April 2013.

[107] L. Xue and V. F. Fusco, "Printed holey plate Luneburg lens," *Microwave and Optical Technology Letters*, vol. 50, pp. 378–380, December 2007.

[108] A. B. Numan, J. F. Frigon, and J. J. Laurin, "Millimeter wave orthogonally polarized substrate integrated waveguide slot antenna arrays," in *Global Symposium on Millimeter-Waves (GSMM)*, May 2015, pp. 1–3.

[109] J. B. Rizk and G. A. Rebeiz, "W-band microstrip RF-MEMS switches and phase shifters," in *IEEE MTT-S International Microwave Symposium Digest, 2003*, vol. 3, June 2003, pp. 1485–1488 vol.3.

[110] W. Hongtao, G. Xuebang, W. Hongjiang, W. Bihua, and L. Yanan, "W-band GaAs PIN diode SPST switch MMIC," in *2012 International Conference on Computational Problem-Solving (ICCP)*, October 2012, pp. 93–95.

MATLAB CODE FOR ESPRIT ALGORITHM

A MATLAB code is listed below to simulate ESPRIT algorithm. This code implements a signals reflected by targets which are placed at different angular positions. This signal is received by a uniform linear array. The targets are modeled by Weibull distribution, characterized by shape and scale parameters as described in [34]. The number of elements in the array is N where each element has radiation pattern stored in radpat_HPBW_30.csv file. The number of targets and their angular position with respect to the normal of the array axis are defined in *DoAs*. Column vectors of matrix A represent array factor for each target in *DoAs*. K samples of the signal reflected back from the analytically modeled targets along with gaussian noise are stored in matrix s. The signal received by the array is then mathematically calculated using Equation 3.2 followed by correlation matrix given in Equation 3.3. Once we have correlation matrix, noise and signal spaces are separated using eigndecomposition. Finally, linear system of Equation 3.4 in signal space is solved to get DoA information. This estimated information is compared with the actual DoA information in *DoAs* to get the error. This algorithm is run by one thousand times and average error at each iteration is used to develop error distribution curves shown in Figures 3.2-3.4.

The below code simulates three targets placed at angle 15^o, 10^o and 5^o with respect to the normal of the array axis. The array is five element uniform linear array with inter-element spacing of half wavelength. Five samples are collected at the receiver array. The targets are midsized vehicle modeled as weibull distribution with shape and scale parameters of 0.8 and 20, respectively [34]. The SNR is set to -3 dB.

```
clear
clc
N=5;% Number of receiver antenna elements
K=5; % Number of snapshots recorded at the receiver
rad_pat=csvread('radpat_HPBW_30.csv');% Radiation pattern of individual antenna element in the receiver array
DoAs=[15,10,5];% Target angular position and number of targets
theta=DoAs.*(pi/180);% Target position from degrees to radians
%Statistical modelling of measured automotive radar reflections
Shape=0.8.*ones(1,length(DoAs));% Weibull distribution parameters for target modeling [34]
```

```
Scale=20.*ones(1,length(DoAs));% Weibull distribution parameters for target modeling [34]
for cnt=1:1000 % Iterations for the algorithm to determine error distribution
SNR=0.5*wblrnd(Scale,Shape); % Target reflected signal
SNR_test(cnt,:)=SNR;
%Implementing Equation 3.1
M=length(theta);
r=length(DoAs);
d=0.5;
k=1:N;
for w=1:M
A(:,w)=exp(1i*2*pi*0.5*(k-1)*sin(theta(w)))';
end
%End implementing Equation 3.1
%Signal received by the linear array Equation 3.2
for w=1:M
s(w,:)=rad_pat(rad_pat(:,1)==DoAs(w),2).*(SNR(w)*randn(1,K)+ j*SNR(w)*randn(1,K));
end
X=A*s+sqrt(0.5)*randn(N,K)+j*sqrt(0.5)*randn(N,K);


%End implementing Equation 3.2
R=X*X';% Correlation matrix Equation 3.3


%ESPRIT Algorithm
[Q, D]=eig(R); %Compute eigendecomposition of covariance matrix
[D, I]=sort(diag(D),1,'descend'); %Find r largest eigenvalues
Q=Q(:,I); %Sort the eigenvectors to put signal eigenvectors first
Qs=Q (:,1:r); %Get the signal eigenvectors
Qn=Q(:,r+1:N); %Get the noise eigenvectors


phi= linsolve(Qs(1:N-1,:),Qs(2:N,:));% linear system solution Equation 3.4
ESPRIT_doas=asin(-angle(eig(phi))/(2*pi*d))*180/pi; % Equation 3.5
error(:,cnt)=abs(sort(ESPRIT_doas,'descend')'-DoAs);
end
Merror=mean(error);
%Error distribution calculation
```

```
for cnt=1:20
error_ind(cnt)= length(Merror((Merror<cnt) & (Merror>(cnt-1))));
Merror((Merror<cnt) & (Merror>(cnt-1)))=0;
end

%Plotting error distribution
plot(1:20,smooth(error_ind),'LineWidth',3)
xlabel('DoA Error(deg.)')
ylabel('Error Count')
set(gca,'FontSize',30)
grid on
avg_SNR1=10*log10(mean(SNR_test))
hold on
```